MBE Growth and Characterization of $EuFe_2(As_{1-x}P_x)_2$ Thin Films: Magnetism, Superconductivity, and Experimental Devices

Pedram Bassirian

Oriel College
University of Oxford

A thesis submitted for the degree of
Doctor of Philosophy

Michaelmas 2025

Abstract

This dissertation details the synthesis, characterization, and device fabrication of the ferromagnetic superconductor $EuFe_2(As_{1-x}P_x)_2$ in high-quality thin film form. A robust molecular beam epitaxy (MBE) growth process was established, enabling the first successful growth of smooth, epitaxial films of this complex material.

The structural and chemical properties of the films were investigated using X-ray diffraction (XRD), Rutherford backscattering spectrometry (RBS) and scanning transmission electron microscopy (STEM) with energy-dispersive X-ray spectroscopy (EDX) mapping. These efforts enabled the assembly of a superconducting phase diagram as a function of phosphorus content and film thickness. A key finding was the significant variability in the films' properties, which did not correlate with the physical parameters in a straightforward way. To investigate potential origins for this behavior, magnetic properties were measured with SQUID magnetometry. The critical current density was then extracted from these data using the Bean critical state model and analyzed using vortex pinning models. Finally, X-ray magnetic circular dichroism (XMCD) was used to provide element-specific magnetic information.

The viability of these films for applications was demonstrated through the fabrication of Hall bar and ring-shaped structures. The Hall bars enabled detailed magnetotransport studies; the longitudinal and transverse resistivity in the normal state were analyzed within a three-carrier model. Furthermore, the unconventional temperature dependence of the upper critical field (H_{c2}), specifically its upturn near T_c, was investigated using a two-band model of superconductivity. The Little-Parks effect was studied using ring geometries, where the observed oscillations showed slight deviations from the conventional form, possibly indicating two contributing frequencies.

This work introduces a methodology for the growth of $EuFe_2(As_{1-x}P_x)_2$ thin films and advances understanding of their fundamental properties, opening new directions for research on this class of ferromagnetic superconductors.

MBE Growth and Characterization of $EuFe_2(As_{1-x}P_x)_2$ Thin Films: Magnetism, Superconductivity, and Experimental Devices



Pedram Bassirian

Oriel College

University of Oxford

A thesis submitted for the degree of

Doctor of Philosophy

Michaelmas 2025

To my parents, for their enduring love and the foundation they laid for my growth,
and to my partner, for their patient support and encouragement throughout this journey.

Acknowledgements

First and foremost, I would like to thank my supervisor, Prof. Thorsten Hesjedal, for his outstanding guidance, patience, and availability. I have never had a supervisor who responded to emails so quickly. His support has been constant, reliable, and essential for the completion of this thesis.

I am also grateful to Prof. Stuart Parkin, in whose institute this research was carried out. His support in providing access to world-class facilities and a stimulating scientific environment was indispensable for the work presented here.

I am very thankful to Prof. Andrew Boothroyd, my college mentor, who always had an open ear and provided advice and encouragement, not only in scientific matters but also when I needed personal support.

Special thanks go to Amilcar Bedoya-Pinto, who first introduced me to molecular beam epitaxy and patiently taught me how to use it. An experience that set the foundation for much of the work presented here.

This journey would not have been the same without the colleagues who made long hours in the lab and office more enjoyable. In particular, I want to acknowledge Mindaugas Silinskas, Jiho Yoon, Hakan Deniz, Ilya Kostanovski, Lukas Fischer, Berthold Rimmler, Mihir Date, Anvesh Dixit, Anirban Chakraborty, Simon Arnold, Pranava Sivakumar, Rana Saha, Jagannath Jena, Souvik Das, Tobias Fäth, Prajwal Rigvedi Madhusudan Rao and Mostafa Marzouk. Listing so many names perhaps says as much about the size of the group as it does about the fun we had, sometimes large groups make science complicated, but we were never short of company.

I also extend my thanks to Kai Litzius. Although our collaborative projects lie outside the scope of this thesis, I am grateful for our scientific discussions and his continued support.

Special appreciation goes to Michael Strauch, Ann-Kristin Flieger, and Martha Schulz for their behind-the-scenes support that kept the institute running and

helped me navigate administrative matters. Likewise, I thank Prof. Bernhard Keimer and Zrinka Gattin for their work with the Max Planck Graduate Center for Quantum Materials, which provided me with a broader academic framework during my PhD.

In addition, I want to highlight the many colleagues whose scientific contributions directly shaped the work in this thesis. Growth of films was carried out in close collaboration with Mindaugas Silinskas. Focused ion beam sample preparation for TEM was performed with the help of Norbert Schrammelt and Hakan Deniz, while TEM and STEM measurements were conducted by Hakan Deniz. RBS measurements and analysis were performed by Ilya Kostanovski and Herbert Engelhard. Room-temperature STM measurements were contributed by Anshuman Padhi and Jingrong Ji. XMCD experiments were carried out by Thorsten Hesjedal, Ethan Arnold, and Emily Heppell, with analysis from Gerrit van der Laan. E-beam lithography and resistivity measurements were performed by Jiho Yoon. Support with MBE maintenance, particularly during system opening, was provided by Andreas Frommfeld. Low-temperature STM/STS measurements have been conducted by Felix Küster and Jenny Davern. These contributions were essential, and I am grateful for the collaborative spirit that made them possible.

Finally, I am deeply indebted to my parents and to my partner whose love and confidence have been a constant source of strength.

Abstract

This dissertation details the synthesis, characterization, and device fabrication of the ferromagnetic superconductor $EuFe_2(As_{1-x}P_x)_2$ in high-quality thin film form. A robust molecular beam epitaxy (MBE) growth process was established, enabling the first successful growth of smooth, epitaxial films of this complex material.

The structural and chemical properties of the films were investigated using X-ray diffraction (XRD), Rutherford backscattering spectrometry (RBS) and scanning transmission electron microscopy (STEM) with energy-dispersive X-ray spectroscopy (EDX) mapping. These efforts enabled the assembly of a superconducting phase diagram as a function of phosphorus content and film thickness. A key finding was the significant variability in the films' properties, which did not correlate with the physical parameters in a straightforward way. To investigate potential origins for this behavior, magnetic properties were measured with SQUID magnetometry. The critical current density was then extracted from these data using the Bean critical state model and analyzed using vortex pinning models. Finally, X-ray magnetic circular dichroism (XMCD) was used to provide element-specific magnetic information.

The viability of these films for applications was demonstrated through the fabrication of Hall bar and ring-shaped structures. The Hall bars enabled detailed magnetotransport studies; the longitudinal and transverse resistivity in the normal state were analyzed within a three-carrier model. Furthermore, the unconventional temperature dependence of the upper critical field (H_{c2}), specifically its upturn near T_c, was investigated using a two-band model of superconductivity. The Little-Parks effect was studied using ring geometries, where the observed oscillations showed slight deviations from the conventional form, possibly indicating two contributing frequencies.

This work introduces a methodology for the growth of $EuFe_2(As_{1-x}P_x)_2$ thin films and advances understanding of their fundamental properties, opening new directions for research on this class of ferromagnetic superconductors.

Contents

List of Figures **xi**

List of Abbreviations **xiii**

1 Introduction **1**
1.1 Introduction to Iron-Based Superconductors 2
1.1.1 Historical Context and Comparison with Cuprates 2
1.1.2 Overview of FeSC Families and Basic Properties 3
1.1.3 Electronic Structure and Gap Symmetry in Iron-Based Superconductors 8
1.2 $EuFe_2As_2$: A Special Case in the 122 Family 10
1.2.1 Dual Magnetism: Itinerant Fe Spin-Density-Wave and Localized Eu Moments 10
1.2.2 Superconductivity under Pressure and Doping 11
1.3 Motivation and Outline 15

2 Methodology **19**
2.1 Molecular Beam Epitaxy: Principles and Practice 20
2.2 Structural and Compositional Characterization 29
2.2.1 Principles of X-ray Diffraction 29
2.2.2 Rutherford Backscattering Spectrometry 30
2.2.3 Energy Dispersive X-ray Spectroscopy and Elemental Analysis 32
2.2.4 Transmission and Scanning Transmission Electron Microscopy 35
2.3 Magnetic Characterization 38
2.3.1 Fundamentals of SQUID Magnetometry 38
2.3.2 X-ray Magnetic Circular Dichroism 41
2.4 Device Fabrication by Electron Beam Lithography 43

3 Theoretical Toolkit **45**
3.1 Gurevich Two-Band Model 46
3.2 Multi-carrier Transport 50
3.3 Bean Critical State Model 51
3.4 Collective Vortex Pinning Model 52
3.5 Little-Parks Effect 53

4 Molecular Beam Epitaxy of $EuFe_2(As_{1-x}P_x)_2$ 57
4.1 $EuFe_2As_2$: Laying the Groundwork for Substitution 58
4.2 Extending Growth to the P-Substituted System 63

5 Transport Measurements 71
5.1 Systematics of the Superconducting Phase Diagram 72
5.2 Field-Dependent Properties of a Representative Device 75
5.3 Normal State Transport and Multi-Carrier Analysis 82
5.4 Magnetoresistance Oscillations in Square Rings 87

6 Magnetometry Measurements 93
6.1 General Magnetic Properties 94
6.2 Bean Critical-State Analysis and Pinning Models 98
6.3 Probing Element-Specific Magnetism with XMCD 100

7 Summary and Outlook 105

A Additional Material for Chapter 4 109

B Additional Material for Chapter 5 113

C Additional Material for Chapter 6 115

References 117

List of Figures

1.1 Overview of key electronic features of FeSCs. 9
1.2 Resistivity evolution and phase diagrams of bulk EFAP. 13

2.1 Fundamental MBE growth modes and surface reaction kinetics. . . 23
2.2 Transition from step-flow growth to nucleation growth as a function of rate and terrace width in GaAs. 24
2.3 Illustration of MBE chamber. 25
2.4 RHEED geometry and characteristic diffraction patterns for different crystalline morphologies. 27
2.5 GaAs(100) $\beta(2 \times 4)$ surface reconstruction. 28
2.6 RBS spectrum of Ta capped EFAP with SIMNRA fit. 32
2.7 EDX process illustration and spectrum of a 80 nm EFAP sample. . 33
2.8 Schematic illustration of TEM image and diffraction formation. . . 36
2.9 Schematic of STEM imaging, detectors, and HAADF result. 37
2.10 Schematic and operational illustrations of the SQUID magnetometer. 39
2.11 Illustration of an EBL patterning process. 43

3.1 Comparison of $H_{c2}(T)$ curves from WHH and Gurevich models. . . 49
3.2 Illustration of the Little-Parks effect. 54

4.1 RHEED, XRD, and STEM characterization of EFA thin films. . . . 61
4.2 In-situ room-temperature STM during growth of initial EFA layers. 63
4.3 Growth rate versus substrate temperature grouped by RHEED-based morphology classification. 64
4.4 XRD θ–2θ scans of EFAP films for different P-content. 66
4.5 STEM and atomic-resolution EDX Maps of EFAP film with high P-content. 69

5.1 Temperature-dependent normalized resistivity curves for EFAP of different P-content and thickness-dependent phase diagram. 73
5.2 Temperature-dependent resistivity of a Hall-bar device in different field orientations. 76

5.3 Temperature dependence of the upper critical field $H_{c2}(T)$ for IP and OOP fields, with extrapolated zero-temperature values and coherence lengths from different fitting models. 78
5.4 $H_{c2}(T)$ curves for different resistivity criteria and field orientations, fitted using the Gurevich two-band model. 80
5.5 Longitudinal and transverse resistivity as a function of magnetic field, with fits to three-carrier model. 84
5.6 Resistance–temperature and field-dependent LP oscillation measurements of ring devices. 88
5.7 Background-corrected LP oscillations in EFAP at different temperatures. 90

6.1 SQUID magnetometry results of representative EFAP films. 95
6.2 Analysis of J_c and Vortex Pinning within the Bean Critical State Framework. 99
6.3 XMCD measurements of EFAP 103

A.1 STEM-EDX map of superconducting EFAP film and STEM of (100) and (110) cut comparison. 111

B.1 Low-temperature STS and STEM results on ultrathin EFAP film. . 114

C.1 XAS and XMCD on EFAP film with thicker capping. 116

List of Abbreviations

AF, AFM . . . Antiferromagnetic, Antiferromagnetic material

BEP . . . . . Beam equivalent pressure

EBL . . . . . Electron beam lithography

EDX . . . . . Energy dispersive X-ray spectroscopy

EFA . . . . . $EuFe_2As_2$

EFAP . . . . . $EuFe_2(As_{1-x}P_x)_2$

FeSC, FeSCs . Iron-based superconductor/s

FM . . . . . Ferromagnetic

GL . . . . . Ginzburg–Landau

HAADF . . . . High-angle annular dark-field

H_{c2} . . . . . Upper critical magnetic field

IP, OOP . . . In-plane, Out-of-plane

J_c . . . . . Critical current density

LP . . . . . Little-Parks

MBE . . . . . Molecular beam epitaxy

MR . . . . . Magnetoresistance

QCM . . . . . Quartz Crystal Microbalance

RBS . . . . . Rutherford backscattering spectroscopy

RGA . . . . . Residual Gas Analyzer

RHEED . . . . Reflection High-Energy Electron Diffraction

RKKY . . . . Ruderman–Kittel–Kasuya–Yosida

SDW . . . . . Spin-density wave

STEM . . . . . Scanning transmission electron microscopy

STM . . . . . Scanning tunneling microscopy

STS . . . . . Scanning tunneling spectroscopy

STO . . . . . $SrTiO_3$

SQUID . . . . Superconducting quantum interference device

TEM . . . . . Transmission electron microscopy

T_C . . . . . Curie temperature

T_c . . . . . Superconducting critical temperature

T_N . . . . . Néel temperature

UHV . . . . . Ultra-high vacuum

XAS . . . . . X-ray absorption spectroscopy

XMCD . . . . X-ray magnetic circular dichroism

XRD . . . . . X-ray diffraction

WHH . . . . . Werthamer–Helfand–Hohenberg

1

Introduction

This chapter sets the stage for the present thesis by providing an overview of iron-based superconductors (FeSCs). We begin with a historical perspective, briefly comparing FeSCs to the well-known cuprate superconductors. Next, the main FeSC families are introduced, highlighting their structural and stoichiometric differences while emphasizing the canonical set of physical properties they share. Understanding these properties and their interplay naturally leads to a discussion of the underlying electronic structure, which is explored in the following section. The chapter then focuses on the special case of Eu-based materials, which serve as the foundation for the doped compounds studied in this work, with particular attention to how Eu moments influence superconductivity. The chapter concludes with a summarizing motivation for this thesis and a brief roadmap of its structure.

Contents

1.1 Introduction to Iron-Based Superconductors 2
1.1.1 Historical Context and Comparison with Cuprates . . . 2
1.1.2 Overview of FeSC Families and Basic Properties 3
1.1.3 Electronic Structure and Gap Symmetry in Iron-Based Superconductors 8
1.2 $EuFe_2As_2$: A Special Case in the 122 Family 10
1.2.1 Dual Magnetism: Itinerant Fe Spin-Density-Wave and Localized Eu Moments 10
1.2.2 Superconductivity under Pressure and Doping 11
1.3 Motivation and Outline 15

1.1 Introduction to Iron-Based Superconductors

1.1.1 Historical Context and Comparison with Cuprates

The discovery of high-temperature superconductivity in layered cuprate perovskites in 1986 by Bednorz and Müller [1, 2] ignited a worldwide surge in superconductivity research [3, 4], further amplified by the awarding of the Nobel Prize in Physics to both scientists just a year after their groundbreaking discovery. The cuprates, which achieved critical temperatures (T_c) above 130 K at ambient pressure, remained the only class of materials with T_c well above the boiling point of liquid nitrogen for over two decades [3]. It was therefore a major breakthrough when in 2008 a new family of high-T_c superconductors was discovered: the iron-based superconductors (FeSCs) [4–6]. Their discovery was also unexpected because they contain iron, long considered antagonistic to superconductivity due to its strong magnetic character, thereby further challenging prevailing views on the interplay of magnetism and superconductivity [4]. The first FeSC was the iron-oxypnictide $LaFeAsO_{1-x}F_x$, in which superconductivity at $T_c \approx 26$ K was reported by Kamihara *et al.* [7]. This discovery was shortly followed by the identification of other superconducting iron pnictides with higher T_c, including $SmFeAsO_{1-x}F_x$ with $T_c \sim 43 - 55$ K[8, 9], and the structurally simpler $Ba_{1-x}K_xFe_2As_2$ (the "122" family) with T_c up to 38 K [10]. The rapid rise in T_c and the quick proliferation of new compounds indicated that FeSCs constitute a broad materials family, analogous in some ways to the cuprates but with important differences.

Like cuprates, the FeSCs are quasi-two-dimensional, layered materials in which superconductivity emerges when an antiferromagnetic (AFM) ground state in the undoped parent compound is suppressed. The two families, however, differ fundamentally in their electronic and magnetic properties. The cuprate parents are strongly correlated charge-transfer (Mott) insulators [11] with localized Cu 3d moments that order in a Néel-type AFM pattern [3]. In contrast, FeSC parent compounds are mostly semimetals with multiple Fe 3d–derived bands crossing the Fermi level; conduction arises from Fe 3d orbitals hybridized with pnictogen or

chalcogen p orbitals, forming electron and hole Fermi pockets that support a spin-density-wave (SDW) instability driven by Fermi-surface nesting [6]. Cuprates possess a single CuO_2-derived band that, when doped, yields one Fermi surface and typically exhibits *d*-wave pairing symmetry, whereas FeSCs are multiband superconductors often displaying an *s*-wave–like gap symmetry [3, 6]. Thus, while electron correlations and magnetism are central to both systems, they manifest in distinct ways.

The discovery of FeSCs opened new directions because their superconductivity can occur at relatively high temperatures in materials that are not copper-based, suggesting new pairing mechanisms. By 2008 – 2010, dozens of FeSCs were identified across several structural families (described below) with T_c reaching up to 55 K in bulk samples [9]. Moreover, thin-film and interfacial engineering led to even higher effective T_c in some cases, for example monolayer FeSe on $SrTiO_3$ (STO) showed signature of superconductivity above 60 K [12, 13]. While still below the cuprate record, these values firmly place FeSCs as the second high-T_c superconductor family. Importantly, FeSCs offer advantages such as high critical current densities in polycrystalline form (due to weaker superconducting anisotropy and less sensitivity to grain boundaries than cuprates) [14, 15], and a rich interplay of superconductivity with magnetism [16]. These aspects have motivated intensive research into the fundamental physics of FeSCs and their potential applications.

1.1.2 Overview of FeSC Families and Basic Properties

The FeSCs encompass several distinct crystallographic families, commonly labeled by the stoichiometry of their formulas as 11, 111, 1111, and 122 (among others). Despite differences in composition, they all share a common structural motif: layers of Fe atoms in a square planar arrangement, each Fe coordinated tetrahedrally by pnictogen (P, As) or chalcogen (Se, Te) atoms. Superconductivity is confined to these Fe-X (pnictogen/chalcogen) layers, analogous to the CuO_2 planes in cuprates, while intervening layers of other elements act as charge reservoirs or structural support. The crystal structures of the families noted above are presented in Table 1.1. For clarity, a schematic representation of unit cells is utilized that always

contains two Fe-X layers, thereby emphasizing the structural similarities between families. This representations are not crystallographically rigorous primitive unit cells, but serve as a convenient framework for comparison. For the 122 family, both, the primitive 2 Fe and the reduced 1 Fe unit cells are also shown. The following paragraphs provide an overview of some selected members of each family and their general properties. This overview is necessarily selective, as a comprehensive list is unfeasible given the rapid expansion of the field, which had generated over 3000 publications within the first five years of discovery [17].

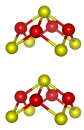
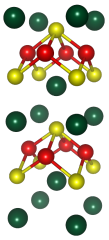
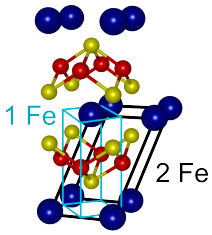
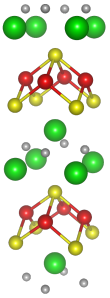
			
11	111	122	1111

Table 1.1: Crystal structures of representative FeSCs, categorized by structural family: 11, 111, 122, and 1111. Fe atoms are shown in red, pnictogen/chalcogen atoms in yellow, alkali metals (Li, Na) in 111 in dark green, 122 cations (Ba, Sr, Ca, Eu) in dark blue, rare-earth elements in 1111 (La, Sm, Nd, Pr) in bright green, and O in white. For the 122 structure, two commonly used unit cells, distinguished by containing either one or two Fe atoms, are illustrated.

The **1111 family**, with the general formula RFeAsO (R = rare-earth element e.g. La, Sm, Nd or Pr), holds a historic place as it includes $LaFeAsO_{1-x}F_x$, the compound that marked the discovery of FeSCs [7]. Structurally, these materials adopt a tetragonal ZrCuSiAs structure (space group $P4/nmm$) with alternating fluorite-type Fe_2As_2 and anti-fluorite type R_2O_2 layers. The undoped parent compounds are semimetals that exhibit an SDW transition of the Fe moments below a temperature of around $T_{\mathrm{SDW}} \approx 130 - 160$ K, which is coupled to a tetragonal-to-orthorhombic structural transition [18–20]. These transitions are closely associated with the onset of electronic nematicity, i.e. the breaking of the electronic fourfold rotational symmetry while preserving translational symmetry. Whether nematicity

is primarily driven by orbital degrees of freedom, spin fluctuations, or lattice effects remains debated, representing an "chicken-and-egg" problem frequently discussed in the field [21, 22].

Superconductivity is induced by doping, typically by substituting O^{2-} with F^{-}, which suppresses the SDW order [19, 23]. This leads to the highest critical temperatures among bulk FeSCs, reaching up to 55 K for $SmFeAsO_{1-x}F_x$ [9]. Application of pressure can also induce superconductivity, though typically less effectively [24]. Many superconducting members of this family can be grown as thin films. Initial pulsed laser deposition (PLD) growths were reported as early as 2008 [25], but the volatility of F required substitution to be performed ex-situ, limiting epitaxial quality. Fully in-situ growth was later achieved using molecular beam epitaxy (MBE), for example, NdFeAs(O,F) on CaF_2 [26], or SmFeAs(O,F) on multiple oxide substrates and CaF_2, where an overlayer of SmF_3 serves as the F donor [27] and using PLD, e.g., SmFeAs(O,F) on CaF_2, which itself acts as an F supplier [28]. As the first FeSCs, the 1111 compounds were frequently used for comparison in early studies, providing a reference for assessing newly discovered families.

Indeed, moving to the structurally simplest system, the **11 family**, one encounters marked differences. Bulk undoped FeSe, unlike the 1111 compounds, is superconducting at ambient pressure without any magnetic ordering. Apart from FeSe, this family includes compounds such as $FeSe_{1-x}Te_x$. These materials consist solely of stacked Fe-X layers (where X is a chalcogen) without any intermediary spacer layers, resulting in a tetragonal PbO-type structure built from edge-sharing $FeSe_4$ tetrahedra. At ambient pressure, bulk FeSe has a modest T_c of approximately 8 K [29], which can be significantly enhanced to around 37 K under applied pressure [30]. Substituting Se with Te also raises the critical temperature, with $FeSe_{1-x}Te_x$ reaching a T_c of 14 K [31]. This value can be further increased either by applying pressure or through fabrication as a thin film [32]. The most dramatic enhancement of superconductivity in this family has been observed in ultrathin films. FeSe, when grown as a single monolayer on an STO substrate, can exhibit an

astonishingly high T_c of 65 K or more [12, 13]. This remarkable discovery, likely driven by interface effects, highlighted the profound impact of lattice and interface engineering and was considered significant enough to motivate the filing of a patent [33]. Although bulk FeSe at ambient pressure lacks static magnetic order, magnetic interactions play a central role in its physics, reinforcing its close connection to the broader FeSC family. Inelastic neutron scattering has revealed both stripe and Néel spin fluctuations [34], placing FeSe close to a magnetic instability. Also, thin films on STO have shown indications of SDW order [35], and bulk FeSe develops magnetic order under applied pressure, seemingly unlike other families where magnetism and superconductivity are typically antagonistic. In reality, the initial parallel increase of both phases with pressure reflects the relief of magnetic frustration; at higher pressures, however, the usual competition re-emerges, and the suppression of magnetic order coincides with a sharp enhancement of T_c [36].

The **111 family**, with general formula AFeAs (A = Li, Na), adopts a tetragonal PbFCl- type ($P4/nmm$) structure consisting of alternating alkali-metal and FeAs layers. LiFeAs is particularly notable as it exhibits superconductivity in stoichiometric form with a critical temperature of about 18 K, without the need for doping or pressure [37]. Unlike most other FeSCs, LiFeAs does not show long-range magnetic order in its parent state, likely due to poor Fermi-surface nesting [38], although AFM fluctuations have been detected by nuclear magnetic resonance [39]. This makes it similar to the outlier discussed above, FeSe. NaFeAs, in contrast, is not a bulk superconductor in its undoped state: while filamentary superconductivity can be assessed by neutron scattering [40], the superconducting volume fraction is small in transport measurements [41], and robust superconductivity emerges only upon electron or hole doping, or under applied pressure [42, 43]. Together with FeSe from the 11 family, LiFeAs and NaFeAs form a distinct subset of FeSCs, where superconductivity can appear without a proceeding supression of magnetic ordering, setting them apart from the majority of FeSC compounds in which magnetism, nematicity and structural transitions are present in the undoped parent compounds at ambient pressure.

The **122 family**, with general formula $A\mathrm{Fe_2As_2}$ (A = Ba, Sr, Ca, Eu), crystallizes in the $\mathrm{ThCr_2Si_2}$-type structure (space group $I4/mmm$), consisting of FeAs layers separated by alkaline-earth or rare-earth layers. $\mathrm{BaFe_2As_2}$ and its relatives are among the most studied FeSCs because large, high-quality single crystals can be grown. The parent 122 compounds are semimetallic and undergo a coupled structural (tetragonal-to-orthorhombic) and SDW transition, e.g., at $T_{\mathrm{SDW}} \approx 143$ K for $\mathrm{BaFe_2As_2}$ [44] and $T_{\mathrm{SDW}} \approx 190$ K for $\mathrm{EuFe_2As_2}$ [45]. As $\mathrm{EuFe_2As_2}$ also contains magnetic moments on the Eu sublattice, it exhibits multiple magnetic phase transitions, which will only be briefly mentioned here and discussed in more detail in section 1.2. This family also contains some unusual members that are superconducting under ambient pressure without doping, such as $\mathrm{KFe_2As_2}$ [46], $\mathrm{RbFe_2As_2}$ [47], and $\mathrm{CsFe_2As_2}$ [48]. Whether these should be considered true parent compounds or effectively heavily doped end members is a matter of terminology. More generally, superconductivity can be induced through hole doping (e.g., $\mathrm{Ba_{1-x}K_xFe_2As_2}$, T_{c} up to 38 K [10]), electron doping (e.g., $\mathrm{Ba(Fe_{1-x}Co_x)_2As_2}$, $T_{\mathrm{c}} \sim 23$ K [49]), isovalent substitution ($\mathrm{BaFe_2(As_{1-x}P_x)_2}$, $T_{\mathrm{c}} \sim 30$ K [50]), or application of pressure [51]. Compared to the 1111 family, 122 compounds generally have slightly lower T_{c} values but are easier to grow and handle, making them workhorses for experimental studies. Notably 122 thin films, particularly Co- or P- and K-doped $\mathrm{BaFe_2As_2}$ exhibit very high critical current densities J_c (several MA/cm^2) and reduced sensitivity to grain boundaries [14, 15, 52–54], which is promising for technological applications such as superconducting wires.

From this brief overview, a unifying theme becomes apparent: most parent compounds of FeSCs exhibit SDW order and a tetragonal-to-orthorhombic structural transition, both of which are gradually suppressed upon doping or pressure, giving way to superconductivity. In some cases, it is argued that magnetism and superconductivity even coexist microscopically over a finite range of parameters [55–58]. Although certain materials such as FeSe or LiFeAs stand out as described, the overall phenomenology across families is remarkably consistent. Underlying their

common properties is a comparable multi-band electronic structure, which will be discussed next.

1.1.3 Electronic Structure and Gap Symmetry in Iron-Based Superconductors

FeSCs are characterized by a multi-band electronic structure that governs both their magnetic and superconducting properties. Early density functional theory (DFT) calculations [59] and angle-resolved photoemission spectroscopy (ARPES) studies [60] revealed that several Fe d-orbitals contribute to states near the Fermi level in FeSCs, producing hole-like Fermi surface pockets at the Brillouin zone center (Γ) and electron-like pockets at the zone corners (M). This is illustrated schematically for the case of a 122-type compound in the 2 Fe Brillouin zone in Figure 1.1(c). A crucial feature, first emphasized by theoretical means by Mazin *et al.* [61], is the nesting between hole and electron pockets by a wavevector $\mathbf{Q} \approx (\pi, 0)$, illustrated in Figure 1.1(d). This nesting drives an instability towards SDW order.

As outlined in the previous sections, superconductivity typically emerges when this SDW order is suppressed by doping or pressure, while spin fluctuations persist. The resulting competition and interplay between magnetism and superconductivity is captured in the generic FeSC phase diagram Figure 1.1(a). AFM spin fluctuations are widely believed to play a central role in the pairing mechanism of FeSCs, with superconductivity mediated not by phonons but by these magnetic interactions [6, 62].

In theoretical language, this can be described within a multi-orbital Hubbard framework, where the role of spin fluctuations can be analyzed using the Random Phase Approximation (RPA) [65–67]. With this, a strongly enhanced spin susceptibility can be found, $\chi_s(\mathbf{q}) = \chi_0(\mathbf{q})/(1 - U\chi_0(\mathbf{q}))$, at a characteristic wavevector of the spin fluctuation $\mathbf{Q}$. This leads to an effective pairing interaction term, $V(\mathbf{k}, \mathbf{k}')$, mediated by these spin fluctuations. The interaction is repulsive in the spin-singlet channel ($V^{\text{singlet}} \sim +U^2\chi_s$) but can be attractive in the spin-triplet channel ($V^{\text{triplet}} \sim -\frac{1}{2}U^2\chi_s$). For the AFM fluctuations dominating FeSCs, the singlet interaction can still induce pairing despite being repulsive, provided the

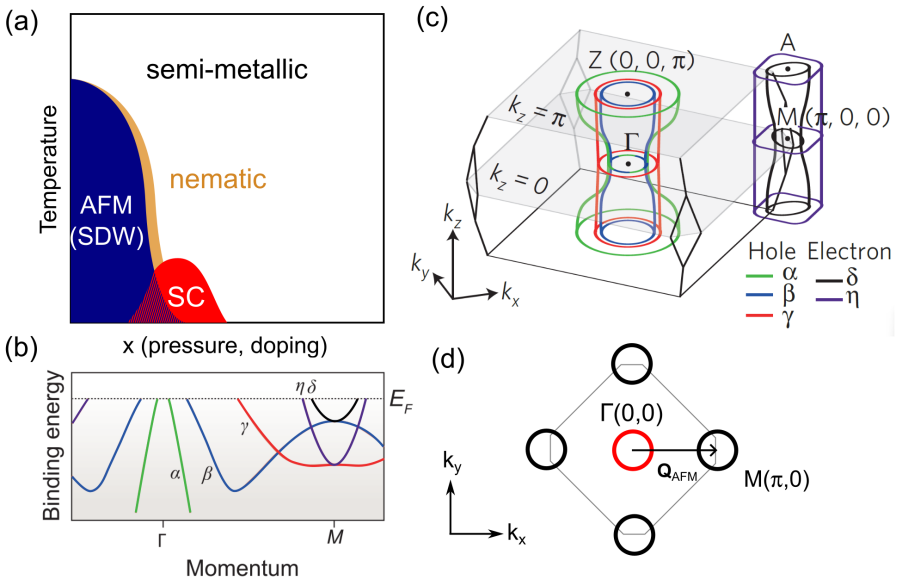


Figure 1.1: Overview of the key electronic features of FeSCs. (a) Generic phase diagram showing the suppression of AFM order and emergence of superconductivity with doping or pressure. (b) Schematic band dispersion near the Fermi level, highlighting the multi-band character arising from Fe 3d orbitals. Reproduced from [63], redrawn with added color. (c) Schematic Fermi surface sheets in the 2 Fe Brillouin zone notation, consisting of hole-like pockets centered at Γ and electron-like pockets centered at $M = (\pi, 0)$ and equivalent points. Figure from [64]. (d) Top view ($k_z = 0$ cut) of the Fermi surface illustrating how the hole and electron pockets are approximately nested by the AFM wavevector $\mathbf{Q}_{\mathrm{AFM}} = (\pi, 0)$. This quasi-nesting drives the stripe-type AFM order of the parent compounds and provides the momentum structure for spin-fluctuation mediated $s^{\pm}$ pairing.

superconducting gap, $\Delta(\mathbf{k})$, changes sign between different parts of the Fermi surface. This can be better understood when considering the linearized gap equation, from which the gap is retrieved self-consistently [68]:

$$\Delta(\mathbf{k}) = -\sum_{\mathbf{k}'} V(\mathbf{k}, \mathbf{k}') \frac{\Delta(\mathbf{k}')}{2E(\mathbf{k}')} \tanh\left(\frac{E(\mathbf{k}')}{2k_{\mathrm{B}}T}\right), \tag{1.1}$$

where $V(\mathbf{k}, \mathbf{k}')$ is the electron-electron pairing potential, $E(\mathbf{k})$ is the quasiparticle energy, k_{B} is the Boltzmann constant, and T the temperature. To satisfy this equation with a repulsive interaction ($V > 0$), a solution for the gap function must reverse sign between different parts of the Fermi surface connected by $\mathbf{k} - \mathbf{k}'$, i.e., $\Delta(\mathbf{k}) = -\Delta(\mathbf{k}')$. This can be achieved within a single Fermi sheet, e.g., if it's of d-wave symmetry. For FeSCs, we can argue that $\chi_s(\mathbf{q})$ (and therefore V) peaks around the nesting vector $\mathbf{Q}$. Hence, equation 1.1 can also be fulfilled when the gap

changes sign between the hole and electron pockets, which are nested by $\mathbf{Q}$. This naturally leads to the so-called $s^{\pm}$ (or extended s-wave) pairing state, where the gap is largely isotropic on each Fermi sheet but has opposite signs on the hole versus electron pockets. This state is fundamentally different from the sign-constant gap of conventional s-wave superconductors and also distinct from the d-wave symmetry found in the cuprates, where the sign change occurs for wavevectors connecting different parts of a single Fermi surface. Sign-changing nested Fermi sheets in FeSCs are supported by a wealth of experimental evidence [69–73].

In summary, the chain of reasoning, from the multi-band Fermi surface and its nesting instability to the spin-fluctuation-driven pairing mechanism and the resulting sign-changing $s^{\pm}$ gap, provides a robust framework for understanding the unconventional superconductivity in the FeSCs.

1.2 $EuFe_2As_2$: A Special Case in the 122 Family

1.2.1 Dual Magnetism: Itinerant Fe Spin-Density-Wave and Localized Eu Moments

$EuFe_2As_2$ (EFA) stands out among FeSCs as it contains an additional magnetic sublattice apart from the Fe atoms: it is the only 122 compound where the A site is a rare-earth element with a local moment. The Eu^{2+} ($4f^7$ configuration) carries a large spin $S = 7/2$ (orbital $L = 0$ for a $^8S_{7/2}$ Hund's rule ground state) [74], corresponding to a theoretical magnetic moment of $\approx 8\ \mu_B$. This gives rise to "dual magnetism" in $EuFe_2As_2$: the Fe sublattice orders in a stripe SDW at high temperature, and the Eu sublattice orders magnetically at a much lower temperature.

As discussed in Chapter 1.1.2, EFA has the typical FeSC behavior undergoing a coupled structural and magnetic transition at $T_{SDW} \approx 190$ K associated with the FeAs layers [75], where the high-temperature tetragonal structure (space group $I4/mmm$) becomes orthorhombic (space group $Fmmm$). Building on this, neutron diffraction studies by Xiao *et al.* [45] reveal that the Fe sublattice orders in a stripe-type SDW with wavevector $\mathbf{Q}_{Fe} = (1, 0, 1)$ in orthorhombic notation, corresponding

to spins in-phase along c across adjacent Fe layers. The Fe moments point along the longer orthorhombic a axis and reach a saturation value of $\sim 0.98\ \mu_B$/Fe.

The Eu^{2+} sublattice undergoes a separate magnetic transition at $T_{\mathrm{Eu}} \approx 19$ K [76], where the moments align along the a-axis with wavevector $\mathbf{k}_{\mathrm{Eu}} = (0, 0, 1)$ and a magnitude of $6.8\ \mu_B$/Eu [45]. This ordering corresponds to an A-type AFM structure, featuring ferromagnetic (FM) alignment within the ab planes and AFM coupling between adjacent planes, as confirmed by directional magnetic susceptibility, neutron scattering, and resonant X-ray scattering measurements [45, 77, 78]. The large separation in temperature and the observation that the Fe moment seems to stay robust when going through the Eu ordering temperature already indicates weak coupling between the sublattices [45]. This is further undermined by a field-induced AFM to FM transition of the Eu sublattice at roughly 1 T [79] without affecting the Fe-SDW. The ease with which the A-type AFM state can be canted and fully reoriented into a FM state by applied fields below 2 T also demonstrates weak interaction between Eu moments. Given the large spatial separation between the Eu layers, which precludes direct overlap of the $4f$ orbitals, this weak interaction is attributed to an indirect Ruderman–Kittel–Kasuya–Yosida (RKKY) exchange mediated by the conduction electrons of the FeAs layers [76].

In summary, undoped EFA has the Fe sublattice behaving much like other FeSC parents (semimetallic, SDW and tetragonal-to-othorombic transition below 190 K) and the Eu sublattice providing a separate localized-spin AFM order at 19 K. The ground state at zero field is thus an antiferromagnetically ordered Eu layer within an antiferromagnetically ordered FeAs matrix. Because of the small Eu-Eu exchange, the Eu order can be manipulated by external parameters (field, pressure, doping) without strongly disturbing the Fe order initially. This flexibility allows EFA to exhibit multiple interesting phases upon tuning, as is discussed next.

1.2.2 Superconductivity under Pressure and Doping

Given the analogy of EFA to other FeSCs, it was natural to explore whether superconductivity could be induced by suppressing the Fe-SDW. Indeed, studies

found that EFA can be tuned into a superconducting state upon application of pressure. Mechanical pressure of approximately 2 GPa can induce superconductivity, as shown by a drop in resistivity, however with a re-entrant magnetic phase hindering zero resistance [80]. Hydrostatic pressure, on the other hand, in the range form $2.5-3$ GPa can induce bulk superconductivity [81, 82]. In these findings, the magnetic ordering of Eu^{2+} moments was found to persist in the superconducting phase. The Eu^{2+} order remained intact under pressure, with T_{Eu} only slightly changed. Hence, at $\sim$3 GPa, EFA was interpreted as an *antiferromagnetic superconductor*, where below $T_{\mathrm{c}} \approx 30$ K the FeAs layers are superconducting, and below $T_{\mathrm{Eu}} \approx 20$ K the Eu layers order [81]. The nearly 100% shielding was obtained when the SDW and structural transition were fully suppressed by pressure. At pressures above 3 GPa, superconductivity is suppressed, while the T_{Eu} increases, and Eu moments even develop ferromagnetic alignment around 6 GPa, as revealed by XMCD measurements [83]. Coexisting AFM phases of both elements inside the superconducting dome have also been reported by ^{57}Fe nuclear forward scattering, where a modulated SDW has been seen at around 2.8 GPa [84]. In addition to applied pressure, a versatile route to induce superconductivity in EFA, as with other FeSCs, is through chemical substitution. Throughout this thesis, this process will be referred to using the terms "substitution" and "doping" interchangeably. This method offers a remarkable variety of pathways to tune the ground state, as substitutions can be performed on all three distinct crystallographic sites: on the Fe site, where Fe can be partially replaced by Co [85–87], Ir [88–91], or Ru [92–94]; on the As site, which is the focus of this thesis, where As is substituted by P [95–98], and on the Eu site, where partial replacement by K or Ca can induce superconductivity [99, 100]. Despite their different effects on charge through hole, electron or isovalent doping and on the local magnetic moments, for instance by dilution of Eu^{2+}, all these substitutions share a common outcome: superconductivity emerges as the tetragonal-to-orthorhombic structural phase transition is suppressed and the c-axis lattice parameter is reduced. This phenomenon, often referred to as a "collapsed tetragonal" state, draws a strong analogy to the effect of hydrostatic pressure, leading to the

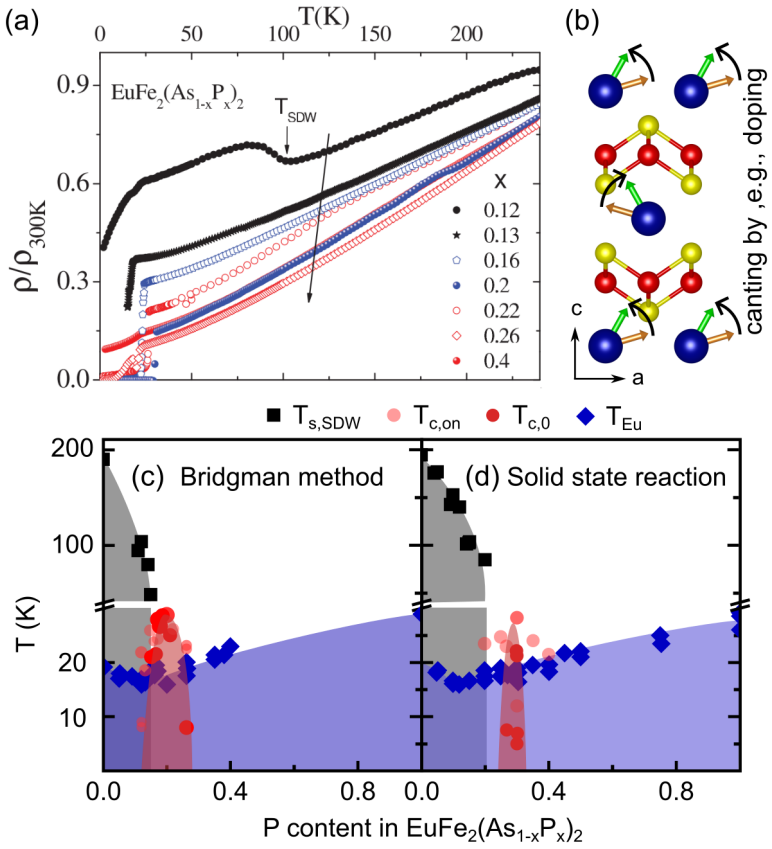


Figure 1.2: (a) Resistivity versus temperature for EFAP at different P concentrations, adapted from [101]. The SDW transition in the undoped compound is indicated by the arrow labeled T_{SDW}. At P/(As+P) = 0.2, the resistivity drops to zero, indicating superconductivity. (b) Schematic illustrating how the c-type AFM order of Fe can tilt toward ferromagnetic alignment, achievable via magnetic field, doping, or pressure, as discussed in the text below. (c) and (d) Phase diagrams showing the structural (T_s) and SDW (T_{SDW}) transition temperatures, the onset of superconductivity ($T_{c,\mathrm{on}}$), zero-resistance superconductivity ($T_{c,0}$), and the Eu magnetic ordering (T_{Eu}) as a function of P content for two different growth methods (Bridgman and solid-state reaction). Differences in the superconducting dome highlight the motivation for exploring alternative growth techniques such as MBE. Panels (c) and (d) were redrawn based on the review [16] to improve image quality, while faithfully representing the original data. The data points in these panels are from the primary sources: [96–98, 101–107] for the Bridgman method and [95, 108–111] for the solid state reaction.

concept of "chemical pressure" as the primary driver for inducing superconductivity. However, the picture of chemical pressure alone is an oversimplification. Comparing the isovalent substitution of P for As with the application of mechanical pressure on the parent compound reveals that superconductivity is induced more efficiently by P substitution than by equivalent hydrostatic pressure. This indicates that

other effects, such as local disorder or specific changes to the electronic band structure, also play a critical role [16].

As the focus of this thesis is on P-substituted samples, this system warrants a more detailed discussion. Superconductivity in $EuFe_2(As_{0.7}P_{0.3})_2$ was first reported by Ren *et al.* in 2009 [95], who observed a T_c of 27 K coexisting with Eu^{2+} ordering near 20 K. It should be noted that in comparison with subsequent reports, the precise phase diagram, particularly the doping level corresponding to the highest T_c, can have some variation, most likely due to differences in internal strain arising from specific crystal growth methods [16]. This variation is illustrated in Figure 1.2, adapted from Ref. [16], which compares phase diagrams obtained from different crystal growth methods. Primary sources of the data are provided in the figure caption.

The magnetic state of the Eu^{2+} sublattice in this doped system is particularly complex. While the parent compound is an A-type antiferromagnet, Mössbauer and low-field magnetometry studies on P-doped crystals have revealed a progressive canting of the Eu^{2+} moments, leading to an increasingly strong net FM response at higher doping levels [96, 101, 108]. With this, P-doped $EuFe_2As_2$ (EFAP) is widely accepted as a *ferromagnetic superconductor* [16, 98, 110]. This evolution from A-type AFM towards a canted FM state is thought to be driven by changes in the RKKY interaction. As the Fe-SDW is suppressed with P substitution, the Fermi surface is modified, which in turn alters the long-range RKKY coupling between the Eu^{2+} moments [103, 106, 112].

The direct conflict between superconductivity, which expels magnetic fields, and the ferromagnetism of the Eu^{2+} ions, which generates an internal field, forces the material into subtle compromise states as first directly imaged and interpreted by Stolyarov *et al.* [113]. Just below the Eu ordering temperature, the system first enters a domain Meissner state (DMS), where nanoscale magnetic domains of alternating magnetization spontaneously form and largely cancel one another's magnetic flux. As the temperature decreases further and the Eu magnetism strengthens, the local internal field may exceed the critical field H_{c1} and can

no longer be efficiently compensated by a DMS. This triggers a transition into the domain vortex-antivortex state (DVS), where the superconductor accommodates the field by nucleating dense arrays of partially flux-compensating vortices and antivortices. The existence of these modulated states as bulk phases was later confirmed by small-angle neutron scattering [114].

Building on this picture, Wilcox *et al.* [115] later showed that the vortex dynamics are influenced by the magnetic domain landscape. Just below the Eu ordering temperature, in the DMS, they identified "vortex polarons", vortices that locally deform magnetic domains to lower their energy, which strongly enhance pinning near the magnetic transition. As the temperature is reduced further, the system transitions into the DVS, where the vortex polaron mechanism fades and the dynamics become dominated by giant flux creep, driven by thermally activated vortex–antivortex annihilation at domain walls. Importantly, they also predicted that thinner films should host narrower domains, strengthening vortex-polaron pinning over a broader temperature range and offering a promising route to engineer high-current performance in superconducting applications [115]. These insights naturally motivate a discussion of thin-film growth, which form the focus of the following chapter.

1.3 Motivation and Outline

Synthesis of FeSCs as thin films has matured into a successful field, with representatives from all major structural families now realized by techniques such as PLD and MBE, as documented in several reviews [6, 116–118]. Within the 122 family, $BaFe_2As_2$ has emerged as a particularly important testbed due to its stable growth. This reliability has paved the way for a second generation of experiments that leverage the unique capabilities afforded by thin films.

One primary advantage of thin films is the ability to manipulate lattice strain. By growing a film on a substrate with a slight lattice mismatch, one can controllably alter the electronic structure and superconducting properties, which are highly sensitive to parameters such as the Fe–As–Fe bond angle. This approach can even

induce superconductivity without chemical doping, as demonstrated in $BaFe_2As_2$ thin films under tensile strain [119].

As already mentioned in the introduction, the most dramatic example of thin-film potential is found in monolayers of FeSe grown on an $SrTiO_3$ substrate. In this case, the critical temperature is enhanced to over 65 K [13, 35], a huge leap from the bulk value of 8 K [29]. ARPES studies revealed a complex interplay of strain-induced SDW and charge transfer from oxygen-vacancy-induced states of the substrate [35]. Moreover, the ground state is highly sensitive to thickness: a single monolayer is a high-T_c superconductor, two monolayers are semiconducting [12], and thicker films revert to a metallic SDW state [35].

Despite this significant progress, a notable gap in this landscape has been the absence of thin films of EFAP. As established in the previous chapter, the intrinsic coexistence of two distinct magnetic sublattices makes this material uniquely compelling, particularly given the rarity of ferromagnetic superconductors. The successful synthesis of this material via MBE is therefore the central goal of this thesis, as it provides a platform to explore its rich physics using techniques that are only possible in the thin-film regime.

First, the ability to pattern films using lithography enables advanced transport measurements. Fabricating Hall bars allows for a precise determination of the charge transport properties. Second, patterning the films into device geometries such as superconducting rings enables direct probing of the pairing symmetry via the Little-Parks (LP) effect, as spin-triplet pairing could manifest in half-quantum LP oscillations (more details given in Chapter 3.5). While $s^{\pm}$ symmetry is the prevailing consensus for most FeSCs, the intrinsic coexistence of ferromagnetism and superconductivity in a single compound presents a unique scenario where short-range spin-triplet pairing, analogous to that sought in complex SC/FM heterostructures, might be considered [120]. While typically dismissed more by Occam's razor than by direct experimental counter-evidence, thin-film devices offer a more direct test. Finally, high-quality thin films are the essential first step towards creating heterostructures and quantum devices. One could envision

interfacing EFAP with other materials to study spin currents or spin-polarized Andreev reflection, ultimately harnessing its unique properties for applications in next-generation superconducting spintronics.

Following the motivation outlined above, the thesis is organized to present the results and analyses that address these objectives. Chapter 2 describes the experimental methods for thin-film growth, characterization, and device fabrication. Chapter 3 introduces the theoretical toolkit, including multi-band superconductivity, vortex dynamics, and the LP effect. Chapter 4 presents the first successful thin film growth of EFA and EFAP by MBE. Chapter 5 discusses magnetometry measurements of the films, and Chapter 6 reports transport studies in patterned devices, including an analysis of the LP oscillations. Finally, Chapter 7 summarizes the findings and provides a brief outlook.

2 Methodology

This chapter provides a comprehensive overview of the experimental and characterization techniques employed in this work. It begins with molecular beam epitaxy (MBE), including its in-situ monitoring capabilities, starting from general principles and then focusing on the specific custom MBE system used for film growth.

Following growth, the structural and compositional properties of the films are examined. The techniques used for this purpose include:

- X-ray diffraction (XRD)
- Energy-dispersive X-ray spectroscopy (EDX)
- Transmission and scanning transmission electron microscopy (TEM/STEM)
- Rutherford backscattering spectrometry (RBS)

Magnetic properties are subsequently assessed, employing:

- Superconducting quantum interference device (SQUID) magnetometry
- X-ray magnetic circular dichroism (XMCD)

Finally, electron beam lithography (EBL) is introduced, which was applied to fabricate devices such as Hall bars and superconducting rings.

This chapter therefore lays out the full workflow from film growth to device fabrication, providing the methodological foundation for the results presented in later chapters.

It should be noted, that scanning tunneling microscopy (STM) and spectroscopy (STS) were also employed, but are not discussed in this chapter, as their use was limited to a brief surface morphology study with the room-temperature STM setup and a small set of low-temperature measurements only presented in the additional materials chapter.

Contents

2.1 Molecular Beam Epitaxy: Principles and Practice . . 20
2.2 Structural and Compositional Characterization 29
2.2.1 Principles of X-ray Diffraction 29
2.2.2 Rutherford Backscattering Spectrometry 30
2.2.3 Energy Dispersive X-ray Spectroscopy and Elemental Analysis 32
2.2.4 Transmission and Scanning Transmission Electron Microscopy 35
2.3 Magnetic Characterization 38
2.3.1 Fundamentals of SQUID Magnetometry 38
2.3.2 X-ray Magnetic Circular Dichroism 41
2.4 Device Fabrication by Electron Beam Lithography . . 43

2.1 Molecular Beam Epitaxy: Principles and Practice

An MBE system allows thin film growth by epitaxial deposition of crystalline materials with atomic-layer precision [121]. For this, beams of atoms or molecules from heated elemental sources are directed onto a heated substrate in ultra-high vacuum (UHV) conditions, where they condense and arrange into a crystal lattice following the template of the substrate. The term *epitaxy* refers to exactly this ordered growth of the film, where the crystal lattice of the depositing material aligns with that of the substrate. As the beams travel through an UHV environment (with base pressures of $\approx 10^{-10}$ mbar) their mean free path ℓ of atoms is far greater than

the chamber dimensions. This can be inferred from the expression for ℓ:

$$\ell = \frac{k_B T}{\sqrt{2}\pi d^2 P}, \tag{2.1}$$

where k_B is the Boltzmann constant, T the gas temperature, d the effective atomic/molecular diameter, and P the pressure. This typically corresponds to tens to hundreds of kilometers, ensuring that the molecular beams travel ballistically to the substrate without collisions or scattering. One of the key advantages of MBE is the exceptional control it offers over film composition and thickness at the atomic scale. Growth rates in MBE are typically very low (on the order of one atomic monolayer per seconds), which, combined with the use of mechanical shutters on each source, permits abrupt starting and stopping of deposition and the creation of atomically sharp interfaces. Low deposition rates and the UHV environment minimize impurity incorporation. Because of these features, MBE is suited for high-quality, single-crystalline growth of complex compounds. Especially, for materials containing volatile elements such as As and P, MBE provides good flux control and the ability to maintain a non-interacting overpressure of these elements during growth, which can be crucial for stoichiometric incorporation. As a result, MBE has been successfully employed to grow high-quality epitaxial films of FeSCs (as outlined in chapter 1.1.2), where controlling the volatile pnictogen content is critical for obtaining the desired phase. Before describing the custom MBE system and its key in-situ tools in detail, the following section provides a brief overview of the different thin film growth mechanisms.

Growth Modes: A Balance of Thermodynamics and Kinetics

While MBE can be viewed thermodynamically as an open system, its conditions are far from equilibrium. Therefore, the film's properties are governed not simply by minimizing the Gibbs free energy, but by kinetic processes: fluxes, surface diffusion, incorporation, and desorption [121]. The balance between the adatom–substrate and adatom–adatom interaction energies leads to three fundamental growth modes, as illustrated in Figure 2.1:

- **Frank-van der Merwe (Layer-by-layer):** Occurs on the first layer when adatoms bind more strongly to the substrate than to each other. To continue growing in this manner, the balance of energies must consistently favor new atoms spreading out over the existing film surface rather than clumping together into islands. This is the most desirable mode for atomically smooth surfaces and high crystalline quality.

- **Volmer-Weber (Island):** Dominates when adatoms prefer to bind to each other, leading to the formation of 3D islands.

- **Stranski-Krastanov (Layer-plus-island):** An intermediate case where a 2D layer first forms before strain accumulation triggers the formation of 3D islands.

Even within the Frank-van der Merwe mode, growth can proceed via two competing kinetic processes: *step-flow* or *2D nucleation*. In the first, adatoms diffuse to and incorporate at existing terrace edges, so growth proceeds mostly from these edges, and the surface remains step-like at all times. In the second, adatoms on terraces do not reach the terrace edge before forming islands once a critical density is attained. These islands then act as new pinning centers. Nevertheless, as long as conditions are balanced, the growth can still remain coherent, maintaining the overall 2D layer-by-layer character. The dominant process is determined by the competition between surface diffusion and the incident atomic flux.

A Quantitative Model for Growth Kinetics

The kinetic processes underlying MBE growth can be described using atomic transport equations. In the following, the equations and parameter definitions are directly derived from and closely follow the notation used in references [122–124], where they are discussed for GaAs, but the formulation is generally applicable to other material systems.

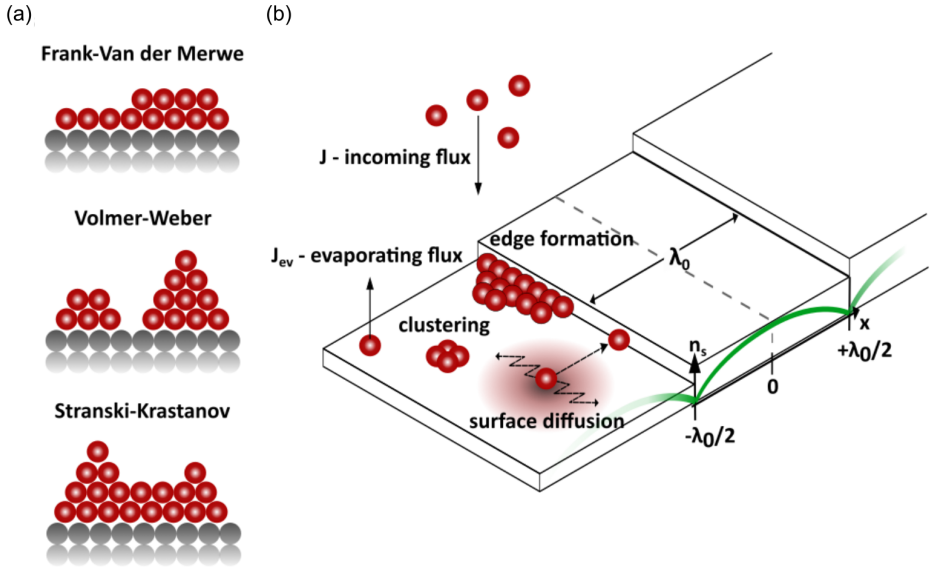


Figure 2.1: (a) Illustration of fundamental growth modes in MBE: Frank–van der Merwe (layer-by-layer), Stranski–Krastanov (layer-plus-island), and Volmer–Weber (island growth). (b) Schematic depiction of the atomic processes at the surface. The incoming flux of atoms (J) deposits atoms on the surface. Some atoms diffuse along a terrace of width λ_0, with the adatom density $n_\mathrm{s}(x)$ following a parabolic profile (highest at the terrace center and decreasing to a minimum at the step edges located at $x = \pm\lambda_0/2$). Other atoms are incorporated at the step edges or form nucleation sites on the terrace, while a fraction desorbs from the surface (flux J_ev).

The mean residence time of an adatom on the surface, τ_s, follows an Arrhenius relation:

$$\tau_\mathrm{s} = \nu_s^{-1}\, e^{E_A/k_\mathrm{B}T}, \tag{2.2}$$

where E_A is the activation energy for desorption, ν_s is the attempt frequency, T is the absolute temperature, and k_B is the Boltzmann constant. The surface adatom concentration, n_s, evolves due to deposition, desorption, and diffusion. The net flux of atoms arriving at the surface, J_v, is given by the difference between the incoming source flux J and the flux of atoms that immediately evaporate back into the vapor, J_ev:

$$J_\mathrm{v} = J - J_\mathrm{ev}. \tag{2.3}$$

Surface diffusion along the step growth direction, defined as x, is described by Fick's

law:

$$J_s = -D_s \frac{dn_s}{dx}, \tag{2.4}$$

where D_s is the surface diffusion coefficient, J_s is the surface diffusion flux, and dn_s/dx is the spatial gradient of the adatom concentration along x. Under steady-state conditions, the diffusion equation can be expressed as:

$$(D_s\tau_s)^2 \frac{d^2 n_s}{dx^2} - \Big(n_s(x) - J\tau_s\Big) = 0, \tag{2.5}$$

Solving for a terrace of width λ_0 with $n_s(\pm\lambda_0/2) = n_{\text{step}}$ gives

$$n_s(x) = (n_{\text{step}} - J\tau_s)\,\frac{\cosh(x/\lambda_s)}{\cosh(\lambda_0/(2\lambda_s))} + J\tau_s, \tag{2.6}$$

where $\lambda_s = \sqrt{D_s\tau_s}$ is the diffusion length. In the common case of negligible desorption ($\lambda_s \gg \lambda_0$), this reduces to a parabolic profile:

$$n_s(x) \approx n_{\text{step}} + \frac{J\lambda_0^2}{8D_s}\left(1 - \frac{4x^2}{\lambda_0^2}\right). \tag{2.7}$$

The supersaturation $\alpha(x) = n_s(x)/n_s^0$, with n_s^0 being an equilibrium surface

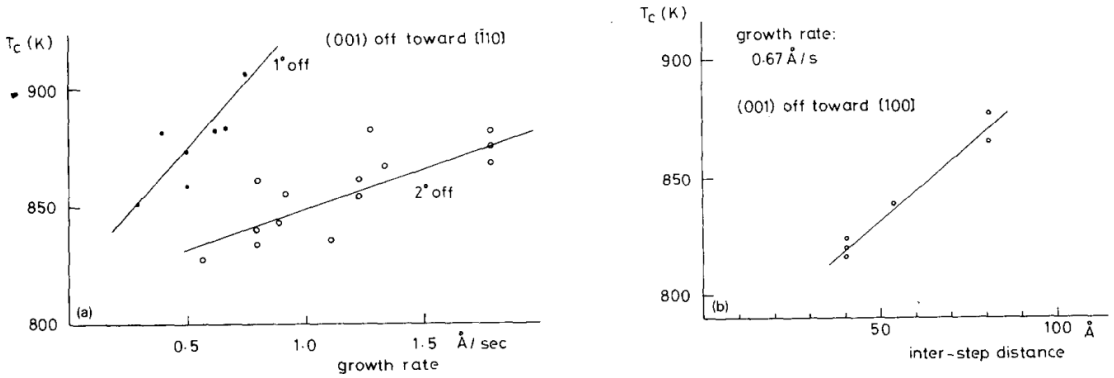


Figure 2.2: Dependence of the critical temperature T_c on growth rate (left) and step spacing (right) for GaAs, shown for growth on two substrates with slightly different miscut angles (1° and 2° off, as indicated). Figure from [125]. T_c marks the transition from step-flow growth to formation of nuclei before being integrated in a step. With higher growth rates or larger terrace widths, higher substrate temperatures is necessary to sustain step-flow.

concentration, determines whether nucleation occurs. If the maximum α at the terrace center exceeds a critical threshold α_c, 2D nucleation dominates over step-flow growth. This transition is exemplified in studies of GaAs growth (Figure 2.2), where

higher temperatures are required to maintain step-flow at faster growth rates or on wider terraces [125]. As will be shown in the results section on EFAP growth (Chapter 4.2), a very similar dependence of growth modes on substrate temperature and deposition rate is observed for successful epitaxial samples.

Description of the Custom-Built MBE System

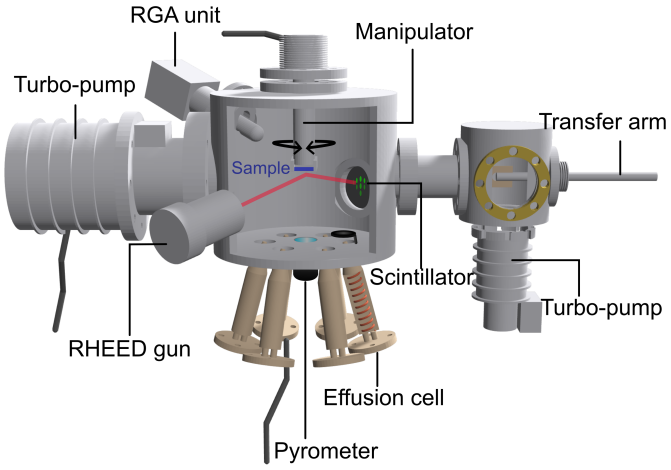


Figure 2.3: CAD model of the MBE, created for illustrative purposes showing the key components and their arrangement. The central UHV main chamber is evacuated by a large turbo-molecular pump. Material deposition is achieved using multiple thermal effusion cells, shown with their electrical wiring. The substrate is mounted on a high-precision manipulator, which allows for rotation and vertical translation, and includes integrated sample heaters. Real-time growth monitoring is performed with a RHEED system, consisting of an electron gun and a phosphor screen. The RGA, enclosed in a liquid nitrogen cryo-shroud, can be inserted to analyze chamber contaminants and fluxes during growth. Samples are introduced into the UHV environment via a separately pumped load-lock chamber, equipped with its own turbo pump and a viewing window.

All thin films in this work were grown using a custom-built MBE system designed for pnictide materials. The system consists of a stainless-steel UHV growth chamber connected to a load-lock for sample introduction. The growth chamber is evacuated by a combination of turbo-molecular and ion pumps, achieving a base pressure on the order of $\approx 10^{-10}$ mbar (with pressure in the low 10^{-9} mbar range typically during active growth). The chamber is equipped with several effusion cells (Knudsen cells) for evaporating the constituent elements of EFAP. High-purity Eu, Fe are placed in standard effusion cells, while P and As are provided from GaP and

GaAs by specialized trapping cells, which are utilized to minimize the release of pyrolytic white phosphorus during evaporation and ensure a high P_2-to-P_4 and As_2-to-As_4 ratio ($\sim$100) [126]. The decomposition cell is provided with a PBN cap for Ga trapping. Each effusion cell is mounted on a water-cooled copper flange and is individually controlled by thermocouple feedback controllers, allowing precise regulation of the cell temperatures and hence the fluxes of each element. A rotating substrate holder is positioned at the center of the chamber, facing the effusion cells at a calibrated distance to ensure a uniform flux distribution over the substrate. The substrate holder includes a resistive heater capable of heating substrates up to about 800 °C and a thermocouple embedded near the substrate position for temperature monitoring. For accurate substrate temperature measurement above $\sim$500 °C, an optical pyrometer is also used (through a viewport) to account for radiative heating, variations in emissivity, and mostly the fact that thermocouples are not in direct contact with the sample holder. The entire system is interlocked and automated via computer control for safe handling of the volatile As and P sources, including pneumatically controlled shutters for each cell. Three critical in-situ tools provide the feedback necessary for precise growth:

Reflection High-Energy Electron Diffraction (RHEED): RHEED is a standard in-situ technique used for monitoring the surface of thin films during MBE growth [127]. The method uses a high-energy electron beam ($10 - 30$ keV) directed at the sample at a grazing incidence angle (usually $1° - 3°$). The resulting diffraction pattern, which arises from the elastic scattering of electrons from the top few atomic layers, is projected onto a phosphor screen and recorded by a CCD camera. The condition for constructive interference is given by the Laue condition, $k_i - k_o = G$, where G is a reciprocal lattice vector. This can be visualized using an Ewald sphere construction, as shown in Figure 2.4(a). Because the electrons only probe a 2D surface, the reciprocal lattice consists of rods instead of points. The high energy of the electrons creates an Ewald sphere with a radius much larger than the reciprocal lattice spacing. As a result, the sphere's intersection with

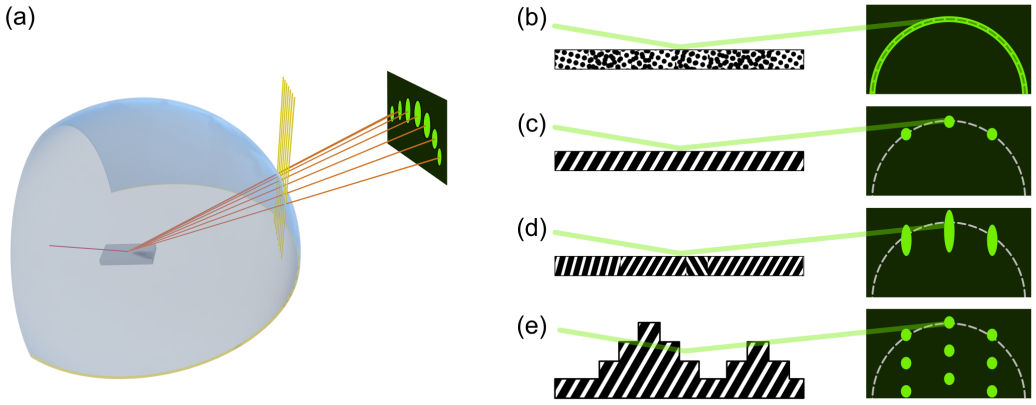


Figure 2.4: (a) Schematic of RHEED geometry. A high-energy electron beam (red) impinges at a grazing angle on the sample (gray). The Ewald sphere (blue) intersects the reciprocal lattice rods (yellow), generating diffraction spots projected onto the phosphor screen. (b)–(e) Illustration of RHEED patterns for different crystalline quality and surface morphologies: (b) polycrystalline, showing full Laue rings; (c) ideal single crystal, producing sharp point-like intersections; (d) realistic single crystal with small imperfections, resulting in streaked rods; (e) 3D surface features, causing point-like diffraction due to breaking of streaks along depth.

the array of reciprocal lattice rods is approximately planar, producing diffraction spots on Laue rings on the screen.

The RHEED pattern primarily reflects the surface morphology and crystal quality. An atomically flat, well-ordered surface produces sharp truncation rods. In practice, small misalignments or lattice variations broaden these rods. The nearly planar intersection of the Ewald sphere with these broadened truncation rods then produces the characteristic streaky features observed in RHEED images. When such streaks persist during growth, they are interpreted as the hallmark of two-dimensional, layer-by-layer growth. Conversely, a spotty pattern indicates three-dimensional island growth, as the electrons can then transmit through the islands and diffract from a 3D lattice, breaking the reciprocal rod condition. Polycrystalline samples produce complete Laue rings as reciprocal lattice vectors are rotated by random grain orientations. An illustration of these patterns can be found in Figure 2.4(b–e).

Beyond overall morphology, RHEED is also sensitive to surface reconstructions, where the outermost atoms rearrange into patterns different from the bulk lattice [127]. A classic example is the (2×4) reconstruction of GaAs(100), where

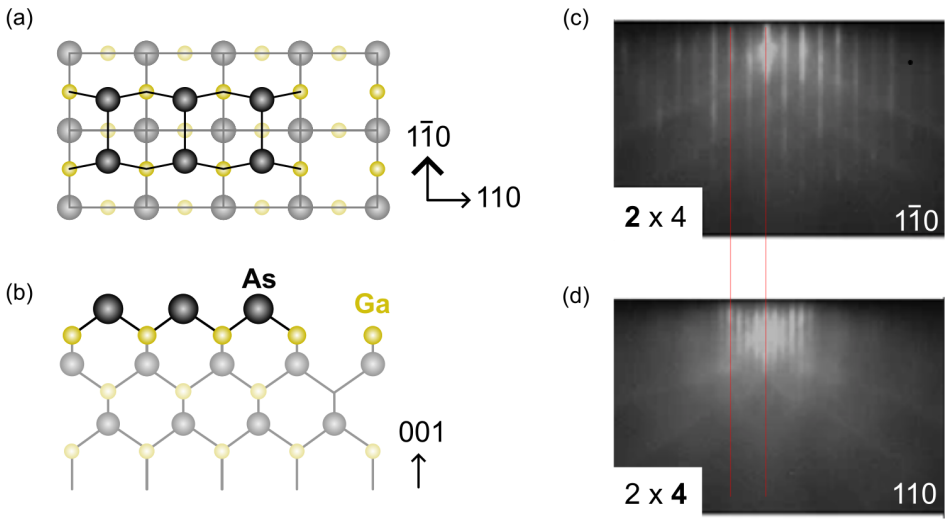


Figure 2.5: Representative schematic of the GaAs(100) $\beta(2 \times 4)$ surface reconstruction. (a) Projection along [001], showing the surface arrangement in the [1$\bar{1}$0]–[110] plane, with one missing As atom per 2×4 surface unit relative to the bulk lattice. (b) Projection along [1$\bar{1}$0], showing the same structure in the orthogonal [001]–[110] plane. The surface unit cell is thus twice the bulk spacing along [1$\bar{1}$0] and four times along [110]. (c) and (d) show corresponding RHEED patterns from [127], where the enlarged surface periodicity produces additional half-order streaks in (c) and quarter-order streaks in (d).

various arrangements, such as As vacancies or dimerizations, can lower the surface energy [128]. Among the many possible reconstructions, there are, for example, configurations that double the surface unit cell in one direction and quadruples it in the other, producing additional diffraction streaks between the primary ones. Identifying such reconstructions is significantly more challenging in complex, multi-element compounds. Even in a relatively simple binary system like GaAs, multiple distinct arrangements can yield similar (2×4) RHEED patterns, of which only one representative case ($\beta(2 \times 4)$) is shown here in Figure 2.5.

Generally, while the spacing between RHEED streaks is related to the in-plane lattice parameters, the technique is mainly used as a qualitative monitoring tool rather than for precise quantitative measurements, for which techniques like XRD or TEM are better suited.

Quartz Crystal Microbalance (QCM): A quartz crystal sensor measures deposition flux via frequency shifts:

$$\Delta f = -\frac{2f_0^2}{A\sqrt{\rho_q \mu_q}} \Delta m, \tag{2.8}$$

where f_0 is the fundamental frequency, A the active area, and ρ_q, μ_q are the quartz density and shear modulus. The QCM readings were calibrated against cross-sectional TEM measurements on selected samples, providing reliable thickness and stoichiometry control for subsequent growths.

Residual Gas Analyzer (RGA): A quadrupole mass spectrometer, continuously monitors the partial pressures of gas species within UHV chamber. This provides a real-time compositional analysis of the vacuum environment, crucial for identifying contaminants like water (H_2O), nitrogen (N_2), and hydrocarbons, thereby ensuring the purity of the growth environment. It is also used for leak detection, especially after opening the chamber, e.g., for insertion of new material. The quadrupole analyzer can be positioned to directly measure the flux from effusion sources in terms of their Beam Equivalent Pressure (BEP). This capability enables precise calibration of elemental flux ratios (e.g., the P/As ratio).

2.2 Structural and Compositional Characterization

2.2.1 Principles of X-ray Diffraction

XRD is a widely used, non-destructive method to study the crystal structure, phase purity and general quality of crystal specimen. The working principle relies on elastic scattering of X-rays from the periodic arrangement of atoms in the crystal. According to Bragg's law, constructive interference occurs when the path length between X-rays scattered from successive planes is roughly an integer multiple of the wavelength:

$$2d \sin\theta = n\lambda, \tag{2.9}$$

where d is the interplanar spacing, θ is the incident angle, λ is the X-ray wavelength, n is the order of reflection. In the case of thin films, measurements are often performed in a fixed θ–2θ geometry, scanning along the $(00l)$ direction. With this setup, diffraction peaks can appear when the scattering vector $\mathbf{Q} = \mathbf{k} - \mathbf{k}'$ matches a reciprocal lattice vector $\mathbf{q}_{00l}$. This provides information about the corresponding interplanar distances according to Bragg's law. For a comparison with theory, it

is usually necessary to take into account atomic form factors, structure factors, and thermal effects. In practice, experimental patterns are often compared with databases of measured or simulated diffraction data for similar materials.

2.2.2 Rutherford Backscattering Spectrometry

To determine the composition of EFAP films, RBS was employed. The RBS is particularly well suited for quantifying heavy elements such as Eu, Fe, and As, since their scattering cross sections are large and their backscattering edges are well separated in energy. The principal limitation in this system is the determination of P, which was only possible for thicker samples with high P-content. The P signal overlaps with the substrate contribution, in particular the Ti edge from the underlying STO, as we will see. For a better resolution of the P content, relative P/As ratios were afterwards analyzed by EDX, which will be introduced in the next section. The following description of the technique's principles is based on well-regarded text of Chu, Mayer and Nicolet [129].

In RBS, a beam of high energy (MeV range) $^4He^+$ is directed at the sample, and ions scattered at a fixed angle θ are detected with a silicon surface barrier detector. The kinematic factor K determines the energy E_1 of a projectile of mass M_1 and initial energy E_0 elastically scattered from a target atom of mass M_2:

$$E_1 = K(\theta, M_1, M_2)\, E_0, \tag{2.10}$$

with

$$K(\theta, M_1, M_2) = \left(\frac{\sqrt{M_2^2 - M_1^2 \sin^2\theta} + M_1 \cos\theta}{M_1 + M_2} \right)^2 . \tag{2.11}$$

This dependence allows to determine between elements of different mass, as heavier atoms produce higher-energy backscattering edges. The scattering probability is given by the Rutherford cross section:

$$\frac{d\sigma}{d\Omega} = \left(\frac{Z_1 Z_2 e^2}{16\pi\epsilon_0 E_0} \right)^2 \frac{1}{\sin^4(\theta/2)}, \tag{2.12}$$

where Z_1 and Z_2 are the projectile and target atomic numbers, e is the elementary charge, and ϵ_0 is the vacuum permittivity. This term directly governs the signal

intensity of a given element. For a slice of material of thickness dx containing atoms at density N, the yield is:

$$dY = N(x)\,\frac{d\sigma}{d\Omega}(E,\theta)\,\Phi\,d\Omega\,dx, \tag{2.13}$$

with Φ the incident ion fluence and $d\Omega$ the detector solid angle. The total detected spectrum is then obtained by integrating over all depths:

$$Y(E) = \int N(x)\,\frac{d\sigma}{d\Omega}(E,\theta)\,\Phi\,d\Omega\,dx, \tag{2.14}$$

subject to the relation between depth and detected energy. Depth information is introduced through the stopping power $S(E)$, which describes the mean energy loss per unit distance:

$$S(E) = -\frac{dE}{dx}. \tag{2.15}$$

An ion scattered from depth x exits the sample with reduced energy:

$$E(x) = KE_0 - \int_0^x S(E)\,dx', \tag{2.16}$$

so that heavier elements give well-defined edges at higher energies, while lighter elements produce weaker signals. Generally, the determination of P is possible by RBS, however, for the reported EFAP films grown on STO this becomes problematic. As shown in Figure 2.6, RBS is most reliable for the heavier elements of our material such as Eu, Fe, and As, since their cross sections are large and the corresponding peaks are well separated. In contrast, the P signal appears at lower energies and overlaps with the Sr signal from the STO substrate, which limits its quantitative determination.

The experimental spectra were analyzed using the program SIMNRA [130]. SIMNRA employs deterministic forward modeling: a sample is represented as a stack of discrete layers with defined thicknesses and stoichiometries. The program calculates the expected scattering yield for each layer using the cross sections above, applies energy loss according to databases of stopping powers. The simulated spectrum is then visually compared with the measured one, and parameters such

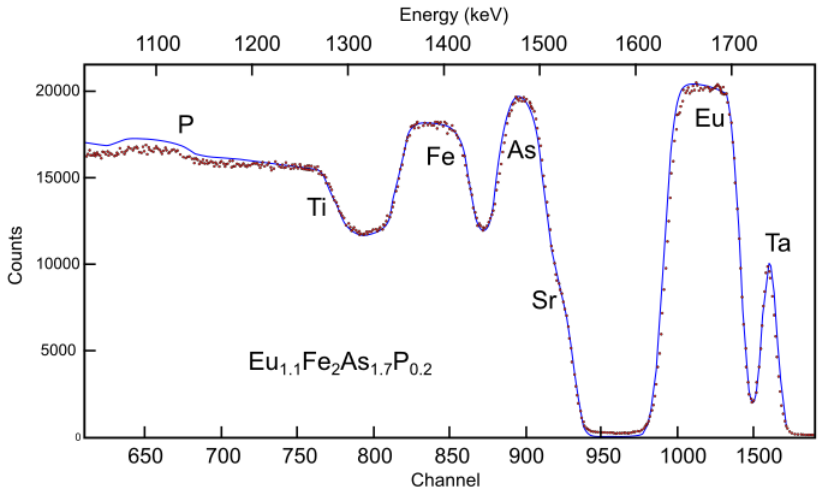


Figure 2.6: RBS results showing experimental points and a SIMNRA simulation (blue line). Peaks are labeled according to their corresponding elements. The P peak is very small and overlaps with the substrate Ti edge, making the fit less precise. The resulting stoichiometry is $Eu_{1.1}Fe_2As_{1.7}P_{0.2}$, with a high uncertainty for P, as variations between 0.05 and 0.4 produce similarly good fits. The figure has been fully recreated and vectorized for higher quality, while remaining faithful to the original data.

as layer thicknesses and elemental concentrations are adjusted iteratively until good agreement is achieved.

2.2.3 Energy Dispersive X-ray Spectroscopy and Elemental Analysis

EDX is an analytical technique used to determine the elemental composition of materials, typically integrated into electron microscopes. The following description of the principles and quantification methods of EDX is based on the book by Goldstein *et al.* [131].

The principle of EDX relies on the characteristic X-ray emissions that occur when a material is bombarded with a high-energy electron beam. In electron microscopes, the primary electrons can knock out core electrons from atoms in the sample, with energies typically $5 - 30$ keV in scanning electron microscopes (SEM) and $100 - 300$ keV in TEM, respectively. When a higher-shell electron fills the core-hole, an X-ray photon is emitted with energy equal to the difference in energy levels. These X-ray energies are characteristic of each element (resembling the element's atomic fingerprint, e.g., Fe K$\alpha \approx 6.4$ keV, As K$\alpha \approx 10.5$ keV, Eu

L lines around 5.8 – 6.5 keV, etc.). By measuring the energies and intensities of these X-rays with an energy-dispersive detector, one can identify which elements are present and estimate their relative abundances.

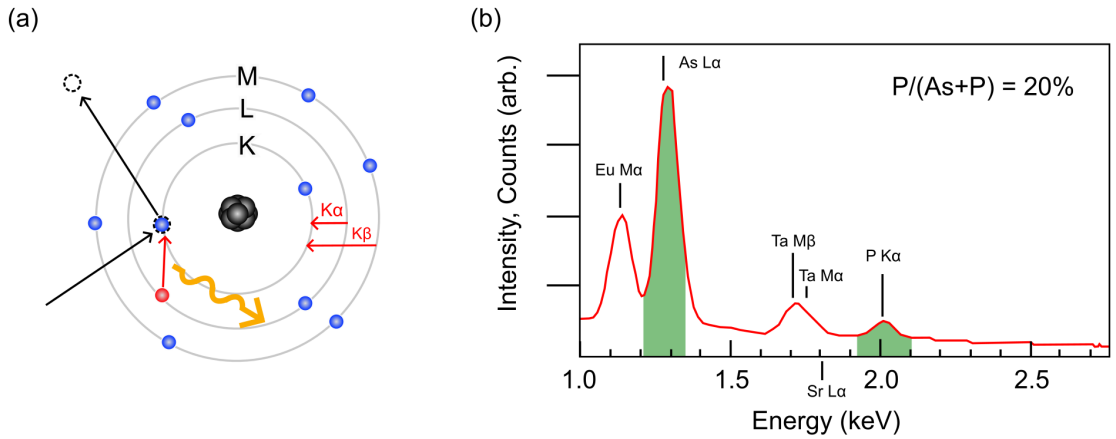


Figure 2.7: (a) Schematic illustration of the EDX process, showing X-ray induced electronic transitions. An incident X-ray ejects an inner-shell electron (here from the K shell), followed by relaxation of an outer electron (here L shell) that emits a characteristic photon (Kα). Other transitions from higher shells would be named Kβ, Kγ, and so on. Other effects, e.g., Auger electrons or double transitions, are omitted for clarity. (b) EDX spectrum of an 80 nm sample collected with a 4 keV primary beam. Main spectral features corresponding to As, P, Eu, and Ta are indicated. Analysis of the simulated spectrum, performed using the JEOL EDS microanalysis system software for the JSM-IT810 series SEM, gives a P/(As+P) ratio of 20%.

To quantify the elemental concentration C_i, the k-ratio is first calculated from the raw intensity I_i at energy position i by comparing the net peak counts of the sample to those of a standard peak count I_{std} of known concentration C_{std}:

$$k_i = \frac{I_i^{\text{sample}}}{I_i^{\text{std}}} = \frac{C_i}{C_{\text{std}}}. \tag{2.17}$$

This formula does not yet account for several important corrections. First, heavier elements backscatter electrons more efficiently, reducing the number of electrons available for inelastic scattering and thus lowering the probability of characteristic X-ray excitation. This effect depends on the atomic number Z and is corrected by the Z-correction. Second, once an X-ray is generated inside the sample, it may be partially absorbed before reaching the detector; this effect is corrected by the A-correction for absorption. Finally, emitted X-rays can excite other atoms

in the sample, producing secondary X-rays. This enhancement is accounted for by the F-correction for fluorescence. With these, the concentration is

$$C_i = C_{\text{std}} \cdot k_i \cdot Z_i \cdot A_i \cdot F_i. \tag{2.18}$$

Finally, the atomic fraction of element i can be obtained by normalizing over all elements. Prior to analysis, the spectrum is corrected for background contributions such as bremsstrahlung, and overlapping peaks are deconvoluted. In this work, EDX provides complementary compositional information to RBS, particularly for lateral uniformity and phase identification. It has been used mainly for quantification of P, as its identification in RBS was difficult due to overlap with the substrate signal, as described before. In most commercial EDX systems standardless quantification is employed, in which the role of the standard is replaced by fundamental physical formulas and atomic databases. Here, the expected X-ray generation efficiency for a pure element is calculated from tabulated atomic data such as ionization cross sections, fluorescence yields, and mass attenuation coefficients, combined with the instrument geometry and detector calibration. The raw peak intensities are then corrected using ZAF and compared to a model by iterative fitting.

Figure 2.7(b) shows the EDX count spectrum of an 80 nm sample in the 1-3 keV range, measured with a primary beam energy of 4 keV. The low acceleration voltage was chosen to limit the probing depth and thereby suppress overlap with substrate peaks. In this region, distinct features can be identified: the As Lα peak at 1.29 keV, the P Kα peak around 2 keV, the Eu Mα peak near 1.1 keV, and several Ta M transitions clustered around 1.7 keV. These constitute the dominant contributions to the shown spectrum range. Additional weaker transitions (other Eu/Ta M-lines and minor satellite features) are present but are buried in the background and not discussed further here. In practice, the system fits all detectable transitions to extract the overall stoichiometry. For the purposes of this work, the focus lies on the spectral region shown, which enables reliable determination of the P/(As+P) ratio. This is particularly significant because P is the lightest element in the compound and contributes the smallest mass fraction, making it generally challenging to detect.

The use of low-energy EDX was therefore crucial, as it enhanced the visibility of the P Kα line and allowed for a quantification. Elements such as Eu and Fe do exhibit peaks below 1 keV (not displayed here), but quantitative analysis typically relies on additional higher-energy K lines, e.g. Fe K at > 6 keV. At such beam energies, stronger substrate signals appear and especially the P signal becomes obscured. Hence, as already descibed, RBS was employed for $EuFe_2As_2$, though here P proved challenging due to the Ti edge. In summary, EDX and RBS together provided a complete elemental characterization scheme.

2.2.4 Transmission and Scanning Transmission Electron Microscopy

TEM is employed in this work primarily for structural and compositional characterization of EFAP films at the atomic level. The technique relies on the interaction of high-energy electrons with the sample. Electrons emitted from a field emission source possess wavelengths significantly shorter than visible light, allowing imaging at sub-nanometer resolution. The electron beam is focused and manipulated using a series of electromagnetic lenses, allowing various operational modes depending on the lens configuration. The following overview of fundamental TEM principles and modalities is primarily based on the comprehensive textbook by Williams and Carter [132].

When a parallel electron beam illuminates a crystalline specimen, two fundamental imaging modalities can be distinguished by considering the paths of electrons deflected by the sample, as illustrated in Figure 2.8. Electrons scattered by a well-defined angle can interfere to produce a diffraction pattern, which encodes information on the in-plane lattice parameters. These patterns, corresponding to the crystal lattice in reciprocal space, are observed in selected area electron diffraction (SAED) mode, where an aperture can be used to isolate diffraction from a specific region. In polycrystalline specimens, this approach permits selection of a single grain, yielding discrete diffraction spots rather than the concentric rings typical of overlapping grains.

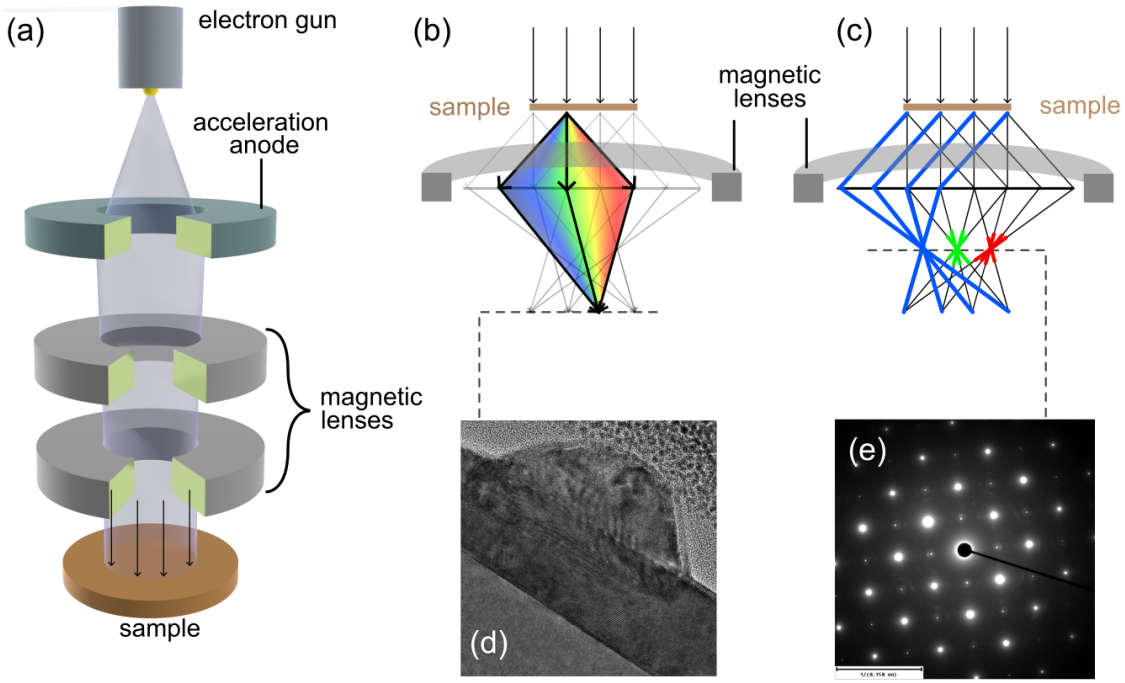


Figure 2.8: (a) Schematic illustration of TEM operation in conventional imaging mode with a parallel electron beam incident on the sample. Electrons are generated in the gun, accelerated towards the anode, and shaped by condenser lenses to achieve parallel illumination. (b) When following electrons transmitted from a single point in the sample, the objective lens refocuses the transmitted cone into the image plane, where contributions from each point overlap to form a real-space image. (c) When following electrons deflected by the same angle (colored differently), their trajectories converge in the back-focal plane, producing a diffraction pattern. Panels (d) and (e) show the resulting signals at the image plane and the SAED at the back-focal plane, respectively. The image in (d) is a cross-section of one of the initial films, which was uncapped and exhibited formation of likely Eu-O bubbles on the surface, though this was not investigated further, as applying a protective Ta layer consistently prevented such features. All depictions are highly schematic; details such as apertures, aberration corrections, and lens system complexities are omitted for clarity.

Beyond diffraction, the deflected electron waves propagate to form a real-space image that reflects variations in mass-thickness or composition, which can be magnified by the objective lenses. For high-resolution (HR) structural imaging, HR-TEM is employed. HR-TEM does not provide a direct image of atomic positions; rather, it converts phase shifts induced by the specimen into measurable intensity contrast. Thin specimens predominantly act as phase objects, shifting the phase of the transmitted electron wave without significantly affecting its amplitude. Lens aberrations and controlled defocus, typically considered detrimental, are exploited

to translate these phase shifts into image contrast, as described by a so-called contrast transfer function.

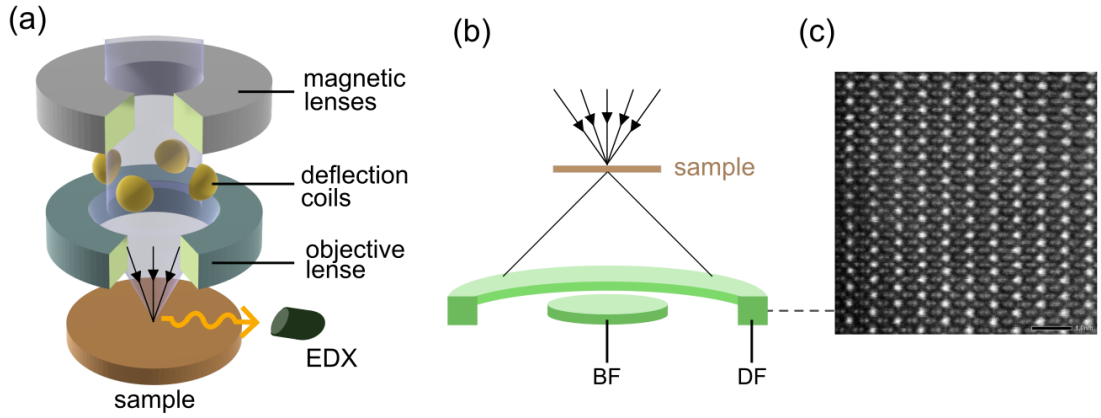


Figure 2.9: (a) Schematic of STEM operation: after the condenser system, deflection coils and the objective lens focus the beam to a nanoscale probe at the sample surface. The localized illumination allows spectroscopic techniques such as EDX to generate spatially resolved chemical maps. (b) Signal detection in STEM, with BF and HAADF detectors indicated schematically. The latter, used predominantly in this work, provides Z-contrast images due to its sensitivity to atomic number. (c) Example HAADF image obtained in STEM mode. All depictions are highly schematic; details such as apertures, aberration corrections, and lens system complexities are omitted for clarity.

In this thesis, the primary TEM mode utilized is scanning transmission electron microscopy (STEM), which provides high-resolution imaging and elemental mapping when combined with an EDX. In STEM, a finely focused electron probe is rastered across the sample, and the transmitted electrons are collected to form an image. A schematic of this setup is provided in Figure 2.9. STEM offers both bright-field (BF) and dark-field (DF) imaging modes. In BF-STEM, the detector collects electrons that pass through the sample with little or no scattering, producing contrast that is sensitive to variations in mass-thickness and crystal orientation. In DF-STEM, only scattered electrons are collected, which enhances contrast from heavier elements, as they scatter electrons more strongly. A high-angle annular dark-field (HAADF) detector, used in our system, collects electrons scattered to high angles, producing images with strong Z-contrast where heavier elements appear brighter. Coupled with EDX (see previous chapter 2.2.3), STEM also enables spatially resolved elemental maps, revealing the composition and distribution of elements at sub-nanometer

scales. Preparing cross-sectional TEM samples of films in this work involved focused ion beam (FIB) thinning. Overall, TEM provides direct microscopic evidence of epitaxy and structural quality. While not every sample was examined due to the labor-intensive preparation, representative films were analyzed to verify structural perfection and to correlate with XRD results.

2.3 Magnetic Characterization

2.3.1 Fundamentals of SQUID Magnetometry

Measurements of magnetic moment as a function of field or temperature in this work have been performed using a Quantum Design MPMS®3 [133]. The working principles of the superconducting quantum interference device (SQUID) magnetometer shall be outlined briefly. The following description largely follows Tinkham [68].

In the MPMS3, the sample is placed in a controlled environment where temperature and magnetic field can be precisely varied. To measure its magnetic moment, the sample is mechanically moved along the vertical axis through a set of pickup coils arranged in a gradiometer configuration. The motion of the sample induces a current in these coils, which is then routed through a secondary coil system that is magnetically coupled to the SQUID loop. In this way, the signal generated by the moving sample is effectively translated into a flux in the SQUID. The SQUID consists of a superconducting loop interrupted by two Josephson junctions. Each junction forms a weak link where the superconducting gap is maintained, allowing a supercurrent to flow without voltage. The physics of the junctions is governed by the Josephson relations in gauge-invariant form:

$$I = I_c \sin \phi, \tag{2.19}$$

$$\frac{d\phi}{dt} = \frac{2e}{\hbar} V, \tag{2.20}$$

where ϕ is the gauge-invariant phase difference of the complex Ginzburg-Landau (GL) order parameter on either side of the junction. As is standard, the complex GL order parameter in each electrode is written as $\Psi = |\psi| e^{-i\varphi}$, with φ denoting

the local phase. The phase difference ϕ therefore represents the difference of φ across the junction, including the contribution of the vector potential in the barrier region. When the bias current exceeds the SQUID's critical current, $I_{\text{bias}} > I_c$,

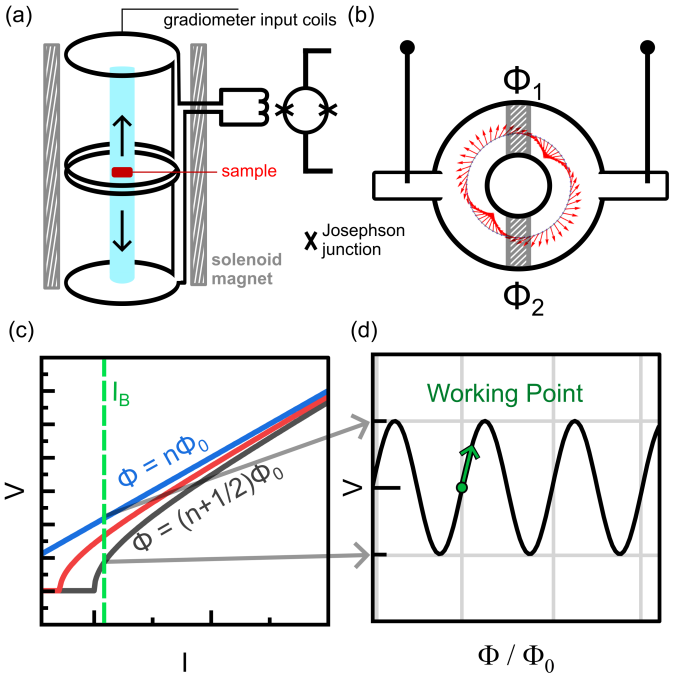


Figure 2.10: (a) Schematic representation of the SQUID magnetometer. The sample (red) is mounted in a transport tube and moved vertically through a second-order gradiometer coil, which cancels background fields, and couples the generated flux to the SQUID sensor (ring with two crosses marking the Josephson junctions). (b) Illustration of the SQUID loop with phases ϕ_1 and ϕ_2 across the two junctions; red arrows indicate one possible superconducting phase winding that enforces flux quantization. This concept, by a happy coincidence, will be revisited and explained a bit more in detail in the Little–Parks discussion in Chapter 3.5. (c) Example current–voltage characteristics obtained from Eq. 2.24. The blue and black curves correspond to flux values $\Phi/\Phi_0 = n$ and $n + 1$, giving the maximum and minimum voltages for a given bias I_{B}; the red curve illustrates an intermediate flux. (d) Voltage oscillations as a function of applied flux Φ. An FLL stabilizes the working point at maximum slope to achieve optimal sensitivity.

a finite voltage appears across the junctions. This situation is described by the resistively and capacitively shunted junction (RCSJ) model, which includes a junction resistance R for the dissipative current and a capacitance C, recasting the quantum problem to a classical one. Expressing the junction voltage in terms of the phase via the Josephson relation yields a second-order nonlinear differential equation for the phase, analogous to the motion of a classical pendulum. The full RCSJ model cannot be solved analytically; for a more complete discussion, the reader is

referred to Tinkham [68]. For the purpose of illustrating the basic principle, we can consider the overdamped limit ($C \to 0$), where the equation becomes analytically solvable, and the voltage–current relation reduces to

$$V = R\sqrt{I_{\text{bias}}^2 - I_c^2}. \tag{2.21}$$

For a symmetric DC SQUID with two identical junctions, the flux quantization condition relates the phase differences of the junctions, ϕ_1 and ϕ_2, to the total flux through the loop Φ:

$$\phi_1 - \phi_2 = 2\pi\frac{\Phi}{\Phi_0}. \tag{2.22}$$

The maximum supercurrent of the loop with two junctions is then

$$I_c(\Phi) = 2I_c\left|\cos\left(\pi\frac{\Phi}{\Phi_0}\right)\right|. \tag{2.23}$$

Inserting this flux-dependent critical current into the voltage relation gives

$$V(\Phi) = R\sqrt{I_{\text{bias}}^2 - \left[2I_c\left|\cos\left(\pi\frac{\Phi}{\Phi_0}\right)\right|\right]^2}. \tag{2.24}$$

This expression can be used to plot the current-voltage characteristic of the SQUID for different bias currents. For a fixed $I_{\text{bias}} > 2I_c$, the SQUID would develop a persistent finite voltage, which depends on the flux through the loop. As the flux is varied, the voltage oscillates between the values corresponding to $I_c(\Phi = n\Phi_0) = 0$ and $I_c(\Phi = (n+1/2)\Phi_0) = 2I_c$. The plot includes a horizontal line at the chosen I_{bias} to visualize the operating point and the resulting voltage oscillation. Finally, a flux-locked loop (FLL) is employed. The FLL maintains the SQUID at a fixed operating point on its voltage-flux curve by applying a compensating flux through a feedback coil. The current required in this feedback coil is linearly proportional to the external flux induced by the sample, allowing for a direct, unambiguous measurement of the magnetic moment, even when the total flux exceeds a single flux quantum. The FLL thereby avoids manual counting of flux quanta and linearizes the SQUID response. By biasing the SQUID at the point of maximum slope on its voltage-flux curve, the system achieves optimal sensitivity to even the smallest changes in magnetic flux.

2.3.2 X-ray Magnetic Circular Dichroism

XMCD is a spectroscopy method that exploits the coupling between the angular momentum of polarized X-ray photons and the magnetic degrees of freedom of a material. All following discussion follows the review of van der Laan and Figueroa [134]. The key physical principle of XMCD is that circularly polarized photons carry a quantized angular momentum projection of $\pm\hbar$ along their propagation axis. Through spin-orbit coupling, this photon angular momentum can be transferred to the electronic system, leading to different absorption probabilities for right- and left-handed light in a magnetized material. The resulting absorption difference, the dichroism, is directly linked to the spin and orbital magnetization of the sample.

To understand XMCD, it is helpful to begin with its "parent" technique, X-ray absorption spectroscopy (XAS). In XAS, X-ray photons of varying energy excite core electrons into unoccupied valence states. The absorption cross-section provides a fingerprint of the element and its electronic configuration.

Mathematically, the transition rate between an initial state ψ_i with energy E_i and a final state ψ_f with energy E_f under interaction with a photon of energy $\hbar\omega$ is given by Fermi's Golden Rule:

$$W_{i\to f} = \frac{2\pi}{\hbar} \left|\langle\psi_f|H'|\psi_i\rangle\right|^2 \delta(E_f - E_i - \hbar\omega), \tag{2.25}$$

where H' is the perturbation Hamiltonian describing the light-matter interaction. In minimal coupling,

$$H' = -\frac{e}{m}\,\mathbf{p}\cdot\mathbf{A}(\mathbf{r},t), \tag{2.26}$$

with $\mathbf{p}$ the electron momentum operator and $\mathbf{A}$ the vector potential of the incoming photon. For a plane wave, $\mathbf{A} \propto e^{i\mathbf{k}\cdot\mathbf{r}}$. Expanding the exponential in powers of (kr),

$$e^{i\mathbf{k}\cdot\mathbf{r}} \approx 1 + i(\mathbf{k}\cdot\mathbf{r}) + \ldots, \tag{2.27}$$

gives a multipole expansion. The leading term defines the *electric dipole approximation* ($Q = 1$), which dominates in the X-ray regime because $kr \ll 1$.

In spherical tensor language, the dipole operator leads directly to the well-known selection rules:

$$\Delta l = \pm 1, \qquad \Delta m = 0, \pm 1. \tag{2.28}$$

These rules explain the basic structure of conventional XAS spectra.

When going from XAS to XMCD, one must take into account that (i) the photon now carries angular momentum, and (ii) strong spin-orbit coupling couples orbital and spin degrees of freedom. This modifies the transition matrix elements and requires the use of total angular momentum quantum numbers J, M. Applying the Wigner–Eckart theorem to the transition operator, treated as a spherical tensor of arbitrary rank Q, leads to the generalized selection rules:

$$\Delta J = -Q, -Q+1, \ldots, Q, \qquad \Delta M = -Q, -Q+1, \ldots, Q. \tag{2.29}$$

In practice, the lowest-order case $Q = 1$ (electric dipole) dominates in the X-ray regime, but higher-order terms such as quadrupole ($Q = 2$) or octupole ($Q = 3$) can also contribute.

Finally, the observable in XMCD is the *difference spectrum*

$$\Delta\mu(\omega) = \mu^{+}(\omega) - \mu^{-}(\omega), \tag{2.30}$$

where μ^{+} and μ^{-} denote the absorption coefficients for right- and left-handed circularly polarized light, respectively. The celebrated XMCD sum rules show that integrals of $\Delta\mu$ over absorption edges are directly proportional to the expectation values of the orbital and spin magnetic moments of the absorbing atom. In practice, more elaborate models [134] (atomic multiplet theory, crystal-field splitting, Coulomb and exchange interactions, hybridization effects) must be included in the Hamiltonian and broadening effects of the experimental apparatus must be considered to reproduce detailed line shapes of the spectra. A comprehensive discussion of XMCD methodology lies beyond the scope of this thesis and is therefore omitted here.

A particularly useful aspect of XMCD is its element specificity. As the photon energy can be tuned to address the absorption edges of a chosen element independently. This allows the magnetic contributions of different elements within a compound to be disentangled. In the case of EFAP, this is of central importance: the Eu ions carry large localized $4f$ moments that are probed at the Eu $M_{4,5}$ edges, while the Fe sublattice contributes itinerant $3d$ magnetism that is addressed at the Fe $L_{2,3}$ edges. Since these absorption edges are well separated in energy, the XMCD spectra of Eu and Fe can be measured independently within the same sample, enabling a direct comparison of the localized and itinerant magnetic subsystems. Thus, XMCD complements SQUID by giving the distribution of magnetism among the constituents of EFAP.

2.4 Device Fabrication by Electron Beam Lithography

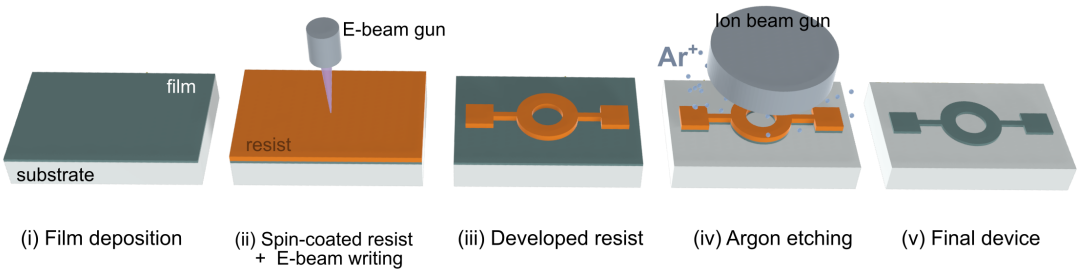


Figure 2.11: Illustration of the full EBL process for generating patterned structures, from resist coating to final device.

For this work, devices such as Hall bars and rings were fabricated using conventional electorn beam lithography (EBL) and ion-beam milling (IBM) techniques. The process begins with film growth on STO substrates by MBE, ensuring controlled thickness and high crystalline quality, as described in section 2.1. After deposition, a negative tone e-beam resist (ARN7520.18) layer with a thickness of 400 nm was applied by spin-coating. The resist was patterned by exposure to a high-precision electron beam using a JEOL JBX-8100FS system, operated at an acceleration voltage of 100 kV. This produced the desired resist mask pattern on top of the

film. To avoid possible degradation of the film integrity in wet environments, an argon IBM process was employed under partial pressure of 1.3×10^{-4} mbar. In this step, the exposed regions were etched away by Ar^+ ion sputtering, where ions are accelerated and bombard the film surface. The etching process was monitored a by end-point detector based on secondary-ion mass spectroscopy to prevent over etching into the STO substrate. Note that the over etching of STO can cause oxygen deficiencies, which can create conducting surfaces on etched areas. Finally, the remaining resist, including the protective layer on top of the structures, was removed with sequential gentle N-Methyl-2-pyrrolidone, acetone, and IPA treatment. A schematic illustration of the fabrication steps is shown in Figure 2.11.

3
Theoretical Toolkit

This chapter gathers all theoretical concepts, models, and formulas required to interpret the experimental data presented in the following chapters. As discussed previously, the system under investigation, EFAP, is a candidate ferromagnetic superconductor exhibiting multiband behavior. Consequently, this chapter begins with a theoretical framework suitable for describing such systems.

The first part addresses the temperature-dependent upper critical field, $H_{c2}(T)$, within a two-band approach as formulated by Gurevich for superconductors in the clean limit. To set the stage, a brief overview of the mixed state in type-II superconductors is provided within the Ginzburg–Landau (GL) formalism, serving as a reminder of the fundamental concepts. This is followed by an outline of the Werthamer–Helfand–Hohenberg (WHH) theory for $H_{c2}(T)$, which serves as a basis for introducing the more general two-band model developed by Gurevich.

The second section focuses on multi-carrier transport in non-superconducting materials, which is essential for analyzing the normal-state transport properties.

Subsequently, the Bean critical state model is introduced to describe magnetic flux penetration in type-II superconductors and to provide the theoretical basis for understanding hysteretic magnetization loops. This framework also enables the determination of critical current densities, J_c, which are then used in the analysis of vortex pinning mechanisms. The following section explores the collective

vortex pinning model, emphasizing the characteristic temperature dependence of $J_c(T)$ in different pinning regimes.

Finally, the chapter concludes with a discussion of the Little–Parks (LP) effect, including the relevant theoretical background and mathematical relations necessary for interpreting the associated experimental observations.

Contents

3.1 Gurevich Two-Band Model 46
3.2 Multi-carrier Transport 50
3.3 Bean Critical State Model 51
3.4 Collective Vortex Pinning Model 52
3.5 Little-Parks Effect 53

3.1 Gurevich Two-Band Model

As the discussion of the two-band superconductivity model will be grounded within the fundamentals of the mixed state in type-II superconductors, we should begin by recalling some basics of superconductivity [68]. The upper critical field H_{c2}, which marks the boundary above which the superconducting vortex state is completely destroyed, can be described phenomenologically by the GL theory. It provides a direct link between this macroscopic critical field and the microscopic coherence length, ξ, which sets the characteristic scale for variations in the superconducting order parameter. For an anisotropic material, the zero-temperature coherence lengths in the principal directions are given by the linearized GL relations:

$$\xi_{ab} = \sqrt{\frac{\Phi_0}{2\pi H_{c2}^{c}(0)}}, \quad \text{and} \quad \xi_c = \frac{\Phi_0}{2\pi \xi_{ab} H_{c2}^{ab}(0)}, \tag{3.1}$$

where Φ_0 is the magnetic flux quantum. Although this thesis concerns thin films, the small intrinsic ξ in FeSCs justifies the use of this 3D formalism, as it will always be smaller than the film thicknesses. GL theory can also be derived from the microscopic Bardeen–Cooper–Schrieffer (BCS) formalism via the Gor'kov Green's function approach, providing a correspondence between phenomenological quantities and microscopic parameters. Exploiting this formalism, Werthamer, Helfand, and

Hohenberg (WHH) derived a full temperature-dependent description of $H_{c2}(T)$ in the dirty limit, where the electronic mean free path ℓ is much smaller than the superconducting coherence length ξ. This is mostly referred to as as the WHH model [135]. Including spin paramagnetism and spin–orbit scattering, the WHH model reads:

$$\begin{aligned}\ln\frac{1}{t} = &\left(\frac{1}{2}+i\frac{\lambda_{\mathrm{SO}}}{4\Gamma}\right)\psi\left[\frac{1}{2}+\frac{h^*+\lambda_{\mathrm{SO}}/2+i\Gamma}{2t}\right]\\ &+\left(\frac{1}{2}-i\frac{\lambda_{\mathrm{SO}}}{4\Gamma}\right)\psi\left[\frac{1}{2}+\frac{h^*+\lambda_{\mathrm{SO}}/2-i\Gamma}{2t}\right]-\psi\left(\frac{1}{2}\right),\end{aligned} \tag{3.2}$$

with

$$t=\frac{T}{T_{\mathrm{c}}},\quad h^*=\frac{4H_{\mathrm{c2}}}{\pi^2\left(\frac{dH_{\mathrm{c2}}}{dT}\right)\Big|_{T_{\mathrm{c}}}},\quad \Gamma=\sqrt{(\alpha_{\mathrm{M}}h^*)^2-(\lambda_{\mathrm{SO}}/2)^2}. \tag{3.3}$$

Here, ψ is the digamma function, α_{M} is the Maki parameter, quantifying the impact of Pauli paramagnetism on the upper critical field relative to orbital effects, while λ_{SO} accounts for spin–orbit scattering. As WHH noted, spin–orbit scattering counteracts Pauli pair breaking by mixing spin states, thereby allowing the superconductor to withstand a stronger magnetic field before being suppressed. A visualization will be provided later, together with a comparison to two-band results, which are explained next. The WHH model is widely used to identify critical field curves, but deviations from its predictions, as prominently seen in MgB_2, indicate unconventional behavior arising from its two-band nature: a quasi-two-dimensional σ bands and three-dimensional π bands, with distinct Fermi velocities and superconducting gaps, lead to $H_{c2}(0)$ being higher than expected [136]. Motivated by this, Gurevich developed a multi-band model based on a weak-coupling BCS approach in the dirty limit [137], which he later extended to the clean limit using Eliashberg theory [138]. The clean limit Gurevich model yields the following implicit equation for the critical field, reflecting the coupled nature of the two condensates:

$$a_1\Big[\ln(t)+U_1\Big]+a_2\Big[\ln(t)+U_2\Big]+\Big[\ln(t)+U_1\Big]\Big[\ln(t)+U_2\Big]=0. \tag{3.4}$$

The coefficients a_1, a_2 and w are combinations of the dimensionless intra- and interband coupling constants ($\lambda_{11}, \lambda_{22}, \lambda_{12} = \lambda_{21}$):

$$\begin{aligned} a_1 &= \frac{\lambda_0 + \lambda_-}{2w}, \qquad & a_2 &= \frac{\lambda_0 - \lambda_-}{2w}, \\ \lambda_- &= \lambda_{11} - \lambda_{22}, \qquad & \lambda_0 &= \sqrt{(\lambda_{11} - \lambda_{22})^2 + 4\lambda_{12}^2}, \\ w &= \lambda_{11}\lambda_{22} - \lambda_{12}^2. \end{aligned} \tag{3.5}$$

The functions $U_1 = U(t, h, \alpha, 1, 1)$ and $U_2 = U(t, h, \alpha, \nu, s)$ are given by

$$\begin{aligned} &U(t, h, \alpha, \nu, s) = \\ &\quad 2^{q^2 s}\mathrm{Re}\sum_{n=0}^{\infty}\int_{q\sqrt{s}}^{\infty} e^{-u^2}\left[\frac{u}{n+1/2} - \frac{t}{\sqrt{h\eta}}\arctan\left(\frac{u\sqrt{h\eta}}{t(n+1/2) + i\alpha h}\right)\right] du. \end{aligned} \tag{3.6}$$

with

$$\begin{aligned} h &= \frac{\hbar^2 v^2 H}{8\pi\phi_0 k_B^2 T_\mathrm{c}^2}, \quad & \alpha &= \frac{4\mu\phi_0 k_B T_\mathrm{c}}{\hbar^2 v_1^2}, \\ q^2 &= \frac{Q_z^2 \phi_0 \epsilon_1}{2\pi H}, \qquad & \eta &= \frac{v_2^2}{v_1^2}, \\ s &= \frac{\epsilon_2}{\epsilon_1}. \end{aligned} \tag{3.7}$$

Here, t is the reduced temperature T/T_c, H is the external field, v_i are Fermi velocities of band i and α is related to the Maki parameter by a numerical prefactor. The Fermi surfaces are specified to be of prolate ellipsoidal form with isotropic in-plane effective mass (m) and larger out-of-plane effective mass (m_c). With this, ϵ_i are defined as the mass anisotropies (m/m_c) for each band i. Q_z is the magnitude of the Fulde-Ferrell-Larkin-Ovchinnikov modulation, which only becomes relevant for fields well above the range applied in this work. Hence the contribution can be neglected and we set $Q_z = 0$.

Figure 3.1 compares four calculated $H_{c2}(T)$ curves. The first two correspond to the WHH model with $\alpha_\mathrm{M} = 2$ and spin–orbit scattering parameters $\lambda_\mathrm{SO} = 0$ and $\lambda_\mathrm{SO} = 1$, respectively, illustrating the aforementioned behavior that spin–orbit scattering counteracts Pauli pair breaking: higher λ_SO leads to an increased $H_{c2}(0)$. The other two curves represent solutions of the Gurevich two-band model for the clean limit. In one case, $\alpha = 0.05$, $\eta = 0.01$, $s = 1$, $\lambda_{11} = \lambda_{22} = 0$, and $\lambda_{12} = \lambda_{21} = 0.5$, corresponding to negligible intraband or dominant interband

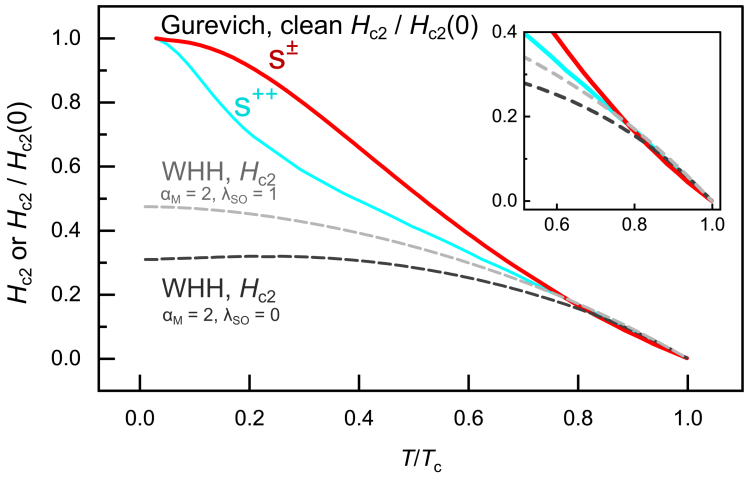


Figure 3.1: Comparison of calculated upper critical field curves within the WHH and Gurevich models. The WHH results (gray dashed lines) are shown for $\alpha_{\mathrm{M}} = 2$ with spin–orbit scattering parameters $\lambda_{\mathrm{SO}} = 0$ and $\lambda_{\mathrm{SO}} = 1$, demonstrating that stronger spin–orbit coupling increases $H_{c2}(0)$. The Gurevich two-band results (solid colored lines) correspond to parameter sets representing predominantly interband ($s^{\pm}$) and intraband (s^{++}) coupling, with exact parameter values provided elsewhere in this section. For the WHH curves, absolute H_{c2} values are plotted, while the Gurevich curves are normalized to $H_{c2}(0)$ to emphasize the shape of the temperature dependence. The inset highlights the upward curvature that may appear within the Gurevich model near T_{c}. It is particularly evident for the $s^{\pm}$ (red) curve.

pairing ($\lambda_{11}\lambda_{22} \ll \lambda_{12}\lambda_{21}$). One possible realization of this regime can be produced by $s^{\pm}$-type order parameters with opposite signs on the two bands. The second case uses $\lambda_{11} = 0.8$, $\lambda_{22} = 0.3$, and $\lambda_{12} = \lambda_{21} = 0.1$, representing stronger intraband coupling ($\lambda_{11}\lambda_{22} \gg \lambda_{12}\lambda_{21}$), as might occur in an s^{++} superconductor. Gurevich discusses these coupling regimes and their consequences in more detail [138]. For the WHH curves, $\frac{dH_{c2}}{dT}\Big|_{T_c}$ was set to unity, and the absolute H_{c2} values are shown to emphasize the increase of $H_{c2}(0)$ with spin–orbit scattering. In contrast, the Gurevich model results are plotted as normalized $H_{c2}/H_{c2}(0)$, which highlights the distinct curvature of $H_{c2}(T)$ arising from multiband effects. The most important qualitative difference for this work is that the Gurevich model can yield an upward curvature of $H_{c2}(T)$ at around T_c, as further illustrated in the inset of Figure 3.1.

3.2 Multi-carrier Transport

The two-band description of superconductivity discussed in the previous chapter highlights the role of multiple electronic bands. Above T_c, these same bands contribute to normal-state transport, necessitating a multi-band treatment of the resistivity and Hall effect. The behavior of charge carriers in metals can be described by Drude's model, which treats electrons as classical particles undergoing scattering in a uniform background potential, according to kinetic gas theory [139]. This classical model treats a single type of carrier with charge q, density n, effective mass m^*, and relaxation time τ. When assuming isotropic Fermi surfaces and solving the equation of motion in magnetic fields, yields a conductivity tensor whose inversion gives a field independent longitudinal resistivity $\rho_{xx} = \rho_0$ and a linear Hall resistivity $\rho_{xy} \propto H$. Extensions to multiple carrier types, each with its own density, charge, and mobility, are obtained by summing the individual conductivity tensors and inverting the result. In such *two- or multi-band models*, the longitudinal resistivity acquires a field dependence that is generally nonlinear, which at low fields may start quadratically but can include higher-order terms at larger fields, explaining the magnetoresistance observed in real materials. As will be demonstrated in section 5.3, a three-carrier model can describe the reported EFAP films accurately. The corresponding expression for the resistivity can be calculated as [140]

$$\rho_{xy}(H) = (\rho_0 H)\,\frac{a + b\,H^2 + c\,H^4}{1 + dH^2 + e_{\text{coeff}}\,H^4} \tag{3.8}$$

$$\rho_{xx}(H) = \rho_0\,\frac{1 + \alpha\,H^2 + \beta\,H^4}{1 + d\,H^2 + e_{\text{coeff}}\,H^4} \tag{3.9}$$

$$
\begin{aligned}
\rho_0 &= \frac{1}{e\left(|n_1\mu_1| + |n_2\mu_2| + |n_3\mu_3|\right)}, \quad e = 1.602 \times 10^{-19}\ \mathrm{C},\\
f_1 &= \frac{|n_1\mu_1|}{|n_1\mu_1| + |n_2\mu_2| + |n_3\mu_3|}, \quad f_2 = \frac{|n_2\mu_2|}{|n_1\mu_1| + |n_2\mu_2| + |n_3\mu_3|},\\
f_3 &= \frac{|n_3\mu_3|}{|n_1\mu_1| + |n_2\mu_2| + |n_3\mu_3|},\\
a &= f_1\mu_1 + f_2\mu_2 + f_3\mu_3,\\
b &= f_1\mu_1(\mu_2^2 + \mu_3^2) + f_2\mu_2(\mu_3^2 + \mu_1^2) + f_3\mu_3(\mu_1^2 + \mu_2^2),\\
c &= \left(f_1\mu_2\mu_3 + f_2\mu_3\mu_1 + f_3\mu_1\mu_2\right)\mu_1\mu_2\mu_3,\\
d &= \left(f_1\mu_2 + f_2\mu_1\right)^2 + \left(f_2\mu_3 + f_3\mu_2\right)^2 + \left(f_3\mu_1 + f_1\mu_3\right)^2\\
&\quad + 2\left(f_1f_2\mu_3^2 + f_2f_3\mu_1^2 + f_3f_1\mu_2^2\right)^2,\\
e_{\mathrm{coeff}} &= \left(f_1\mu_2\mu_3 + f_2\mu_3\mu_1 + f_3\mu_1\mu_2\right)^2,\\
\alpha &= \left(f_1 + f_2\right)\mu_3^2 + \left(f_2 + f_3\right)\mu_1^2 + \left(f_1 + f_3\right)\mu_2^2,\\
\beta &= f_1\,\mu_2^2\mu_3^2 + f_2\,\mu_1^2\mu_3^2 + f_3\,\mu_1^2\mu_2^2
\end{aligned}
\tag{3.10}
$$

with n_i (μ_i) being the charge carrier densities (carrier mobilities) of band i.

3.3 Bean Critical State Model

The Bean critical state model provides a phenomenological description of the current distribution in a hard type-II superconductor [141]. It assumes a critical state in which vortices are fully pinned and, wherever magnetic flux penetrates, a critical current flows. Accordingly, the current density is either zero, within the central region where no field has penetrated, or equal to $\pm J_c$ elsewhere.

In a zero-field-cooled (ZFC) sample, when the external field is increased, magnetic flux penetrates progressively toward the specimen center until, at a certain field strength, it reaches the core. Upon subsequently reducing the field, counterflowing screening currents retain trapped flux until the situation eventually reverses. This simplified picture explains why hard type-II superconductors exhibit hysteretic magnetic behavior.

Using Maxwell's equations, and specifically the Biot-Savart law, the critical current can be related to the external magnetic field through a cross product. From this, one can derive an expression linking the width of the magnetization hysteresis loop (ΔM) to the critical current. The formulation presented by Gyorgy *et al.* for a rectangular sample with in-plane dimensions $a \leq b$ and the field applied to the surface normal is widely used [142]:

$$J_{\mathrm{c}} = \frac{20\,\Delta M}{a\left(1 - \frac{a}{3b}\right)} \quad . \tag{3.11}$$

In this expression, the pre-factor of 20 is not dimensionless; it requires that ΔM be expressed in units of emu/cm^3 to yield J_{c} in A/cm^2.

3.4 Collective Vortex Pinning Model

In type-II superconductors, two principal pinning mechanisms are distinguished: δT_{c} pinning, originating from spatial inhomogeneities of the local superconducting critical temperature, and $\delta\ell$ pinning, arising from weak, randomly distributed point-like defects that cause local variations in the mean free path [143, 144]. Blatter *et al.* [143] showed how such pinning mechanisms can be connected to microscopic quantities, including the critical current density J_{c}. Experimental evidence for mean free path fluctuation-induced pinning and explicit expressions for $J_{\mathrm{c}}(t)$ for both types of pinning were given by Griessen *et al.* [144]. In a 3D single-vortex collective pinning framework, these yield the following analytic forms:

$$\frac{J_{\mathrm{c}}(t)}{J_{\mathrm{c}}(0)} \;=\; (1-t^2)^{5/2}\,(1+t^2)^{-1/2}, \tag{3.12}$$

for $\delta\ell$ pinning. While δT_{c} pinning follows

$$\frac{J_{\mathrm{c}}(t)}{J_{\mathrm{c}}(0)} \;=\; (1-t^2)^{7/6}\,(1+t)^{5/6}. \tag{3.13}$$

Hence, equipped with J_{c} from the Bean model, as calculated using equation (3.11), these expressions can be employed to probe the pinning structures by exploiting the difference in collective vortex motion.

3.5 Little-Parks Effect

In the GL theory, minimization of the free energy gives rise to the GL equations, which also describe the Cooper pair current [68]. The supercurrent density is given by

$$\mathbf{j}_s = \frac{2e\hbar}{m}|\psi|^2\left(\nabla\varphi - \frac{2e}{\hbar}\mathbf{A}\right), \tag{3.14}$$

where $\Psi = |\psi|e^{i\varphi}$ is the complex superconducting order parameter with phase φ, $\mathbf{A}$ is the magnetic vector potential, e the elementary charge, $\hbar$ the reduced Planck constant, and m the effective mass of a Cooper pair. Integrating around a closed path one obtains

$$\oint \mathbf{j}_s \cdot d\mathbf{r} = \frac{2e\hbar}{m}|\psi|^2\left(\oint \nabla\varphi \cdot d\mathbf{r} - \frac{2e}{\hbar}\oint \mathbf{A}\cdot d\mathbf{r}\right). \tag{3.15}$$

The wavefunction should be single-valued, $\oint \nabla\varphi \cdot d\mathbf{r} = 2\pi n$, while the vector potential term can be converted by Stokes' theorem into a general expression for the magnetic flux, $\oint \mathbf{A}\cdot d\mathbf{r} = \int \mathbf{B}\cdot d\mathbf{S} = \Phi$. If the integration contour lies deep within the bulk of the superconductor, where $\mathbf{j}_s = 0$, one obtains the flux quantization condition $\Phi = n\Phi_0$, with $\Phi_0 = h/2e$ the magnetic flux quantum. More generally, when such a current-free contour is not available, it is the fluxoid that remains quantized, defined as [145, 146]

$$\Phi_{\text{fluxoid}} = \Phi + \mu_0\lambda^2\oint \mathbf{j}_s \cdot d\mathbf{r} = n\Phi_0, \tag{3.16}$$

where μ_0 is the vacuum permeability and λ is the London penetration depth. Without going into mathematical details, one possible line of reasoning commonly used to illustrate how this quantization can be observed experimentally is outlined below. Choosing a circle of fixed radius fixes the supercurrent velocity v_s to obey fluxoid quantization. As the external magnetic flux Φ is increased, v_s adjusts linearly to maintain the quantization for a given integer state n. Through GL theory, the supercurrent velocity is related to T_c quadratically. A schematic representation of how v_s and the suppression in superconducting critical temperature ΔT_c will periodically vary with Φ is shown in Figure 3.2. This picture also clarifies how the winding number n is chosen: the system attempts to keep T_c as high as

possible, so n is selected to minimize ΔT_c, which simultaneously keeps v_s minimal. Whenever Φ reaches a full quantum Φ_0, n can change by one. Another way to

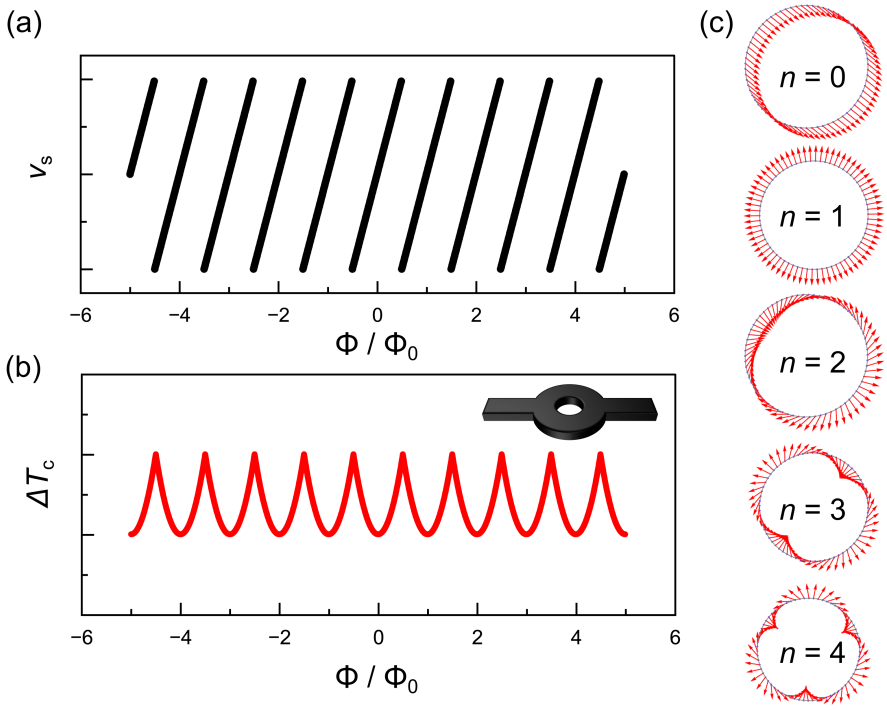


Figure 3.2: (a) Quantization of the supercurrent velocity as a function of external magnetic field. (b) Corresponding variation of the critical temperature shift, ΔT_c, with external field. (c) Flat schematic of the GL phase around a superconducting ring. Each arrow indicates the local phase of the order parameter, represented by its angle relative to the ring tangent. Single-valuedness requires the phase to return to its starting value after one complete circuit. Representative winding numbers $n = 0$–4 are shown.

think about this is that when the external field reaches Φ_0, the complex GL order parameter $\Psi = |\psi|\, e^{-i\varphi}$ can incorporate this change into its phase to compensate for changes in the vector potential. Adjusting the phase is an effective way for the system to respond, allowing it to compensate the external field by an additional Φ_0. For intermediate flux values that are fractions of Φ_0, the system cannot fully incorporate them into the phase. Instead, the free energy is reduced by affecting other quantities, which in turn influence v_s and T_c. Experimentally, a fixed closed path can be realized by fabricating a thin-walled ring. This was first demonstrated by Little and Parks [146], and the resulting oscillatory effect is known as the Little–Parks (LP) effect. Tinkham [68] and Moshchalkov *et al.* [147] reported

concise formulas for ΔT_c in annular rings. For this work, square rings were chosen, because they can be fabricated more easily using EBL. A formula for this geometry can be derived following the same method as for an annular ring, leading to the following expression for a superconducting square ring, approximated by averaging the one-dimensional result over the different radii imposed by the finite linewidth w with side length L and effective centerline area L^2:

$$\frac{\Delta T_c(H)}{T_c(H=0)} = -\left(\frac{\pi\,\xi(0)\,w\,H}{\sqrt{3}\,\Phi_0}\right)^2 - \left(\frac{\pi\,\xi^2(0)}{2L}\right)^2 \left(n - \frac{HL^2}{\Phi_0}\right)^2 . \tag{3.17}$$

From this formula, the expected oscillation period becomes $\Delta H = \Phi_0/L^2$, and the amplitude is $\Delta T_c^{\mathrm{amp}}(H) = T_c(0)\,(\pi\,\xi_0/4L)^2$. In realistic experimental scenarios, ΔT_c is often not directly accessible. However, the effect of the oscillating T_c propagates into the resistivity [146, 148] by

$$\Delta R = \Delta T_c \left(\frac{\partial R(H=0)}{\partial T}\right)\Big|_{T=T_c} . \tag{3.18}$$

This expression shows that the amplitude of the resistance oscillations is proportional to both the LP-induced modulation of T_c and the slope of the resistive transition at zero field.

In type-II superconducting rings with wall thicknesses exceeding the coherence length, vortices can nucleate within the walls. As FeSCs have very short coherence lengths, this scenario is likely even when careful zero-field cooling and slow current sweeps are applied. Following the same arguments as above, these vortices are also quantized. Their appearance may locally change the phase winding number n, but the periodicity of the LP oscillations remains unaffected [149]. In principle, the number of vortices can increase with each integer multiple of Φ_0 as the external field grows, and decrease on backward sweeps. Also a mixture of vortex-assisted and conventional LP behavior is conceivable. As the fluxoid quantization remains unchanged, the oscillation period will be the same. However, trapped vortices introduce additional quantized flux inside the ring. Consequently, the LP oscillations may appear phase-shifted along the external field axis. Additionally, vortex-assisted oscillations can exhibit amplitudes larger than expected for the pure LP effect [150].

It has been predicted that spin-triplet SCs with gaps of the p+ip form may host half-flux vortices [151]. Building on that, the effects on oscillations in triplet superconductors even with vortices in the ring wall have been theoretically studied by Halász in [152], who predicted a possible splitting of each magnetoresistance peak with the peaks moving apart with decreasing ratio of the spin and charge superfluid density γ. Oscillations become more complex and periodicities can be temperature dependent. Another effect, which can be understood intuitively when considering $\Phi_{\text{fluxoid}} = (n + 1/2)\Phi_0$, is the possibility of a spontaneous half magnetic flux quantum even at zero-field. This has been reported for rings of 4Hb-TaS_2 [153] and β-Bi_2Pd [154]. Interpretation of deviations from conventional LP effects still remain difficult, as half-quantum vortices can also appear due to other reasons. To name some, they have been predicted in heavy-fermion SCs [155], polycrystalline samples with rotated grains in a specific orientation such that odd numbers of Josepshon couplings between grains show half-quantized vortices [153], or in cases where a two-component order parameter is present together with a specific strain orientation across the ring [156]. Especially when looking at LP oscillations, trapped fluxes need to be ruled out.

4

Molecular Beam Epitaxy of $EuFe_2(As_{1-x}P_x)_2$

This chapter details the MBE growth and basic characterization of EFA and its P-substituted variant EFAP. These crystallize in the $ThCr_2Si_2$-type structure (tetragonal, space group *I4/mmm*). The in-plane lattice constant of EFA is $a \approx 3.906, \text{Å}$, which increases slightly upon P substitution due to the concomitant shrinkage of the *c*-axis. Both are grown on STO(1 0 0) substrates. STO has a cubic perovskite structure (space group $Pm\bar{3}m$) with a room-temperature lattice constant $a_{\text{STO}} \approx 3.905\,\text{Å}$. The lattice mismatch f is estimated as

$$f_{\text{STO}} \approx \frac{(3.906 - 3.905)}{3.905} \times 100\% \approx 0.03\%.$$

For comparison, $LaAlO_3$ (LAO) has a pseudo-cubic lattice constant of $a_{\text{LAO}} \approx 3.79\,\text{Å}$, corresponding to a mismatch of

$$f_{\text{LAO}} \approx \frac{(3.906 - 3.79)}{3.79} \times 100\% \approx +3.1\%.$$

Similarly, $(LaAlO_3)_{0.3}(Sr_2TaAlO_6)_{0.7}$ (LSAT) has $a_{\text{LSAT}} \approx 3.868\,\text{Å}$, giving

$$f_{\text{LSAT}} \approx \frac{(3.906 - 3.868)}{3.868} \times 100\% \approx +1.0\%.$$

Despite the larger mismatch, successful growth of EFA and EFAP films was also achieved on LAO and LSAT substrates. Of particular note is the more successful

growth of high-P EFAP films on LSAT substrates compared to STO, consistent with the reduced in-plane lattice parameter at full P substitution ($x = 1$, $a \approx 3.82, \text{Å}$) [74]. For this thesis, the primary focus is on films grown on STO, where in total more than 500 films were grown (including many failed trials during optimization). Unless otherwise stated, all results discussed in the following sections refer to films grown on STO; whenever other substrates are used, this will be explicitly mentioned.

In the following, epitaxial growth of the parent compound EFA is established first. This includes identification of suitable growth conditions and the accessible growth window, as well as in-situ monitoring by RHEED and room-temperature STM during the initial stages of growth. The resulting films are then analyzed by XRD and TEM[1] to confirm their structural quality. This provides the basis for subsequent P substitution.

Building on these results, growth of EFAP is presented next, which is stabilized using an ultrathin EFA buffer layer. As the main focus of this work, EFAP is examined in more detail: growth conditions and dynamics are discussed, and in-situ RHEED observations are complemented by structural analysis (XRD, TEM) and atomic-resolution compositional mapping (EDX). The latter directly confirms P incorporation on the As sublattice, with indications of a modulated substitution pattern.

Contents

4.1 $EuFe_2As_2$: Laying the Groundwork for Substitution . 58
4.2 Extending Growth to the P-Substituted System 63

4.1 $EuFe_2As_2$: Laying the Groundwork for Substitution

The epitaxial growth of EFA thin films requires a balance between flux ratios, substrate temperature and growth rate. An important initial condition is establishing

[1] FIB preparation was performed by Norbert Schrammelt and Hakan Deniz, and TEM/STEM measurements by Hakan Deniz, whose support is gratefully acknowledged.

flux ratios that yield near-stoichiometric films, which represents the first step toward achieving stable epitaxy. RBS[2] shows that when the Eu:Fe:As ratio deviates strongly from the nominal 1:2:2, the films turn amorphous or polycrystalline. As an example, the RHEED result of an Eu-rich composition ($Eu_{1.5}Fe_2As_2$) with no long-range crystal order is shown in Figure 4.1(a). In such cases, RHEED patterns lack streaks or spots altogether and rings appear. Once the fluxes are tuned closer to stoichiometric balance, crystalline growth emerges and the RHEED images begin to show 3D spots characteristic of island nucleation, sometimes together with streaks, as shown in Figure 4.1(b). At this stage, the correct phase has formed but epitaxy is incomplete. The transition to epitaxial, layer-by-layer growth is then accomplished by fine-tuning the substrate temperature, as evidenced by the appearance of sharp RHEED streaks, as shown in Figure 4.1(c). In addition to the primary streaks, weaker features appear at fractional positions (1/3, 2/3), indicative of a surface reconstruction. Azimuthal RHEED scans further confirm a fourfold in-plane symmetry, consistent with epitaxial alignment on the STO substrate.

The precise nature of the reconstruction is difficult to determine without complementary high-resolution surface probes such as in-situ STM with atomic resolution, but its presence underscores the high surface quality achieved under optimized growth conditions. In fact, a few high-resolution low-temperature STM measurements were undertaken and are summarized in the additional materials (Chapter B). But these were primarily aimed at probing superconducting gaps in ultrathin films, as will be discussed further in the next chapter.

Over the course of three years of trials, we found that substrate temperatures ranging from roughly 380 °C to 520 °C can, at different times, yield high-quality EFA films in our MBE system. The chamber conditions, such as base pressure and residual contaminants, inevitably evolve between experimental runs, especially after each chamber opening. Consequently, while 380 °C to 520 °C is the broad overall window observed, there appears to be a narrow "optimal"temperature at any given point in time. Deviations of just a few degrees above or below this

[2]RBS measurement and analysis performed by Ilya Kostanovski and Herbert Engelhard, whose support is gratefully acknowledged.

short-term optimum can lead to substantial changes in film morphology. This sensitivity is best seen when comparing two back-to-back films grown under otherwise identical conditions. In this specific example presented in Figures 4.1(b) and (c), at 462 °C, RHEED revealed a mixed pattern indicative of both epitaxial and island-type growth modes, whereas lowering the substrate temperature to 457 °C yielded purely epitaxial films with sharp streaks and the aforementioned fractional streaks. Returning to 462 °C once again pushed the system toward 3D islands. This trend was consistently observed across multiple runs: a small reduction in temperature invariably reduced or eliminated 3D islands in subsequent growth. This underscores both the delicate temperature sensitivity of EFA and the necessity of fine-tuning growth conditions as the chamber environment varies over time. Another reason for the wide usable temperature range is the interplay between substrate temperature and growth rate. In analogy to the critical conditions separating step-flow growth from random nucleation (see Chapter 2.1), the apparent boundary between smooth epitaxial growth and island growth shifts with growth rate, so that different substrate temperatures may be optimal depending on the deposition rate. While such a systematic dependence cannot be established here, since after the successful stabilization of EFA the focus of the project shifted to EFAP films, this point will be revisited in the following chapter, where the combined dataset of EFA and EFAP samples allows us to examine this scaling more directly. Typical BEP rates, as measured by RGA, were $\sim 5 \times 10^{-13}$ Torr for Eu, $\sim 6 \times 10^{-13}$ Torr for Fe, and $\sim 1 - 5 \times 10^{-12}$ Torr for As, with the As flux predominantly supplied as As_2. A Eu:Fe:As BEP ratio of 1:1:2 allows reliable production of crystalline films with good stoichiometry, which was confirmed by RBS. The nominal 1:1:2 flux ratio does not directly reflect the $Eu_1Fe_2As_2$ stoichiometry, likely because Fe exhibits a much higher sticking coefficient than Eu. A moderate As surplus (up to about five times the baseline flux) further improves growth, most likely by compensating for As desorption at elevated substrate temperatures, helping to maintain the correct 122 structure and stoichiometry. When the As content is increased beyond this range, the films exhibit degraded crystallinity and deviate from stoichiometry. Capping

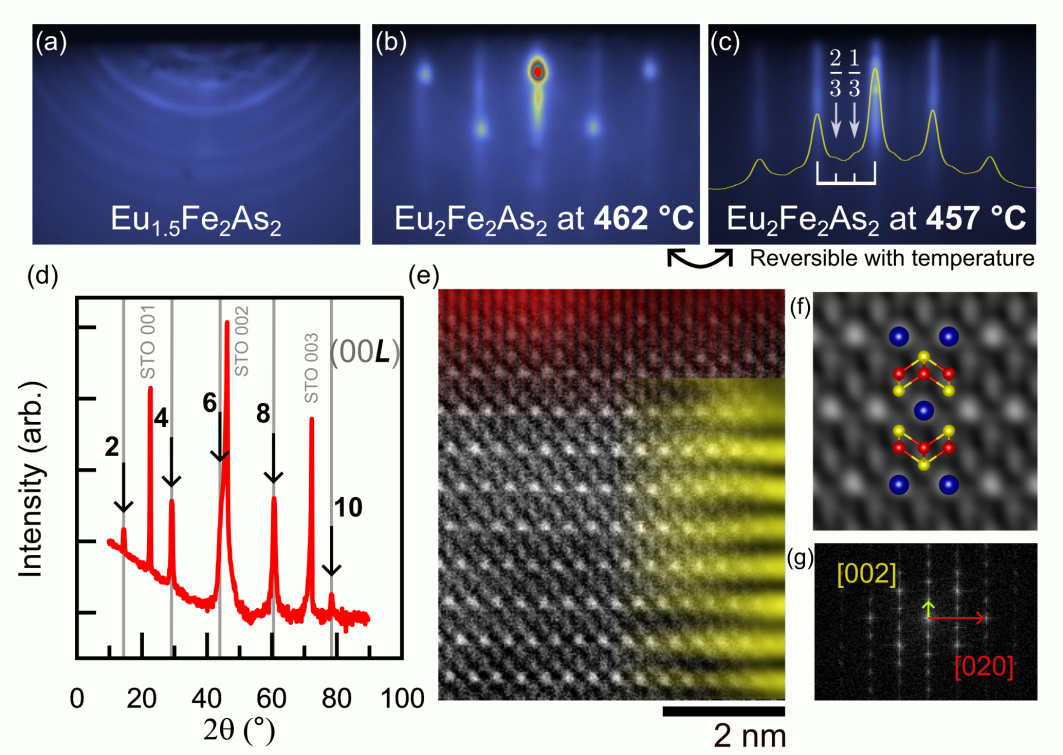


Figure 4.1: (a) Ring-type RHEED patterns characteristic of films grown far from stoichiometry, exemplified here by a Eu-rich sample. (b) Mixed dots and streaks, indicative of coexisting island and 2D growth, observed under near-stoichiometric conditions but with non-optimal substrate temperature. (c) Well-defined RHEED streaks with (1/3, 2/3) fractional streaks under optimal growth conditions. The fractional streaks are more clearly visible in the integrated line profile, shown as a yellow line. (d) Representative XRD θ–2θ scan showing (0 0 l) reflections at ∼14.5° (0 0 2), 29.4° (0 0 4), 44.7° (0 0 6), 61.0° (0 0 8), and 78.7° (0 0 10), corresponding to $c \approx 12.1$, Å. (e) HAADF-STEM cross-section demonstrating good crystallinity. (f) Zoomed-in, Gaussian-filtered view with the atomic crystal model overlaid. (g) FFT of the full HAADF-STEM image with identification of the [0 0 2] and [0 2 0] q-vectors. The corresponding inverse FFT components are overlaid in (e) in red and yellow, respectively.

films with As was attempted, but did not provide sufficient protection, as the physical properties degraded over the course of several months. In contrast, roughly 2 nm Ta capping preserved the samples, with films remaining stable as evidenced by unchanged resistivity and magnetization measurements even after more than a year. Ex-situ structural characterization corroborates the in-situ observations. Out-of-plane X-ray diffraction (θ–2θ) scans show clear EFA (0 0 l) reflections at ∼14.5° (0 0 2), 29.4° (0 0 4), 44.7° (0 0 6), 61.0° (0 0 8), and 78.7° (0 0 10), consistent with a c-axis lattice parameter of about 12.1 Å, in agreement with bulk values [16].

As expected for the body-centered tetragonal $I4/mmm$ structure, reflections with odd l are systematically absent. STO substrate peaks appear at ∼22.8°, 46.5°, and 72.6°. Cross-sectional TEM images confirm the expected crystal structure. A cropped region of the image is shown in Figure 4.1(e), while panel (f) presents a magnified and smoothed by Gaussian-filtering view of the same area, overlaid with the atomic structure model. Subfigure (g) shows the FFT of the full HAADF-STEM image (not displayed here). By performing an inverse FFT including all reflections along the [0 0 2] and [0 2 0] reciprocal lattice lines, the corresponding lattice planes were reconstructed and overlaid in color with the HAADF-STEM image in panel (f). Early stages of film morphology were further explored with in-situ room-temperature STM on partially grown EFA layers without breaking vacuum[3]. As the films are typically capped to prevent oxidation, AFM under ambient conditions was less informative. In the STM procedure, growth was paused as RHEED indicated surface roughening (∼1 nm according to QCM), then the sample was transferred to a compatible STM system via a vacuum transfer arm. After imaging, the sample was returned to the MBE chamber to continue growth until RHEED streaks appeared (∼3.6 nm according to QCM). A further iteration under these conditions, involving interrupting growth, was not possible, as epitaxial growth could not be continued. An STM surface analysis of a slightly thicker sample (∼5.6 nm) was performed on a separate sample. The full process is illustrated in Figure 4.2. Line profiles confirm layer-by-layer growth, with indications of possible half-layer steps of ∼0.6 nm. Taken together, these results show that growth quality follows a reproducible hierarchy: Fluxes that produce strongly off-stoichiometric films result in amorphous or polycrystalline growth, approximate stoichiometry leads to 3D island formation, and when the substrate temperature is carefully optimized, fully epitaxial films can be obtained. Flux ratios of about 1:1:2 with slight As overpressure are optimal, whereas excessive As destabilizes the surface. In-situ room-temperature STM confirms the nucleation of monolayer islands, and XRD and TEM demonstrate

[3]Support of Anshuman Padhi and Jingrong Ji for STM measurements is gratefully acknowledged.

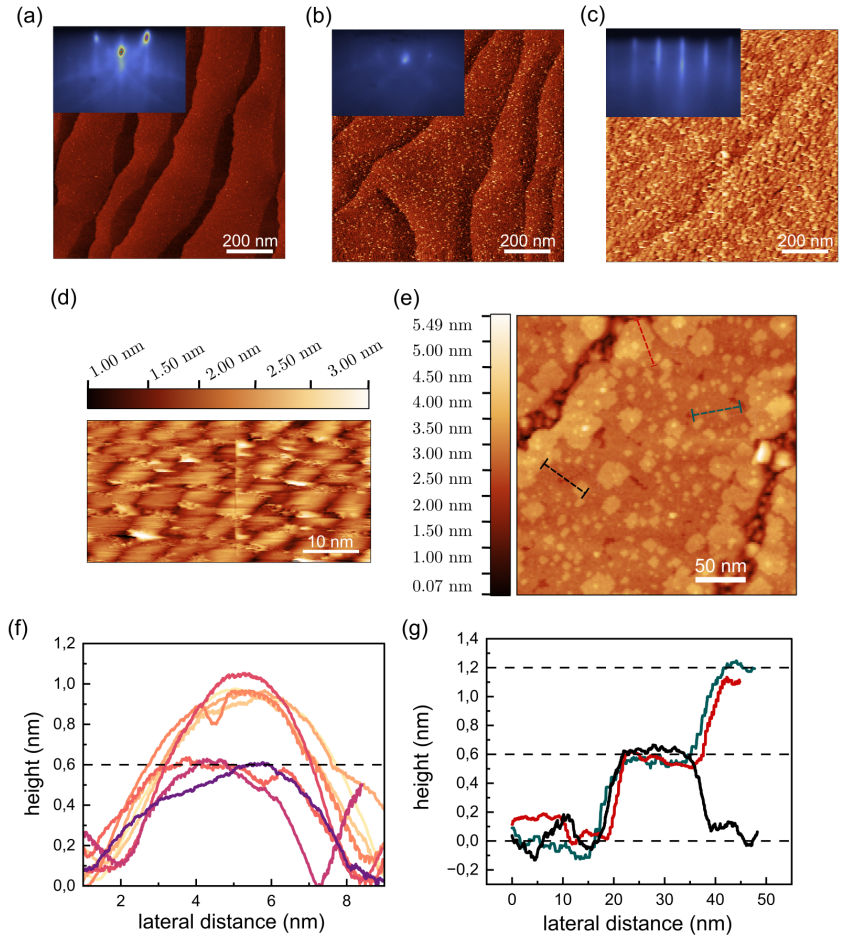


Figure 4.2: (a–d) STM images at different stages of growth: (a) the pristine STO(1 0 0) substrate; (b) a film thickness of ∼1 nm, where the substrate RHEED lines become blurred; (c) ∼3.6 nm, when film RHEED lines start to appear; (d) higher-resolution zoom-in at ∼3.6 nm. (e) STM image of a separate sample at ∼5.6 nm. (f) Line profiles of (d), revealing two characteristic step heights. The smaller height of ∼0.6 nm corresponds to half-unit-cell steps. (g) Line profiles of (e), showing further coalescence of the previously irregular growth centers into extended flat terraces. Step heights again occur in multiples of 0.6 nm (half-unit cells).

c-axis orientation and high crystallinity. These findings establish robust conditions for EFA thin films as a platform for further substitution and doping studies.

4.2 Extending Growth to the P-Substituted System

P-substituted EFAP extends the 122 phase by partially replacing As with P. This substitution is nominally isoelectronic, providing a pathway to tune structural,

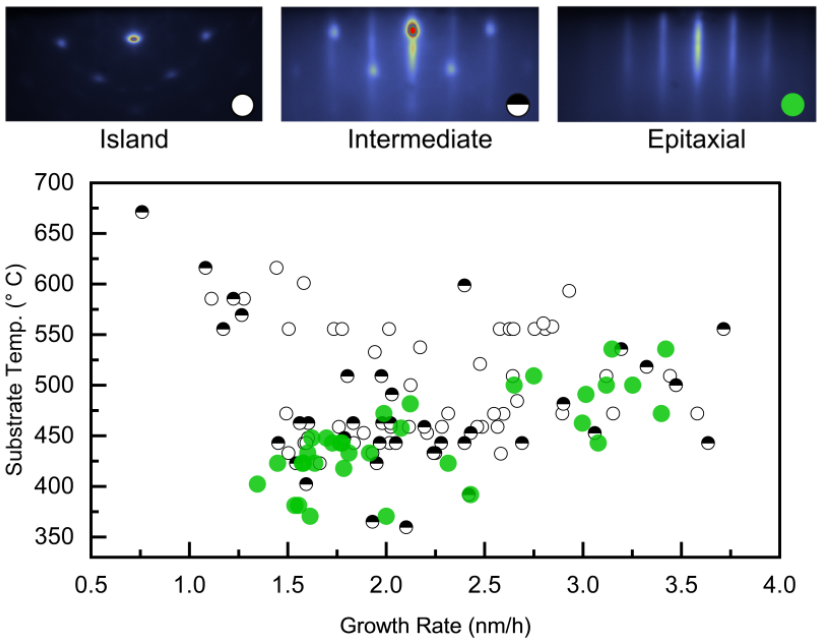


Figure 4.3: Growth rate vs. substrate temperature for EFAP films. Each point corresponds to a single sample, with morphology classified from RHEED: green circles indicate purely epitaxial films with streaks only, half-filled circles represent mixed epitaxial/island growth with both streaks and spots, and open white circles (black outline) denote island-type growth. Representative RHEED patterns used for classification are shown in the top row.

magnetic and electronic properties without strongly altering carrier density. In this work, we achieved P/(As+P) ratios up to 0.35 on STO. As described in Chapter 2, the incorporation of P was controlled using a GaP source with a Ga trapping unit, identical to the cell of GaAs. Varying the BEP of P between approximately 0.15×10^{-12} Torr and 0.3×10^{-12} Torr produced films with up to 35% P/(As+P) on STO. The actual incorporation is not strictly linear with source temperature. Although EFAP shares a similarly small lattice mismatch with STO as EFA, starting growth with a thin EFA seed layer of about half a unit cell often improved subsequent EFAP crystallinity and suppressed early-stage islands.

Combining EFA and EFAP films reveal a correlation between substrate temperature, growth rate, and resulting growth mode, which was already mentioned in the previous chapter but could not be fully assessed for EFA due to limited statistics. Figure 4.3 maps the observed growth morphologies in the substrate temperature–growth rate plane. Each data point is marked according to the RHEED pattern:

green circles correspond to purely epitaxial films with streaks only, half-filled circles indicate mixed epitaxial/island-type growth with both streaks and spots, and open white circles (with black outline) denote island growth. The boundary separating 2D and 3D modes follows an approximately linear trend, albeit with scatter in the data, reminiscent of the critical conditions separating step-flow from random nucleation growth in GaAs and related systems (see Chapter 2.1, and, in particular, Figure 2.2). Thus, EFAP provides the systematic evidence that the effective growth window shifts with deposition rate.

Ex-situ structural characterization confirm RHEED observations further. Out-of-plane X-ray diffraction scans reveal EFAP (0 0 l) reflections near 15°, 30°, 46°, 62°, and 81°, while the STO substrate peaks appear at ∼22.8°, 46.5°, and 72.6° (Figure 4.4). The c-axis lattice parameter remains close to 12 Å, with systematic shifts as the P fraction increases, in good agreement with bulk values displayed in the same figure.

High-resolution STEM and atomic-resolution EDX mapping provide further insight into the structural and compositional properties of EFAP thin films. Figure 4.5 presents a representative dataset for a sample with more than ∼35% P/(As+P). Panels (a)–(d) display atomic-resolution EDX maps (5 nm field of view, (1 0 0) orientation) of Eu, Fe, As, and P, respectively. A Wiener filter was applied to the STEM-EDX maps for noise reduction. Circular markers highlight the regions subsequently enlarged in panels (e)–(f), where the elemental maps are overlaid with the corresponding atomic structure model. Panel (i) shows line profiles obtained by averaging the elemental intensities along the a-axis (perpendicular to the growth direction). To guide the eye, the atomic model is again included, with lines connecting each atomic species to its corresponding profile. The STEM images confirm that EFAP preserves the layered crystal structure characteristic of EFA, consistent with the tetragonal $I4/mmm$ space group.

The crystal lattice is well ordered within the field of view, and the averaged line scans reveal a distinct modulation in the substitution pattern. Specifically, P atoms do not occupy As sites uniformly but instead exhibit alternating layers with

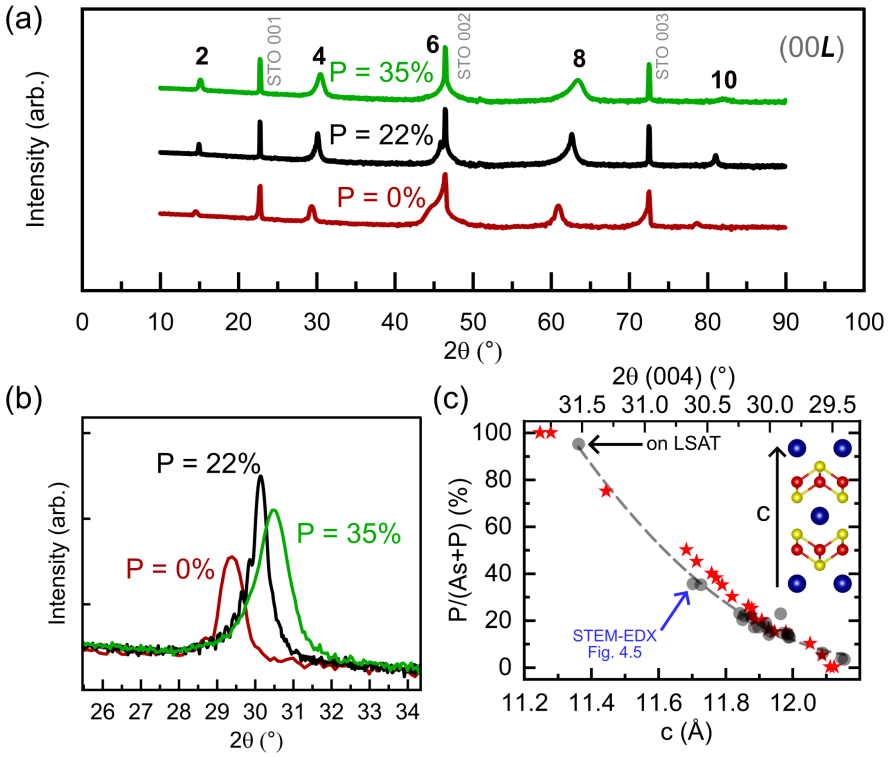


Figure 4.4: (a) Out-of-plane XRD θ–2θ scans of EFAP films with P/(As+P) = 0, 22, and 35% (intensities offset for clarity). (b) Enlarged view of the (0 0 4) reflections with peak fitting. (c) P content vs. c-axis lattice parameter extracted from the (0 0 4) peak position (bottom axis), with corresponding 2θ values on the top axis. Red stars indicate bulk values from the literature [101, 110]. The c-axis decreases systematically with increasing P substitution. The film with ∼95% P/(As+P) was grown on LSAT rather than STO, since higher P levels also reduce the in-plane lattice constant; this data point should therefore be interpreted with caution. Dashed line is a guide to the eye. Blue arrow highlights a sample that is further studied by STEM-EDX in Figure 4.5.

higher and lower P incorporation. This modulation is also reflected in the As signal, which alternates between high- and low-intensity layers, with minima coinciding with the P maxima. Such behavior suggests a non-random substitution mechanism, potentially associated with site-selective energetics during growth. While this could in principle be described as alternating "A" and "B" sites, we avoid such notation here, since its crystallographic consistency remains uncertain. Importantly, this modulation is not a local anomaly: it is observed across multiple regions in the lamellae. Furthermore, the same behavior was detected in a second lamella with ∼22% P/(As+P). Although weaker due to the lower P content, the modulation persists. This latter sample is superconducting, while the $>$ 35% P sample is not,

which motivated the repeated measurement to verify whether superconducting compositions also exhibit the same substitution pattern. EDX Maps of P an As on the other sample are given in the additional materials Chapter A.

Panel (j) presents the full EDX spectrum obtained from the 5×5 nm^2 region. The characteristic Eu L, Fe K, As K, and P K lines used for elemental identification are marked. Quantification of this window yields $Eu_{1.12}Fe_2As_{1.17}P_{0.78}$, while RBS measurements on the same sample, averaged over a much larger region, give $Eu_{0.9}Fe_2As_{1.4}P_{0.9}$. The discrepancy between the two results arises from the different element sensitivities and limitations of the techniques, particularly the difficulty of quantifying P by RBS due to overlap with the Ti edge from the STO substrate, as detailed in Chapter 2.2.2.

Two additional considerations should be noted. First, the Fe signal appears to show small peaks at Eu lattice positions. While this could suggest partial Fe substitution on Eu sites, it is more likely an artifact of peak overlap between the Fe K and Eu L_β lines, as can be seen in panel (j), leading to partial misattribution of Eu counts to Fe. Second, faint line-like features in the EDX maps may raise questions about spatial inhomogeneity. However, these are likely artifacts of projection geometry: in the (1 0 0) view, the Fe–Fe spacing is the smallest among the elements and thus difficult to resolve. To test this interpretation, a (1 1 0) oriented lamella was examined for a different sample. In that geometry, the Fe spacing along the in-plane direction becomes larger, while the Eu spacing becomes comparatively closer. The maps indeed confirm this: Fe sites are well resolved in the (1 1 0) cut, whereas the Eu in-plane resolution is reduced. These observations validate the interpretation that the line features in the (1 0 0) projection arise from resolution limits rather than genuine inhomogeneity. Results of the (1 1 0) cut lamellae are presented in the additional materials Chapter A.

Taken together, these results demonstrate that EFAP thin films can be grown with up to ∼35% P substitution on STO (1 0 0) while preserving the 122 crystal structure. These films provide a robust platform for studying how isoelectronic

P doping modifies magnetism and potentially induces superconductivity in the $EuFe_2As_2$ family.

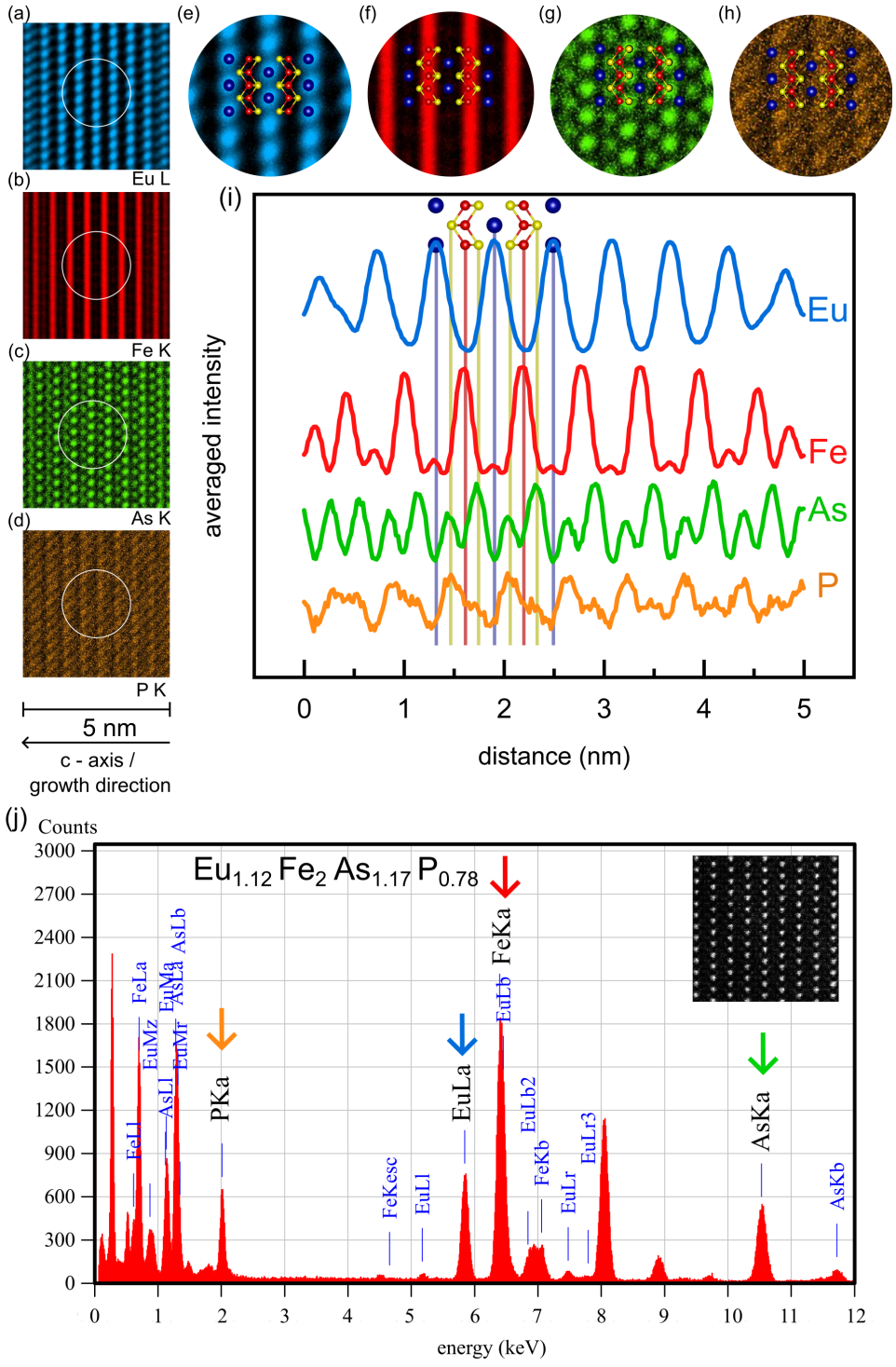


Figure 4.5: High-resolution STEM and atomic-resolution EDX of EFAP with more than ∼35% P/(As+P). A Wiener filter was applied to the Maps for noise reduction. (a)–(d) Elemental EDX maps of Eu, Fe, As, and P (5×5 nm^2, (1 0 0) orientation). (e)–(f) Enlarged region overlaid with the atomic structure model. (i) Averaged elemental intensities along the *a*-axis with model overlay. (j) EDX spectrum from the same 5×5 nm^2 region, corresponding to the maps in (a)–(d). Colored arrows indicate at which energies the maps were retrieved.

5
Transport Measurements

This chapter presents a comprehensive investigation into the electrical transport properties of the synthesized EFAP thin films, from foundational characteristics to quantum interference effects.

The discussion begins by establishing the systematic evolution of superconductivity as a function of doping and film thickness, culminating in a comprehensive electronic phase diagram for the material family. Following this broad overview, the focus narrows to a single, representative sample patterned into a microbridge. Its response to high magnetic fields is analyzed to determine the upper critical field and explore the characteristics of its multi-band superconductivity. The analysis then turns to the normal state of this device, where its magnetoresistance and Hall effect are deconstructed using a three-carrier framework. Finally, the chapter concludes by probing the superconducting pairing state directly through Little-Parks experiments on a ring-shaped device.

Contents

5.1 Systematics of the Superconducting Phase Diagram . 72
5.2 Field-Dependent Properties of a Representative Device 75
5.3 Normal State Transport and Multi-Carrier Analysis . 82
5.4 Magnetoresistance Oscillations in Square Rings 87

5.1 Systematics of the Superconducting Phase Diagram

This section provides an overview of the foundational transport characteristics, beginning with the non-superconducting parent compound. It then explores the emergence of superconductivity as a function of both relative P content (x = P/(As+P)) and film thickness. All measurements were conducted on the non-patterned, as-grown films utilizing a four-probe van der Pauw geometry.

The Parent Compound: $EuFe_2As_2$

The temperature-dependent resistivity of the parent compound is presented in Figure 5.1(a). The data, normalized to its room temperature value, is shown for a representative 17 nm thick film. The sample exhibits characteristic metallic behavior, with its resistance decreasing upon cooling from room temperature to 2 K. Two distinct features are observable in the curve. First, an abrupt peak near 172 K corresponding to the SDW transition associated with the Fe sublattice. Second, a smaller anomaly at approximately 19 K consistent with the Néel temperature for the antiferromagnetic ordering of the Eu^{2+} spins. Both transitions are consistent with reports on the bulk material [45]. As expected for undoped EFA, no superconducting transition is observed at low temperatures.

Variability in Phosphorus-Induced Superconductive Samples

P substitution successfully induced superconductivity. Figure 5.1(b) displays a collection of resistance-temperature curves for several epitaxial
EFAP films with clear RHEED streaks assessing high-quality epitaxy. Despite only choosing comparable crystalline quality, the transport behavior shows considerable variation, which does not correlate straightforwardly with simple parameters like film thickness or the nominal P content determined by EDX.

The normal-state behavior across these superconducting films is notably diverse. Some samples display a conventional metallic decrease in resistance upon cooling, while others exhibit a more strange-metallic linear temperature dependence that

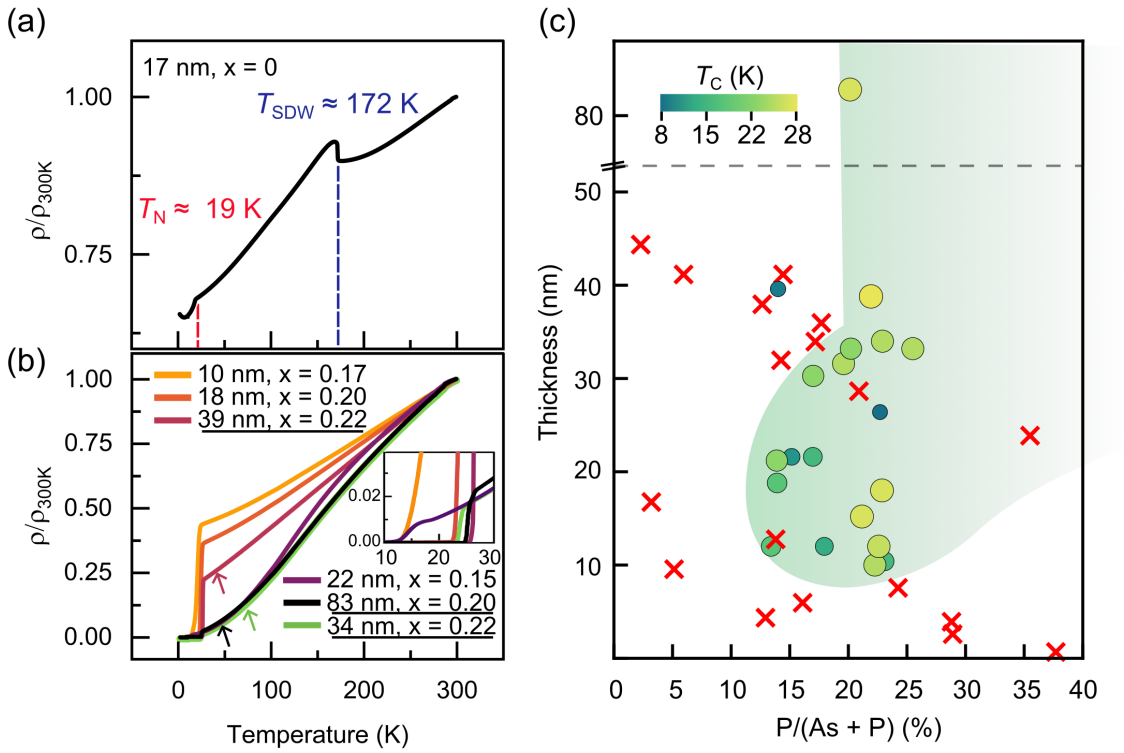


Figure 5.1: (a) Temperature-dependent normalized resistivity (ρ/ρ_{300K}) curves of as-grown EFA thin film. The abrupt peak near 172 K is attributed to the SDW transition, whereas a small anomaly near 19 K corresponds to the Néel ordering of Eu^{2+}. (b) Same curves for P-induced superconductive EFAP films. Films with a variety of thicknesses and P-content are shown. As described below in this section, no clear trend can be observed. Highlighted films with arrows are also described further in the text below. Inset shows a zoomed in plot. (c) Phase diagram with thickness vs. P-content for the subset of epitaxially grown samples. Epitaxial quality was assessed by RHEED showing clear streaks.

persists down to the superconducting transition temperature. A third category of films even shows a slight resistive upturn before the onset of superconductivity. This pronounced variability is likely a signature of the system's proximity to a quantum critical point, where minor fluctuations in local stoichiometry, defect density, or strain can profoundly alter the electronic scattering mechanisms [157].

To illustrate this complexity, three specific curves in Figure 5.1(b) are indicated by arrows, with their corresponding labels underlined. The green and crimson curves correspond to films with nearly identical P content ($x \approx 0.22$) and similar thicknesses (34 nm and 39 nm, respectively). However, the former (green) has a classic metallic profile, while the latter (crimson) shows a linear temperature

dependence. Furthermore, the metallic behavior of the green curve more closely resembles that of the black curve, which represents a sample that is significantly thicker (83 nm) and has a slightly lower P content ($x \approx 0.20$).

Thickness-Dependent Superconducting Phase Diagram

To systematically investigate the relationship between superconductivity, film thickness, and composition, a phase diagram was constructed, as shown in Figure 5.1(b). This diagram plots the superconducting transition temperature as a function of film thickness and relative P content. Each data point represents a sample of high epitaxial quality. The value of T_c is indicated by a color scale (from blue for lower T_c to yellow for higher T_c), and the size of the data point is scaled with T_c to guide the eye. Samples that did not exhibit superconductivity are marked with a red cross.

The resulting phase diagram reveals several key trends. First, the superconducting dome in our thin films appears to extend to lower P concentrations than has been reported for bulk single crystals [16]. Second, the diagram seems to suggest a clear thickness threshold, films thinner than approximately 8 nm appearing non-superconducting while thicker ones ($\gtrsim 20$ nm) exhibit a well-defined superconducting dome with a maximum near $x \approx 0.20 - 0.25$. This apparent cutoff should not be interpreted as a fundamental limit, but rather as a limitation of the employed measurement techniques, such as the transport measurements shown here, but also SQUID magnetometry. As shown by low-temperature STM measurements (additional materials chapter B), even a 4 nm film tentatively indicates the presence of a superconducting gap, suggesting that superconductivity might persist below the transport detection threshold. These observations are presented as supplementary information, as they rely on a limited dataset but nonetheless offer qualitative support for this interpretation. In general, the observed phase diagram remains broadly consistent with previous reports [16], though quantitative comparison of absolute doping levels is complicated by factors such as EDX calibration and substrate-induced strain.

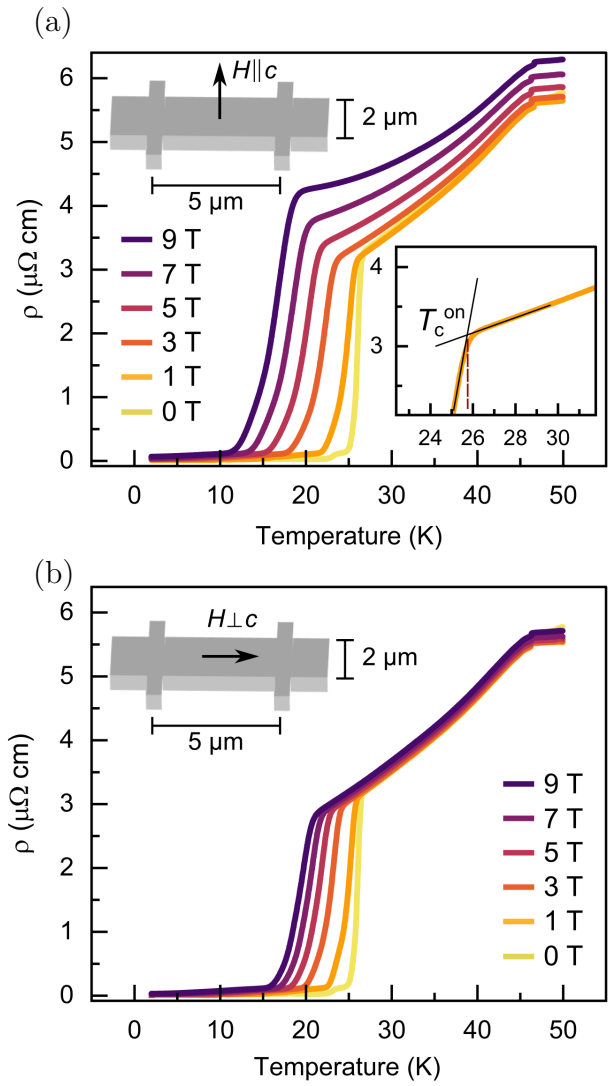
Overall, these results suggest some thickness-dependent evolution of the superconducting phase. However, it is also crucial to consider that the determination of P content carries a larger uncertainty for thinner films. Specifically, the presence of the non-superconducting EFA buffer layer, while only a single unit cell thick, becomes more significant in the overall EDX signal for very thin films. This could systematically shift the calculated P/(As+P) ratio to lower values, an effect that must be considered when interpreting the precise boundaries of the phase diagram.

5.2 Field-Dependent Properties of a Representative Device

Given the observed variability in the normal-state transport properties, which did not correlate strongly with film thickness, epitaxy or P content, a single sample was selected for detailed magnetotransport studies. We chose the thickest film (83 nm, $x \approx 0.20$, black curve in Figure 5.1(b) for this purpose, as it demonstrated the highest resilience and yield during the patterning of Hall-bar structures[1]. This pragmatic choice ensured the fabrication of a high-quality device suitable for low-noise measurements of longitudinal and transverse resistivity. The device was patterned with a contact strip geometry of (2×5) μm^2 for the field-dependent measurements presented hereafter. Figure 5.2 displays the longitudinal $\rho - T$ curves in various applied fields (0 to 9 T), for field orientations out-of-plane (OOP, $H \parallel c$) and in-plane (IP, $H \parallel ab$). In zero field, a superconducting onset transition at $T_c \approx 27$ K can be recorded. Under applied magnetic field, the superconducting transition shifts to lower temperature and broadens slightly, as seen in Figure 5.2. Nonetheless, even at the highest fields (9 T), the resistance eventually falls to zero at lower T, indicating the patterned sample still achieve a fully superconducting state. As expected T_c is more strongly suppressed by OOP field than by IP fields: for a given H, the transition in $\rho(T)$ occurs at a lower temperature when $H \parallel c$ compared to $H \parallel ab$. For example, a 9 T perpendicular field causes reduction to $T_c \approx 18.4$ K, while the same 9 T applied IP causes reduction to $T_c \approx 20$ K. This

[1]Device fabrication was performed by Jiho Yoon, whose support is gratefully acknowledged.

reflects the greater effectiveness of $H \perp$ layers in orbital pair-breaking, consistent with observations in other FeSCs [16].



(c)

$\mu_0 H$ (T)	T_c^{on} (K)	T_c^{90} (K)	T_c^{50} (K)	T_c^{10} (K)
0	26.7	26.4	26.0	25.3
1	25.8	25.5	24.6	22.6
3	23.3	22.9	21.7	19.0
5	21.5	21.0	19.6	16.6
7	19.9	19.4	17.8	14.6
9	18.5	17.8	16.1	12.9

(d)

$\mu_0 H$ (T)	T_c^{on} (K)	T_c^{90} (K)	T_c^{50} (K)	T_c^{10} (K)
0	26.7	26.4	26.0	25.3
1	25.8	25.6	24.9	23.1
3	24.0	23.6	22.7	20.6
5	22.7	22.3	21.2	19.1
7	21.7	21.2	20.0	17.8
9	20.8	20.3	19.0	16.7

Figure 5.2: (a, b) Resistivity as a function of temperature data obtained for different OOP and IP fields, respectively. The inset illustrates the method for determining the onset transition temperature, T_c^{on}. Other criteria are defined relative to the resistivity value at this onset point. (c, d) Tables showing extracted critical temperatures from (a) and (b), based on different resistivity drop criteria.

Estimate of $H_{c2}(0)$ by the Werthamer-Helfand-Hohenberg model

To quantify the field-induced shift of the superconducting transition, the onset temperature T_c^{on} is defined as the intersection point between a linear fit to the normal-state background and the line corresponding to the steepest slope of the

resistive transition. This construction is illustrated in Figure 5.2. In addition to T_c^{on}, characteristic temperatures have been extracted at which the resistivity has dropped to 90%, 50%, and 10% of its normal-state value just above the transition. Using these definitions, one can extract characteristic T_c values at each field and for the different field orientations. Tables 5.2(c) and (d) compile the estimated T_c for each criterion. It should be emphasized that all definitions consistently show a decrease of T_c with increasing field, and a broadening of the transition width. From these data, the upper critical field $H_{c2}(T)$ can be determined without the need for a separate measurement protocol. As, for each fixed field, a characteristic T_c can be identified as described above; assigning the corresponding field value to H_{c2} at that temperature yields $H_{c2}(T)$ for the specific case $T = T_c$. Plotting $H_{c2} - T$ in this way constructs the phase boundary. To get an upper boundary first, T_c^{on} is used.

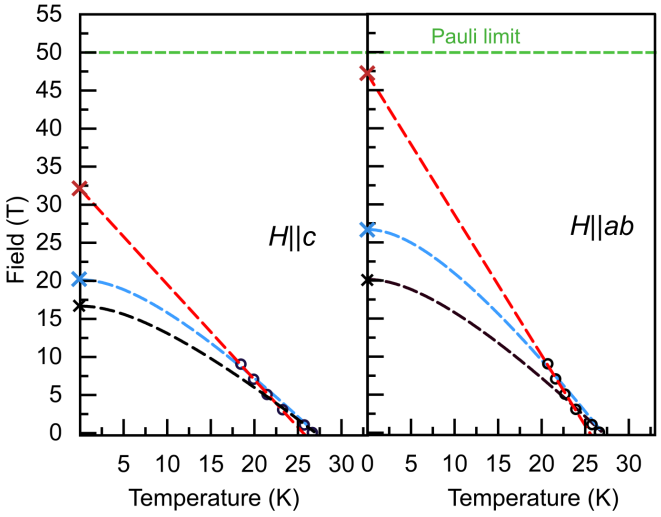
The obtained diagram is presented in Figure 5.3(a). The results for the other resistivity criteria is shown in 5.4. A pronounced upward curvature in the $H_{c2}(T)$ data is visible at lower temperatures, present for both IP and OOP field orientations. This concave shape deviates from the standard behavior predicted by conventional superconductivity models. A detailed discussion of the theoretical models that can account for this curvature will be the central topic of the next section. Before getting into the details of that analysis, it is a necessary prerequisite to establish a quantitative estimate for $H_{c2}(0)$. Since the standard WHH model (see section 3.1) fails to capture the observed curvature, a pragmatic estimate for the $H_{c2}(0)$ range was obtained. The analysis focused on the dataset from the onset resistance criterion, which is the most suitable, due to its less pronounced concave shape. The WHH model, with $\alpha = 0$ and $\lambda_{SO} = 0$, was applied to two different regions of the data: one within 5 K of T_c and another across the full measured range. Additionally, a simple linear fit to the low temperature linear region was included to establish an upper boundary for the estimate. Notably, even the highest extrapolated value ($\approx$47 T) remains below the Pauli paramagnetic limit ($H_P \approx 50$ T). The results of these three estimation methods are compiled in Figure 5.3. Table 5.3(b) also contains the

corresponding coherence lenghts. These were calculated using the anisotropic GL relations, as desribed in Chapter 3.1 and restated here for completeness:

$$\xi_{ab} = \sqrt{\frac{\Phi_0}{2\pi H_{c2}^{c}(0)}}, \quad \text{and} \quad \xi_c = \frac{\Phi_0}{2\pi \xi_{ab} H_{c2}^{ab}(0)},$$

where $\Phi_0 = 2.0678 \times 10^{-15}\,\mathrm{Wb}$ is the magnetic flux quantum, $H_{c2}^{c}(0)$ denotes the upper critical field measured with the field along the c-axis (OOP), and $H_{c2}^{ab}(0)$ with the field parallel to the ab-plane (IP).

(a)



(b)

	$\mu_0 H_{c2}^{c}(0)$ (T)	$\mu_0 H_{c2}^{ab}(0)$ (T)	$\xi_{ab}(0)$ (nm)	$\xi_c(0)$ (nm)
✗	16	20	4.54	3.63
✗	20	27	4.06	3.00
✗	32	47	3.21	2.18

Figure 5.3: (a) Temperature dependence of the upper critical field, $H_{c2}(T)$. The left (right) panel corresponds to the OOP (IP) field orientation. Data points were extracted from $\rho(T)$ measurements. The data is compared to three different fitting models represented by dashed lines: The black dashed lines are fits using the WHH model ($\alpha = 0$, $\lambda_{SO} = 0$) applied only to data near T_c (within 3 K). The blue dashed lines are WHH fits applied to the entire temperature range. The red dashed lines are linear fits to the high-field, low-temperature region. The standard WHH model fails to capture the prominent upward curvature. The crosses on the vertical axis show the zero-temperature extrapolations, $H_{c2}(0)$, for each corresponding fit. The green dashed line represents the Pauli limit. (b) A summary of the extrapolated critical field values, $H_{c2}^{ab}(0)$ and $H_{c2}^{c}(0)$, derived from the three fitting methods. The coherence lengths calculated from these values, as described in this section, are also listed.

On the Origin of the Upward $H_{c2}(T)$ Curvature

Returning now to the prominent upward curvature of the $H_{c2}(T)$, this section evaluates its potential physical origins. The curvature is more evident when using

the 10% resistivity criterion. Such a criterion dependent upturn is commonly associated with vortex melting [158], corresponding physically to a transition from a vortex solid phase to a vortex liquid phase. To quantify this transition, the data are typically fitted using the empirical power-law function:

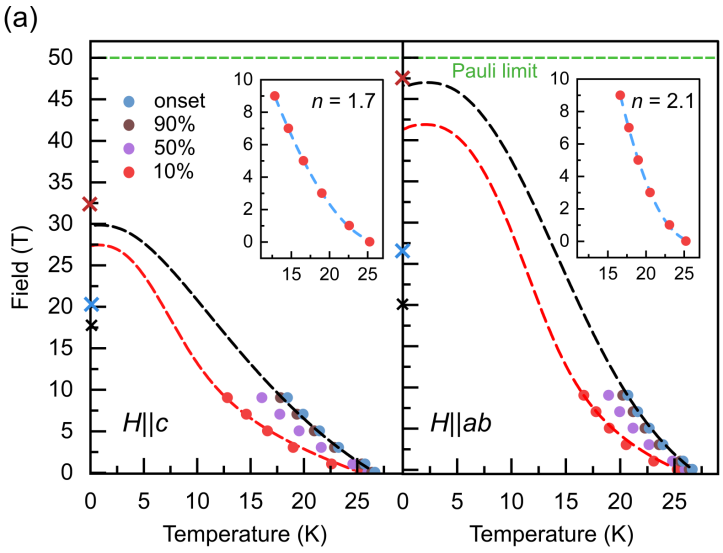
$$H_{c2}(T) \propto \left(1 - \frac{T}{T_c}\right)^n. \tag{5.1}$$

Fits of this form for the 10% criterion curves, indicated by blue dotted lines in the in Figure 5.4, yield exponent values of $n = 1.7$ for the OOP orientation and $n = 2.1$ for the IP orientation. These values align well with those reported for a broad range of superconductors, from $YBa_2Cu_3O_{7-\delta}$ to structurally similar FeSCs such as $Ca_{10}(Pt_{4-\delta}As_8)(Fe_{2-x}Pt_xAs_2)_5$ [159] and $Ba(Fe_{1-x}Co_x)_2As_2$ [160], despite differences in the precise criteria used to determine the melting line. While the upward curvature in $H_{c2}(T)$ can be attributed to vortex dynamics, several factors suggest that intrinsic properties of the superconductor may be at play in this case. The observed concave shape is pronounced even when using a high resistivity criterion to define T_c, a regime where the influence of vortex melting is expected to be minimal. Furthermore, the resistive transitions in the presence of a magnetic field exhibit only modest broadening. This is in contrast to some systems where thermal vortex fluctuations have been proposed to cause the upward trend, such as in $Ca_{10}(Pt_{4-\delta}As_8)(Fe_{2-x}Pt_xAs_2)_5$, which show a much more significant broadening effect [159]. To quantify the potential influence of thermal fluctuations, an estimate utilizing the Ginzburg-Levanyuk number G_i may help. It is given by [116]

$$G_i = 1.07 \times 10^{-13} \frac{\kappa^4 T_c^2}{\mu_0 \epsilon^2 H_{c2}(0)}, \tag{5.2}$$

where $\kappa = \lambda/\xi$ is the Ginzburg-Landau parameter and ϵ is the anisotropy factor. Using a literature value for the London penetration depth of $\lambda \approx 350\,\text{nm}$ [113] and the coherence length $\xi_{ab}(0)$ calculated from our critical field data via GL theory, we obtain $G_i \approx 0.69 \times 10^{-3}$. This value is slightly lower than that reported for P-doped $BaFe_2As_2$ [161] and is $10 - 30$ times smaller than values for NdFeAs(O,F)

[162], placing our material in the range of moderate thermal vortex fluctuation effects for 122-type FeSCs.



(b)

	λ_{11}	λ_{22}	λ_{12}	sym.
$H^{on}_{c2,c}$	0	0	0.5	$s^{\pm}$
$H^{10\%}_{c2,c}$	0.82	0.44	0.3	s^{++}
$H^{on}_{c2,ab}$	0.25	0.5	0.5	$s^{\pm}$
$H^{10\%}_{c2,ab}$	0.59	0.48	0.25	s^{++}

Figure 5.4: (a) $H_{c2}(T)$ curves obtained using different resistivity drop criteria, as defined in the text above. The left (right) panel corresponds to the OOP (IP) field orientation. Red and black dashed lines represent simulated fits to the 10% and onset criteria curves, respectively. Inset shows fits of the data obtained by 10%-criteria with a power-law function (equation (5.1)). Colored crosses indicate extracted critical field value range from Figure 5.3. (b) Corresponding table summarizing the coupling parameters extracted from the simulated curves.

An alternative and compelling explanation is the intrinsic two-band nature of superconductivity in this material, an argument already invoked in 2008 for $LaFeAsO_{0.89}F_{0.11}$ [163] and shortly after for $NdFeAsO_{0.7}F_{0.3}$ [164]. In the latter case, the authors argued that the upward trend in $H_{c2}(T)$ reflects an intrinsic property of the oxypnictides rather than effects from vortex melting or pinning. This assessment appears to hold more generally across FeSCs, as underlined by its more recent applications, e.g., for $CaKFe_4As_4$ [165] or FeSe [166]. As described in Chapter 3.1, the theoretical model for two-band superconductivity developed by Gurevich [137, 138] can produce a concave temperature dependence of $H_{c2}(T)$. Since the material is in the clean limit ($\xi \ll \ell$), due to the typically short coherence lengths in FeSCs [5, 6], the corresponding formulation should be used. For clarity,

the defining equations of this model are reiterated here:

$$a_1\Big[\ln(t)+U_1\Big]+a_2\Big[\ln(t)+U_2\Big]+\Big[\ln(t)+U_1\Big]\Big[\ln(t)+U_2\Big]=0,$$

where the terms are defined as follows:

$$\begin{aligned}
U_1 &= U(t,h,\alpha,1,1), & U_2 &= U(t,h,\alpha,\nu,s),\\
a_1 &= \frac{\lambda_0+\lambda_-}{2w}, & a_2 &= \frac{\lambda_0-\lambda_-}{2w},\\
\lambda_- &= \lambda_{11}-\lambda_{22}, & \lambda_0 &= \sqrt{(\lambda_{11}-\lambda_{22})^2+4\lambda_{12}^2},\\
w &= \lambda_{11}\lambda_{22}-\lambda_{12}^2.
\end{aligned}$$

The function $U(t,h,\alpha,\nu,s)$ is given by the integral:

$$U(t,h,\alpha,\nu,s) = 2^{q^2 s}\mathrm{Re}\sum_{n=0}^{\infty}\int_{q\sqrt{s}}^{\infty} e^{-u^2}\left[\frac{u}{n+1/2}-\frac{t}{\sqrt{h\eta}}\arctan\left(\frac{u\sqrt{h\eta}}{t(n+1/2)+i\alpha h}\right)\right]du,$$

and the physical parameters are:

$$\begin{aligned}
h &= \frac{\hbar^2 v^2 H}{8\pi\phi_0 k_B^2 T_c^2}, & \alpha &= \frac{4\mu\phi_0 k_B T_c}{\hbar^2 v_1^2},\\
q^2 &= \frac{Q_z^2\phi_0\epsilon_1}{2\pi H}, & \eta &= \frac{v_2^2}{v_1^2},\\
s &= \frac{\epsilon_2}{\epsilon_1}.
\end{aligned}$$

Here, t is the reduced temperature T/T_c, H is the external field, v_i are Fermi velocities of band i, Q_z is the magnitude of the Fulde-Ferrell-Larkin-Ovchinnikov modulation and ϵ_i are related to the effective mass anisotropies of each band i. Due to the limited magnetic field range of our measurements, the parameter space for the model is large, and a unique set of fitting parameters cannot be determined. However, the model can successfully reproduce the experimental data using physically reasonable parameters. The simulation of the upper critical field was undertaken to provide a proof-of-concept for a two-band model, rather than to obtain a definitive fit. Initially, an $s^{\pm}$ pairing state is assumed by setting the coupling constants to $\lambda_{11}=\lambda_{22}=0$ and $\lambda_{12}=\lambda_{21}=0.5$, consistent with other

FeSCs [165–171]. Effects of an FFLO state were considered negligible ($Q_z = 0$), and s is set as 1, setting the same anisotropy across different bands. By establishing a baseline comparison with the OOP, high-resistance criterion data, the other parameters were determined to be $v_2 = 1.5 \times 10^5\,\mathrm{m/s}$ and $\eta = 0.01$. α was set to 0.05 so the extrapolated $H_{c2}(0)$ does not surpass the upper limit obtained from a linear fit. While not a physical requirement, this value, much like Q_z, cannot be reliably assessed without high-field data. These last three parameters were then fixed for subsequent simulations of data from other field orientations and the low-resistance criterion, where only the inter- and intraband coupling constants λ_{ij} were adjusted. It should be emphasized that this approach does not yield a unique solution but serves to underline that the two-band model is a possible intrinsic mechanism to explain the observed behavior. Simulated curves for the onset and 10% criteria in both field orientations are shown in Figure 5.4, together with the corresponding fitting parameters summarized in the adjacent table.

5.3 Normal State Transport and Multi-Carrier Analysis

Magnetoresistance (MR) measurements were conducted on the same samples and device structures described in the previous chapter. All measurements were performed using a fixed current of $1 \times 10^{-4}\,\mathrm{A}$, with magnetic field sweeps from $+14\,\mathrm{T}$ to $-14\,\mathrm{T}$ at four selected temperatures: 23 K, 30 K, 40 K, and 60 K. Since no magnetic hysteresis was observed, and to improve figure clarity, only the $+14\,\mathrm{T} \rightarrow -14\,\mathrm{T}$ sweep is shown and analyzed in the figures.

The MR was calculated from the longitudinal resistivity ρ_{xx} using the standard definition:

$$\mathrm{MR} = \frac{\rho_{xx}(B) - \rho_{xx}(0)}{\rho_{xx}(0)}. \tag{5.3}$$

Figure 5.5(a) displays the resulting MR curves. For the 23 K dataset, the zero-field resistivity $\rho_{xx}(0)$ was determined by fitting a parabolic function to the high-field data, since the low-field region exhibits a rapid drop toward zero, indicative of the

onset of superconductivity [see inset of Figure 5.5(a)]. A positive MR is observed across all temperatures, which is consistent with the electron cyclotron motion and consistent with previous results on the bulk parental compound [172]. Although it should be noted, that upon application of pressure to reach the superconductive region, negative MR has been reported for high fields in the same report [172]. In the measurements provided here, in the highest applied field of 14 T, MR reaches 75% at 23 K, before lower temperatures open a complete gap and cause resistance measurements to drop to zero.

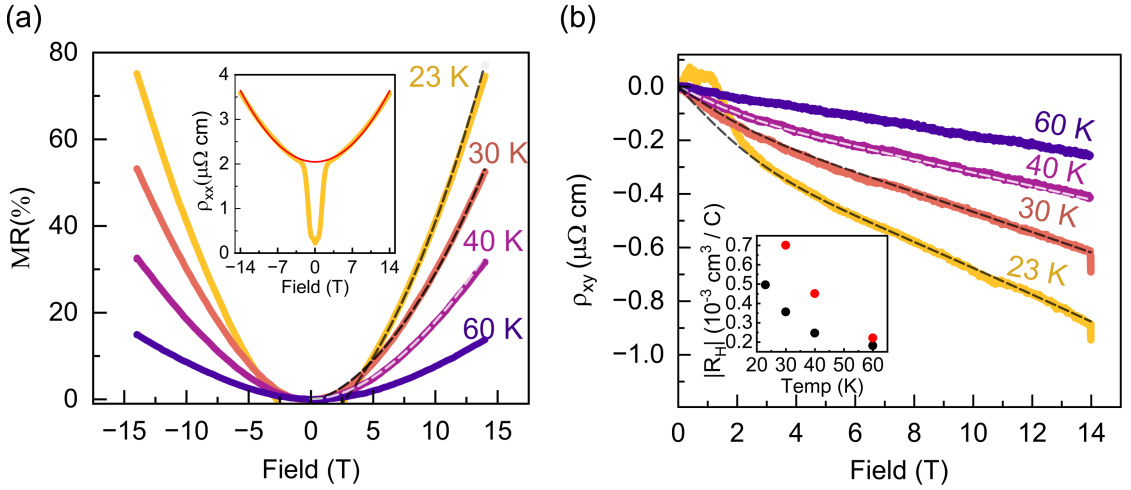
The transverse resistivity ρ_{xy} shows a notable correlation with ρ_{xx}, due to the mixing of longitudinal contributions into the transverse signal. Therefore, antisymmetrization was applied to isolate the genuine Hall response:

$$\rho_{xy} = \frac{\rho_{xy}(+B) - \rho_{xy}(-B)}{2}. \tag{5.4}$$

Each $-B$ value was inferred from a single sweep, which makes the antisymmetric signal explicitly antisymmetric with respect to the magnetic field by construction, and a single branch contains all relevant information.

The Hall coefficient, R_{H}, was determined from the slope of the antisymmetrized Hall resistivity, which is presented in Figure 5.5(b). To account for the non-linear field dependence of the resistivity, linear fits were performed separately on two distinct regions: the high-field region and the low-field region (0 to 2 T). The temperature dependence of the coefficients extracted from the high-field slope (black dots) and the low-field slope (red dots) is shown in the figure's inset. The 23 K data was excluded from the low-field analysis, as the resistive drop caused by the onset of superconductivity cannot be interpreted using a classical Hall effect model.

The extracted R_{H} values are on the order of $-10^{-3}\,\mathrm{cm}^3/\mathrm{C}$, with the highest magnitude of $-0.7\times10^{-3}\,\mathrm{cm}^3/\mathrm{C}$ recorded for the low-field slope at 30 K. This value is at least three times smaller than those reported for thin films of $Ba(Fe,Co)_2As_2$, but it is in close agreement with the reported value of $-0.8\times10^{-3}\,\mathrm{cm}^3/\mathrm{C}$ for low field slope of the parent compound under an applied pressure of 3.2 GPa just before T_{c} [172].



(c) **Fitting parameters**

23 K
Carrier densities (10^{20} cm^{-3})
$n_1 = 17.6$, $n_2 = 1.42$
Carrier mobilities (10^3 cm^2/Vs)
$\mu_1 = -0.665$, $\mu_2 = -2.395$
$\mu_3 = 0.490$
30 K
Carrier densities (10^{20} cm^{-3})
$n_1 = 19.7$, $n2 = 0.705$
Carrier mobilities (10^3 cm^2/Vs)
$\mu_1 = -0.548$, $\mu_2 = -2.222$
$\mu_3 = 0.429$
40 K
Carrier densities (10^{20} cm^{-3})
$n_1 = 21.1$, $n_2 = 0.900$
Carrier mobilities (10^3 cm^2/Vs)
$\mu_1 = -0.405$, $\mu_2 = -1.220$
$\mu 3 = 0.350$

(d) **Correlation matrix at 30 K**

	n_1	μ_1	n_2	μ_2	μ_3
n_1	1.000	0.069	-0.513	-0.529	-0.634
μ_1	0.069	1.000	0.804	0.741	-0.787
n_2	-0.513	0.804	1.000	0.966	-0.298
μ_2	-0.529	0.741	0.966	1.000	-0.270
μ_3	-0.634	-0.787	-0.298	-0.270	1.000

Figure 5.5: (a) MR versus field at 23 K, 30 K, 40 K, and 60 K. The inset displays the full ρ_{xx} versus field at 23 K, showing a drop associated with the onset of superconductivity. Consequently, for the calculation of MR, a polynomial fit (red curve) was applied to estimate $\rho_{xx}(0)$. Dashed lines represent fits to the three-carrier model. (b) Corresponding ρ_{xy} versus field at the same temperatures, where a non-linear trend is observed at low fields. Dashed lines indicate the same three-carrier model fit, which is applied simultaneously to both ρ_{xx} and ρ_{xy} to obtain consistent shared parameters. The inset shows R_{H} calculated under the assumption of a single-band model in the high-field linear region (black dots) and low-field linear region (red dots). (c) Fitted parameters of the three-carrier model. (d) Correlation matrix for the 40 K dataset, illustrating interdependence among parameters.

Although this material has been shown to be ferromagnetic, it is unlikely that the observed non-linear anomaly originates from a magnetically driven anomalous Hall effect (AHE). This interpretation is challenged by the fact, that the AHE would appear at temperatures as high as 40 K, which is unexpected, since SQUID measurements indicate a Curie temperature $T_C \approx 24$ K. Although a contribution from slow magnetic ordering above T_C cannot be fully excluded, the most likely explanation is that the non-linearity arises from the material's multi-band electronic structure, rather than from ferromagnetic ordering.

Similar trends have been reported in other FeSCs as well as for the parent compound, where non-linear Hall resistivity in the normal state has been interpreted within a three-carrier model [172]. This interpretation is necessitated by the material's compensated nature, where similar electron and hole carrier concentrations ($n_e \approx n_h$) mean a simpler two-carrier model fails to adequately describe the observed non-linear behavior. Since P doping in EFAP is isovalent, it primarily introduces chemical pressure without directly altering the carrier concentration balance. Therefore, the applicability of a multi-carrier transport scenario extends to the normal state of the P-doped samples studied here, particularly at temperatures just above T_c. A notable difference arises when comparing chemical pressure (doping) with external hydrostatic pressure. In the normal state of the parent compound under sufficiently high hydrostatic pressures, ρ_{xy} has been observed to become linear before the onset of superconductivity [172]. This linearity suggests that a simpler two-carrier compensated model becomes sufficient to describe the charge transport under these conditions. In contrast, the chemically pressure-induced samples presented here are preceded by a normal state that continues to exhibit a non-linear ρ_{xy} down to just above T_c. That persistent non-linearity, on the other hand, indicates that the three-carrier transport scenario, remains relevant for understanding the electronic properties in the chemically doped normal state leading into the superconducting regime of EFAP.

Simultaneous fits of ρ_{xx} and ρ_{xy} using a three-carrier model, as described in Chapter 3.2 by equations (3.8), (3.9), and (3.10), have been performed. For clarity,

the corresponding equations are repeated here:

$$\rho_{xy}(H) = (\rho_0 H)\,\frac{a + b\,H^2 + c\,H^4}{1 + dH^2 + e_{\text{coeff}}\,H^4}$$

$$\rho_{xx}(H) = \rho_0\,\frac{1 + \alpha\,H^2 + \beta\,H^4}{1 + d\,H^2 + e_{\text{coeff}}\,H^4}$$

$$\rho_0 = \frac{1}{e\,(|n_1\mu_1| + |n_2\mu_2| + |n_3\mu_3|)}, \quad e = 1.602 \times 10^{-19}\ \text{C},$$

$$f_1 = \frac{|n_1\mu_1|}{|n_1\mu_1| + |n_2\mu_2| + |n_3\mu_3|}, \quad f_2 = \frac{|n_2\mu_2|}{|n_1\mu_1| + |n_2\mu_2| + |n_3\mu_3|},$$

$$f_3 = \frac{|n_3\mu_3|}{|n_1\mu_1| + |n_2\mu_2| + |n_3\mu_3|},$$

$$a = f_1\mu_1 + f_2\mu_2 + f_3\mu_3,$$

$$b = f_1\mu_1(\mu_2^2 + \mu_3^2) + f_2\mu_2(\mu_3^2 + \mu_1^2) + f_3\mu_3(\mu_1^2 + \mu_2^2),$$

$$c = (f_1\mu_2\mu_3 + f_2\mu_3\mu_1 + f_3\mu_1\mu_2)\,\mu_1\mu_2\mu_3,$$

$$d = (f_1\mu_2 + f_2\mu_1)^2 + (f_2\mu_3 + f_3\mu_2)^2 + (f_3\mu_1 + f_1\mu_3)^2 + 2\left(f_1f_2\mu_3^2 + f_2f_3\mu_1^2 + f_3f_1\mu_2^2\right)^2,$$

$$e_{\text{coeff}} = (f_1\mu_2\mu_3 + f_2\mu_3\mu_1 + f_3\mu_1\mu_2)^2,$$

$$\alpha = (f_1 + f_2)\,\mu_3^2 + (f_2 + f_3)\,\mu_1^2 + (f_1 + f_3)\,\mu_2^2,$$

$$\beta = f_1\,\mu_2^2\mu_3^2 + f_2\,\mu_1^2\mu_3^2 + f_3\,\mu_1^2\mu_2^2$$

with n_i (μ_i) being the charge carrier densities (carrier mobilities) of band i. These formula can describe the data well at 30 K and 40 K, as shown by the dashed lines in Figure 5.5(a) and (b). The 23 K data can also be described by the model when considering fields above 2.5 T. This cut-off is chosen from where resistivity dropped in the ρ_{xx} data, as can be seen in the inset of (a). The initial values for the fitting procedure were based on results on the pressure-induced parental compound [172]. It should be noted that in a multi-carrier system, multiple parameter sets can yield comparably good fits to the transport data. This degeneracy suggests that while the three-carrier model captures the essential physics of the system, the specific parameter values for carrier densities and mobilities should be treated with caution.

To investigate the interdependence of the model parameters, a sensitivity analysis was performed by calculating the parameter correlation matrix. For example, the results for the 30 K dataset are shown in Table 5.5(d). The analysis reveals several strong correlations. The most prominent is the near-perfect positive correlation ($r = 0.97$) between the second carrier's density (n_2) and its mobility (μ_2). Additionally, the mobility of the first carrier, μ_1, is strongly correlated with both n_2 ($r = 0.80$) and μ_2 ($r = 0.74$), and strongly anti-correlated with μ_3 ($r = -0.79$). These results quantitatively confirm the model's degeneracy and underscore that while the overall fit is robust, the absolute values of individual, strongly correlated parameters carry significant uncertainty. Further constraints, for example from independent measurements, would be needed to uniquely determine the parameter space.

At 23 K, near the superconducting transition, the shape of ρ_{xy} changes significantly, and even shows a sign change at low fields. This behavior somehow resembles that reported in Mn-doped Bi_2Se_3, where a sign change in ρ_{xy} was attributed to a two-component anomalous Hall effect [173]. Given the success of the multi-component model at higher temperatures, it may also apply here. However, the drastic shape change may simply result from the onset of superconductivity itself, as the resistivity is driven toward zero. Measurements at lower temperatures (not shown here) show suppression of the Hall signal, accompanied by large fluctuations, before the system fully transitions into the superconducting state.

5.4 Magnetoresistance Oscillations in Square Rings

Following the successful fabrication of Hall bars via lithography, the research progresses to the study of multiply-connected devices. Ring structures can be designed for investigating the LP effect. As detailed in Chapter 3.5, this experiment provides a direct probe of the magnetic flux quantum and can also reveal signatures of triplet gap symmetries, though such characteristics are not anticipated in the present material system. Using electron-beam lithography, square rings with a mid-to-mid diameter of $L = 800$ nm and a wall width of $w = 200$ nm were patterned onto the same 83 nm, $EuFe_2(As_{1-x}P_x)_2$ ($x \approx 0.20$) film from which the Hall bar results

of the previous chapter were obtained[2]. A schematic of the square ring geometry is shown in Figure 5.6 together with the zero-field $R(T)$ curves after fabrication, showing that the devices show the same characteristic behavior as the Hall bars. Successful measurements of oscillations were only achieved with these thickest devices. The absence of oscillations in devices patterned on thinner films, as well as in those with narrower walls fabricated on the 83 nm film, suggests that the electrical integrity of these more fragile structures was compromised during fabrication.

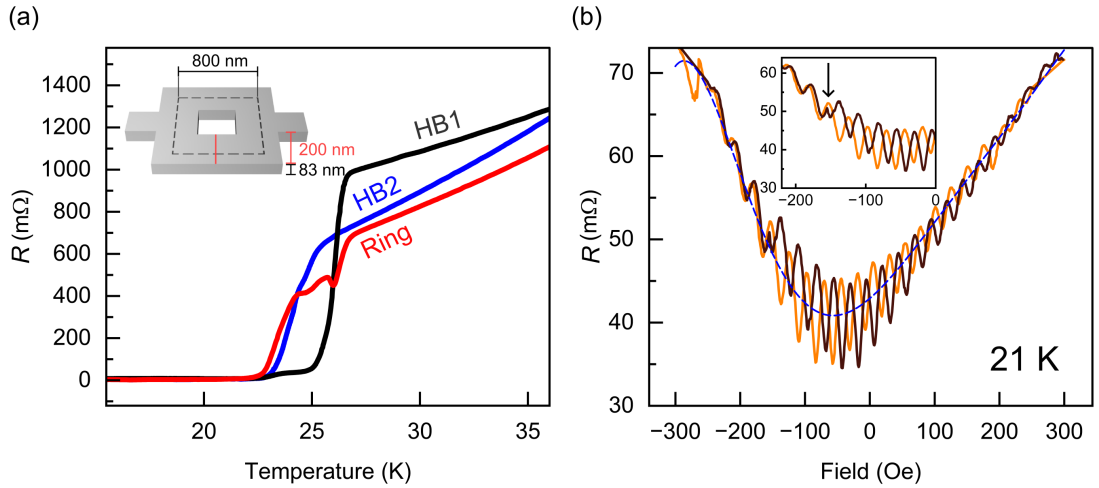


Figure 5.6: (a) Resistance-temperature characteristics of two Hall bars compared with the ring device used in the subsequent measurements. While slight variations in T_c and curve progression are observed, all samples exhibit robust superconductivity. The inset presents a schematic of the ring device with an 800 nm mid-to-mid diameter, 83 nm thickness, and 200 nm wall width. (b) Resistance-field dependence at 21 K, measured with forward and reverse sweeps up to 300 Oe, shown in different colors. The fitted background, represented by the blue dashed line, corresponds to a sixth-order polynomial. The forward and reverse sweeps reveal a π-shift in the oscillations. The inset provides a magnified view of the region where the π-shift occurs, possibly due to vortex entry or exit at this specific point.

The procedure for measurement always followed a zero-field cooling, then the perpendicular field was swept from $0 \rightarrow +300$ Oe $\rightarrow -300$ Oe $\rightarrow +300$ Oe. Clear oscillations were observed within a narrow temperature window of 20.5 K to 23 K. The raw measurement data consists of two primary features: the desired oscillations and a large, asymmetric background. As shown in Figure 5.6(b), this background is largely insensitive to the field sweep direction. To isolate the oscillations, this

[2]Device fabrication was performed by Jiho Yoon, whose support is gratefully acknowledged.

background was fitted to a sixth-order polynomial (shown as a blue dashed line) and subsequently subtracted from the data. To ensure a consistent initial state free of trapped flux, the device was thermally cycled to 50 K before each new temperature measurement. Still, the oscillatory signal occasionally revealed hysteresis between the forward and backward sweeps. These were not smooth shifts but rather abrupt, discrete π-phase jumps, an example of which is seen in Figure 5.6(b). This behavior is an indication, that vortices may be trapped (or trapped vortices may get destroyed) during the measurements [154]. A possible point of vortex entry and trapping is highlighted by an arrow, where a clear deviation between the sweeps sets in.

The expected period of the LP oscillations can be theoretically established. For an s-wave superconductor without triplet pairing, the period is governed by the magnetic flux quantum, $\Phi_0 = h/(2e)$. This fundamental relationship is expected to hold not only for the pure LP effect but also in cases of vortex-assisted transport, which mainly differ in background [174]. In hybrid ferromagnetic-superconductor structures, the changes in flux quantum are expected to be negligible at its conventional value of Φ_0 for standard s-wave pairing [175]. The scenario becomes more complex when considering the possibility of spin-triplet pairing, which can theoretically lead to fractional MR oscillations [152, 154]. Based on the lithographically defined mid-to-mid diameter of $L = 800\,\text{nm}$ and expressions derived in Chapter 3.5, the ideal oscillation period is calculated as:

$$\Delta H_{\text{LP}}^{exp.} = \frac{\Phi_0}{L^2} = 32.2\,\text{Oe}.$$

However, the ring's finite width introduces ambiguity in defining the effective loop area. By assuming that the superconducting current may circulate anywhere across the full wall width, the corresponding range of possible flux areas yields an expected period of $\Delta H_{\text{LP}}^{\text{exp.}} = 25.5\,\text{Oe}$ to $42.2\,\text{Oe}$. This calculated range will serve as the benchmark for the experimental data analysis that follows.

To avoid visual complications from the hysteretic shift between sweep directions, the analysis is restricted to the initial downward field sweep from $300\,\text{mT}$ to $-300\,\text{mT}$. Representative datasets measured at constant temperatures of $20.5\,\text{K}$,

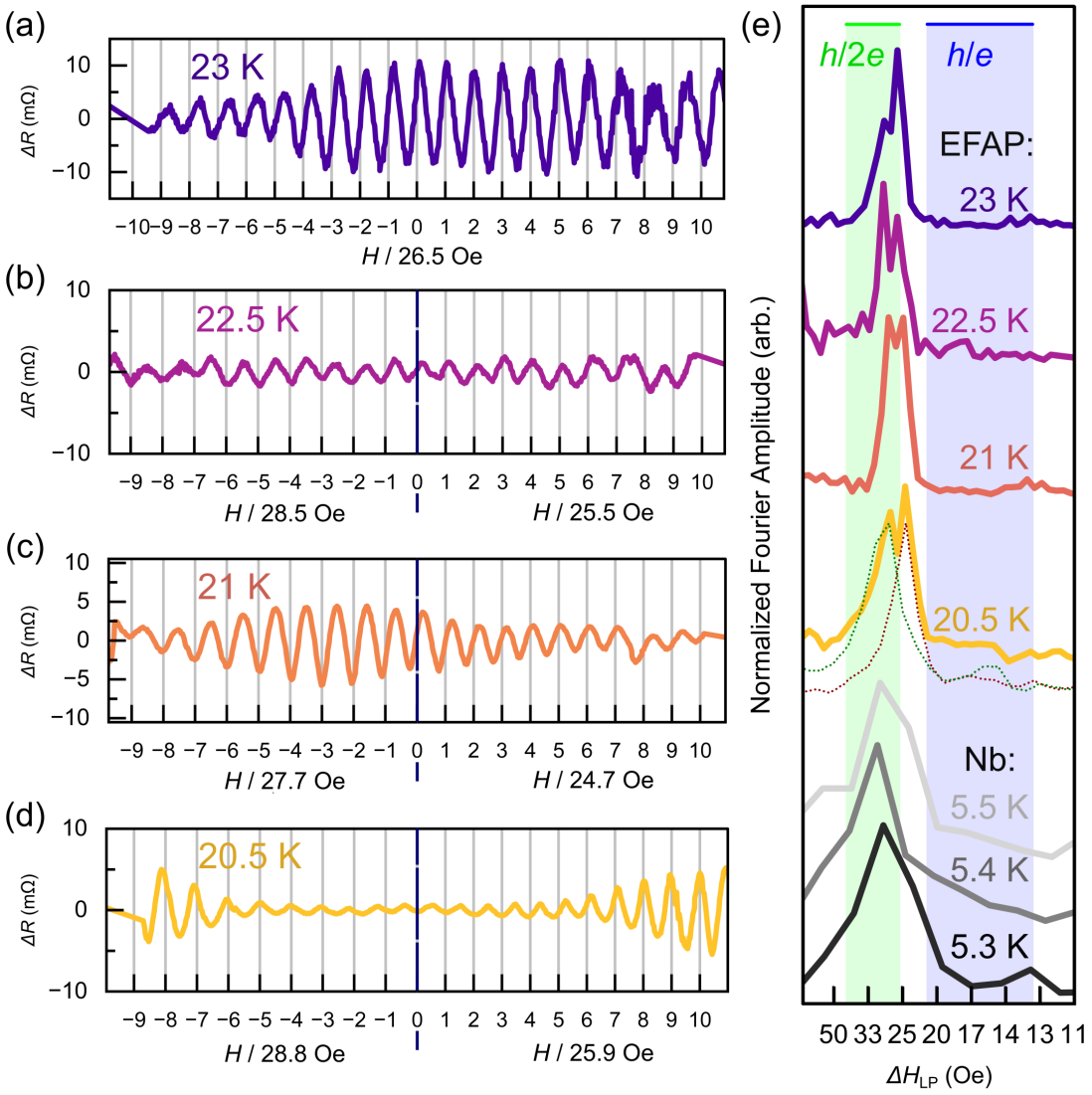


Figure 5.7: (a–d) Resistance difference versus field oscillations, after background subtraction, measured at 23 K, 22.5 K, 21 K, and 20.5 K, respectively, during field sweeps from 300 to −300 Oe. Gridlines are drawn as multiples of the oscillation period. In (b–d), the oscillation period exhibits slight differences between positive and negative fields and the gridlines are adjusted accordingly to provide a clearer visual guide. (e) Corresponding FFT spectrum, revealing a double-peak structure for the EFAP rings. For the 20.5 K data, separate FFTs calculated from only positive (negative) field ranges are shown by green (red) dotted lines. Green and blue bars at the top indicate the range of possible oscillation period values corresponding to a magnetic flux quantum of $h/2e$ or h/e. Gray lines in different shades correspond to reference measurements on Nb rings with the same geometry, taken at 5.3–5.5 K as indicated.

21 K, 22.5 K and 23 K are shown in descending temperature order in Figure 5.7(a–d). The observed resistance oscillations, with amplitudes of approximately 10 mΩ, are larger than expected by the conventional LP model. This can be emphasized by calculating the theoretical values from the equations (3.17) and (3.18) derived in Chapter 3.5. The calculation uses an overestimated maximum coherence length of $\xi_0 = 5$ nm [see Table 5.3(b)], the experimentally obtained slope of the resistive transition $\left(\mathrm{d}R/\mathrm{d}T\right)|_{T_\mathrm{c}} \approx 1.5\,\Omega\,\mathrm{K}^{-1}$ [from Figure 5.6(a)] and ring parameter L. This framework predicts a maximum LP resistance amplitude of:

$$\Delta R_\mathrm{LP} = \left(\tfrac{\mathrm{d}R}{\mathrm{d}T}\right)\Big|_{T_\mathrm{c}} T_\mathrm{c}(0) \left(\frac{\pi\xi_0}{4L}\right)^2 \approx 1\,\mathrm{m}\Omega. \tag{5.5}$$

This value is too small to explain the measurements. In fact, to generate a 10 mΩ amplitude via the standard LP mechanism would require a transition slope of $\approx 16\,\Omega\,\mathrm{K}^{-1}$, which is inconsistent with our measurements. Therefore, the larger oscillation amplitudes, along with the previously discussed π-phase shifts, provide evidence for a vortex-assisted LP effect.

The primary observation from Figures 5.7(a–d) is a variation in the oscillation period. Rather than remaining constant, the period alternates between two discrete values, which differ by roughly 2 Oe to 3 Oe. This behavior appears to be correlated with the sign of the applied magnetic field, with one period predominantly observed for positive fields and the second for negative fields. To highlight this, the grid lines in the figure are defined using a different base period for the positive and negative regimes in (b–d).

Further quantitative evidence for this bimodal period distribution is provided by the Fast Fourier Transform (FFT) shown in Figure 5.7(e). In the figure, the expected period ranges, taking into account current loop ambiguity, corresponding to $h/2e$ and h/e flux quanta are marked by green and blue bars, respectively. The FFT spectrum reveals a double-peak structure, confirming that the resistance oscillations may contain a superposition of two distinct frequency components. To test the hypothesis that these components depend on the magnetic field direction, FFTs of the 20.5 K data were calculated separately for the positive and negative

field ranges. As shown by dotted lines, each range exhibits only one of the two peaks, supporting the field-direction dependence. This temperature is chosen representatively, but similar behavior is found at other temperatures. Furthermore, Figure 5.7(e) contains the FFT result of oscillations obtained from a Nb reference sample of the same geometry at temperatures of 5.3, 5.4 and 5.5 K. As Nb has a lower T_c, the temperature window in which LP oscillations could be observed was shifted to lower temperatures accordingly. The corresponding peaks appear slightly broader due to a reduced number of discernible oscillations. These do not show the double peak feature and are generally shifted towards slightly higher oscillation periods, making them more centered around the $h/2e$ range. This highlights another key anomaly: the obtained oscillation periods of the EFAP rings, while close to the $h/2e$ regime, are systematically shorter than expected but also do not correspond to an h/e period.

All these observed effects remain challenging to interpret. It is quite possible that the interplay between magnetic domain walls and superconductivity, involving intricate phenomena such as domain-Meissner states, vortex–antivortex configurations, or vortex polarons, as briefly discussed at the end of Chapter 1.2.2, influences the LP oscillations in a manner not captured by conventional theory. Consequently, the present work can only conclude this chapter with a call for further theoretical efforts to better understand these effects.

6

Magnetometry Measurements

This chapter presents a study of the magnetic properties of the EFAP thin films, conducted using SQUID magnetometry. The primary objectives are to investigate the ferromagnetic ordering of the Eu^{2+} sublattice and to simultaneously confirm superconducting properties, such as the diamagnetic response and vortex dynamics.

Measurements were performed on as-grown films. For this purpose, the 10 x 10 mm^2 films grown on STO substrates were cleaved into smaller pieces, and the surface area of each sample, as required for the accurate calculation of magnetization, was determined through digital analysis of optical photographs.

The analysis focuses primarily on two representative superconducting samples: Sample A ($x = 0.22, d = 83$ nm) with a metallic $R - T$ behavior and Sample B ($x = 0.22, d = 53$ nm) with a strange-metallic, linear $R - T$ behavior prior to the superconducting transition. Sample A is the same film that was patterned into a Hall bar for the detailed transport studies presented in the previous chapter. As established previously, simple parameters such as P content or film thickness do not uniquely determine the normal-state transport differences. Therefore, these two samples were selected as prototypes of the two distinct regimes (metallic, strange-metallic). A central goal of this investigation is to explore whether this divergence in normal-state resistivity can be correlated with differences in their

magnetic properties, specifically the critical current density J_c calculated from magnetic hysteresis and the nature of the vortex pinning mechanisms.

The chapter is structured as follows. The first section provides an overview of the fundamental magnetic properties, presenting representative magnetization-temperature and magnetization–field data obtained via SQUID magnetometry. The next section introduces the application of the Bean critical state model to extract the critical current density J_c. The resulting J_c values are then analyzed within the framework of different flux pinning models (see Chapter 3.3). Finally, complementary XMCD measurements are presented to provide an element-specific perspective on the magnetic behavior.

Contents

6.1 General Magnetic Properties 94
6.2 Bean Critical-State Analysis and Pinning Models . . . 98
6.3 Probing Element-Specific Magnetism with XMCD . . 100

6.1 General Magnetic Properties

While transport measurements are essential for detecting a zero-resistance state, magnetometry provides the necessary magnetic confirmation of superconductivity by the Meissner response. Indeed, every film that showed a resistive transition also produced a clear diamagnetic signal in SQUID magnetometry, supporting its superconducting nature. Figure 6.1 presents representative magnetization data for Sample B, showing how its magnetic moment responds to changes in temperature and applied field. All measurements were taken after cooling the sample in zero field (ZFC) and measuring in a warming up process.

Panel (a) of Figure 6.1 shows the out-of-plane (OOP) magnetization as a function of temperature in various applied fields. The data reveals a sharp diamagnetic drop around $T_c \approx 22$ K, marking the transition into the superconducting state. It is worth noting that the magnetic T_c is consistently lower than the onset temperature found in the transport data (e.g., 27 K for Sample B). This discrepancy could

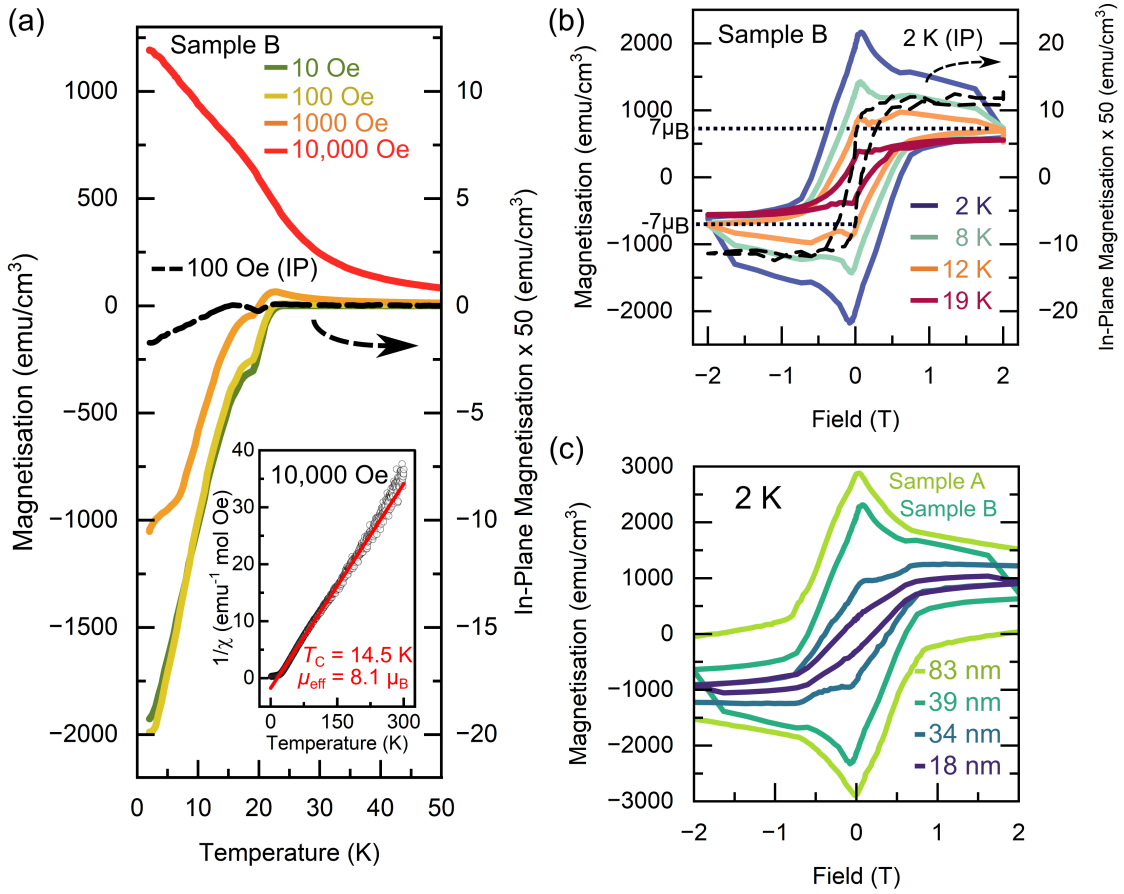


Figure 6.1: (a) OOP $M(T)$ curves for a EFAP film ($x \approx 0.22$, $d = 39\,\text{nm}$) measured on warming in 2, 10, 100, 1000, and 10,000 Oe after zero-field cooling. One IP curve at 100 Oe (right axis) highlights the weaker IP response. (b) OOP M–H loops at 2, 8, 12, 19, and 22 K. An IP loop at 2 K is also shown on a separate axis. (c) Comparison of OOP M–H loops at 2 K for three films of different thicknesses, demonstrating how thickness influences the magnitude and shape of the hysteresis.

simply be due to the different measurement systems, or it might hint at an intrinsic property, such as an inhomogeneous superconducting state where zero-resistance pathways form before the sample can effectively expel magnetic fields. As expected, applying higher fields weakens the diamagnetic signal. A key observation is the complete suppression of the diamagnetic signal at 1 T, a field where the sample is known to be fully superconducting from transport data. This provides evidence for the coexistence of superconductivity and a strong, field-aligned moment from the Eu^{2+} sublattice, which now dominates the total magnetic response. The inset shows the inverse magnetic susceptibility (χ^{-1}) and a linear fit to the Curie-Weiss law. The susceptibility was converted to molar units (emu/(mol Oe)) to allow for the

calculation of the effective magnetic moment in units of μ_{B}. This conversion required an accurate determination of the sample volume, which was derived from the surface area measured via digitized photographs and the unit cell parameters obtained from XRD and TEM (see Chapter 4.2). The linear fit yields an effective magnetic moment of $\mu_{\mathrm{eff}} \approx 8.1\,\mu_B$ and a positive Curie–Weiss temperature of $T_{\mathrm{C}} \approx 14.5\,\mathrm{K}$, confirming the presence of ferromagnetic correlations. The experimental value for μ_{eff} is in excellent agreement with the theoretical moment of $7.94\,\mu_B$ for a free Eu^{2+} ion, with the minor deviation being well within the uncertainty from sample dimension measurements.

However, the precise value of T_{C} is highly sensitive to the subtraction of the magnetic background. This background was measured independently on an annealed substrate of the same dimensions and showed only a negligible paramagnetic upturn at low temperatures, allowing it to be treated as a constant. However, the Curie–Weiss fit is extremely sensitive to the exact value of this constant. To illustrate this point, altering the subtracted background by a mere $5 \times 10^{-7}\,\mathrm{emu}$, an amount 600 times smaller than the film's magnetic moment at low temperature, shifts the calculated T_{C} from 14.5 K to 22 K, even while the inverse susceptibility remains linear and the resulting effective moment retains a physically plausible value of $\mu_{\mathrm{eff}} \approx 7.5\,\mu_{\mathrm{B}}$. For this reason, while the positive sign of T_{C} robustly indicates ferromagnetic correlations for the range of plausible background corrections, the fitting procedure is too delicate to determine its precise value reliably.

In the general magnetization–temperature curves below 1 T a second feature appears at lower temperatures. Around 17 K, a subtle upturn in the magnetic moment is often associated with the ferromagnetic ordering of the Eu^{2+} ions. This result matches well with reports on bulk EFAP. It should be noted that this shoulder has not been observed in all films.

To highlight the film's magnetic anisotropy, panel (a) also includes an in-plane (IP) $M(T)$ curve (black dashed line). The magnetic signal in this orientation is very weak. To make the IP data visible on the plot, its corresponding axis (right) was magnified 100-fold, and the data itself was multiplied by another 50-fold. Even

after this significant scaling, the curve is barely visible, though it faintly shows the same superconducting and ferromagnetic transitions. This strongly suggests the small IP signal may not be an intrinsic property, but a small projection of the dominant OOP signal caused by a minor sample misalignment. For this reason, the rest of the analysis will focus only on the OOP magnetic properties.

Panel (b) of Figure 6.1 presents OOP M–H loops measured at several temperatures below T_c, specifically at $2, 8, 12, 19$, and $22\,\mathrm{K}$. The curves show the superposition of two distinct magnetic signals: a broad hysteresis consistent with the Bean critical state model, which arises from vortex pinning in the type-II superconductor, and a narrower, S-shaped curve typical of a soft ferromagnet, reflecting the field-alignment of the Eu^{2+} moments.

The coercive field from the ferromagnetic component is difficult to resolve, as it is obscured by the much larger superconducting hysteresis. It is, however, expected to be small, consistent with reports on the related compound $EuFe_2P_2$, the non-superconducting, ferromagnetic $x = 1$ end-member of the EFAP series [176]. Normalizing the data using the previously determined sample dimensions reveals a saturation moment of approximately $7\,\mu_B$ per Eu atom. As indicated by the dotted lines in the figure. The strong c-axis anisotropy is confirmed by the IP M–H loop at $2\,\mathrm{K}$ (dashed line), which required the same scaling for visualization as its $M(T)$ counterpart in panel (a).

Panel (c) investigates the influence of film thickness by comparing the M–H loops at 2 K for four EFAP films of similar composition ($x = 0.20-0.22$) but different thicknesses (18, 34, 39, and 83 nm). While the fundamental shape of the hysteresis is consistent, the magnitude of the low-field magnetization increases with film thickness. At high fields, the hysteretic contribution from superconductivity vanishes and all curves converge towards the same saturation moment of the Eu^{2+} ions.

A key observation is that the width of the hysteresis loop, which is proportional to the critical current density J_c, appears to increase with film thickness. A detailed analysis of J_c is presented in the next subchapter, using Sample A as the representative case. The observed trend must be interpreted with caution: it is only

consistent when comparing films grown in the same batch (i.e., fabricated under similar chamber conditions over a short period). Adding single samples from different batches can portray significant outliers; for instance, some thinner films grown more than a year prior have exhibited even larger hysteresis widths than the thickest film shown here. This highlights the long-term variability of the growth conditions.

Taken together, the data in Figure 6.1 underscore the interplay of superconductivity and magnetism in EFAP thin films. By varying the measurement geometry (OOP vs. IP), magnetic field, temperature, and film thickness, these results reveal a complex phase space where robust superconductivity coexists with ferromagnetism of the Eu sublattice. Such findings provide a platform for further investigations as understanding this interplay is might be crucial for the task of enhancing critical temperatures.

6.2 Bean Critical-State Analysis and Pinning Models

The previous section established that the low-temperature M–H loops are dominated by a broad hysteresis, which is a clear signature of vortex pinning. To move beyond this qualitative observation, this section presents a detailed quantitative analysis of the critical current density, J_c.

The central goal is to address a key question from the transport chapter: what is the origin of the distinct normal-state behaviors? To investigate this, the pinning mechanisms of Sample A (metallic) and Sample B (strange-metal) will be determined and compared, seeking a correlation between their vortex dynamics and their normal-state electronic properties.

As described in Chapter 3.3, J_c can be estimated from the width of the magnetization hysteresis loop ΔM, using the following expression derived for a rectangular sample within the Bean critical state model:

$$J_c \approx \frac{20\,\Delta M}{a\left(1-\frac{a}{3b}\right)},$$

where a and b ($a \leq b$) are the in-plane sample dimensions. By applying this analysis to the M–H loops measured at different temperatures, the field and temperature dependencies of the critical current density, $J_c(H)$ and $J_c(T)$, can be obtained. Figure 6.2(a) displays the M–H loops recorded at temperatures between 2 and 24 K for Sample A, while panel (b) shows the corresponding $J_c(H)$ values derived from them. Next, $J_c(T)$ was extracted from panel (b) at fixed magnetic fields

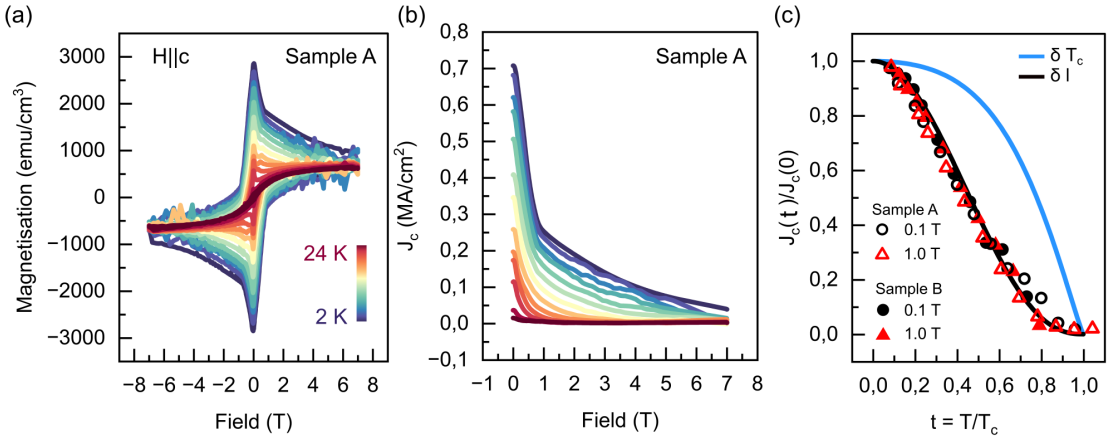


Figure 6.2: (a) OOP M–H loops for Sample A at temperatures ranging from $2 - 24$ K. (b) Critical current densities $J_c(H)$, extracted from hysteresis widths from (a) for the same temperatures. (c) Comparison of $J_c(t = T/T_c)$ curves of Sample A and B at fixed $H = 0.1$ T and $H = 1$ T. Results overlaid with $\delta\ell$ and δT_c pinning model predictions. The closer agreement with $\delta\ell$ suggests that random point-like defects govern vortex pinning in these samples.

of $\mu_0 H = 0.1$ T and $\mu_0 H = 1$ T, representatively. To identify the dominant vortex pinning mechanism, as described in Chapter 3.4 (see equations (3.12) and (3.13)), $J_c(T)/J_c(T = 0)$ was plotted as a function of the reduced temperature $t = T/T_c$. The same analysis was carried out for Sample B, and the results for both samples are shown in Figure 6.2(c), together with the theoretical fits for different pinning models. The experimental data for both samples exhibit excellent agreement with the $\delta\ell$-type pinning model. This model describes pinning by random, point-like defects causing spatial fluctuations in the charge-carrier mean free path. In contrast, the δT_c pinning model, originating from local variations in the superconducting transition temperature, is clearly inconsistent with the experimental data.

This finding implies that the type of pinning mechanism is the same in both samples, dominated by point-like disorder rather than extended defects. This conclusion is supported by STEM studies, which consistently show a low density of layered inhomogeneities across different films and different regions. This result does not contradict the earlier observation that the magnitude of J_c is different between the two samples. The higher critical current in the thicker Sample A may be attributed to a higher density of these point-like pinning sites. Therefore, while the different normal-state transport behaviors of Sample A and Sample B do not originate from a different class of pinning, differences may originate from different concentration of the same underlying point-like defects. At this stage, it must be acknowledged that this endeavor did not succeed in explaining the origin of the differing transport behavior.

6.3 Probing Element-Specific Magnetism with XMCD

To complement the SQUID magnetometry measurements, which probe the total bulk magnetic moment of the sample, XMCD measurements were performed on a 39 nm thick sample capped with ≈ 1 nm of Ta. This element-specific technique allows for the direct and independent probing of the magnetic moments on the Eu and Fe sublattices, unambiguously identifying the origin of the observed magnetic ordering.

The measurements were carried out by Ethan Arnold and Emily Heppell at the I06 Nanoscience Beamline at Diamond Light Source. The analysis based on atomic multiplet theory was performed by Gerrit van der Laan.

Measurements were performed at the Eu $M_{4,5}$ ($\sim 1120 - 1170$ eV) and Fe $L_{2,3}$ ($\sim 700 - 730$ eV) absorption edges. The XAS spectra for negative (μ^-) and positive (μ^+) circular polarization, as well as the corresponding XMCD signal, at the Eu $M_{4,5}$ edges are shown in Figure 6.3(a) for an applied magnetic field of 0.5 T and in panel (b) for 6 T. The measurements were performed at ~ 2 K. The M_5 edge displays two peaks separated by ~ 3 eV, corresponding to Eu^{2+} (lower energy, ~ 1128 eV) and Eu^{3+} (higher energy, ~ 1131 eV). The XMCD signal originates from Eu^{2+}, consistent

with its half-filled $4f$ shell. In contrast, Eu^{3+}, with a $4f^6$ configuration ($^7F_0$) and quantum numbers $S = 3$, $L = 3$, $J = 0$, is non-magnetic and therefore does not contribute to the XMCD signal. A strong XMCD signal is immediately apparent even at a low applied field of 0.5 T, and its intensity continues to increase up to the maximum measured field of 6 T. This provides direct and unambiguous evidence of a large, field-aligned magnetic moment associated with the Eu^{2+} ions. The presence of a strong dichroism even at low field is a signature of ferromagnetic ordering, strongly corroborating the interpretation of the SQUID magnetometry data.

In contrast, the results for the Fe $L_{2,3}$-edges, shown in Figure 6.3(c,d), reveal a different behavior: The XMCD signal is negligible at 0.5 T. Only at the highest applied field of 6 T does a small, but measurable, XMCD signal appear. This observation demonstrates that the Fe sublattice does not possess a significant magnetic order. The possibility that this weak signal originates from oxidized Fe on the sample surface cannot be ruled out. This is particularly relevant given the total electron yield (TEY) detection geometry, which limits the probing depth to approximately $3 - 5$ nm and may be further reduced by the presence of the capping layer.

Atomic multiplet calculations were performed to model the Eu $M_{4,5}$ XAS and XMCD spectra, explicitly including both spin–orbit and electrostatic interactions [177, 178]. The intra-atomic Coulomb and exchange interactions comprise the $3d$–$4f$ and $4f$–$4f$ terms. Wave functions for the initial and final electronic states were calculated in intermediate coupling using Cowan's atomic Hartree–Fock code with relativistic corrections [179, 180], with the Slater integrals scaled to 80% of their Hartree–Fock atomic values (parameters listed in reference [177]). Intrinsic lifetime broadening was modeled with Lorentzian functions having half-widths at half-maximum of $\Gamma = 0.4$ (0.5) eV for the M_5 (M_4) edge, while instrumental resolution was incorporated via Gaussian convolution with $\sigma = 0.3$ eV for XAS and $\sigma = 0.6$ eV for XMCD. Excellent agreement with the experimental Eu $M_{4,5}$ XAS spectra is obtained by assuming a mixed-valence state of 46% Eu^{2+} and 54% Eu^{3+}, as presented in Figure 6.3(e).

The Eu^{3+} component likely arises from surface oxidation of this highly reactive element, an effect enhanced by the aforementioned surface sensitivity of our TEY measurements. A comparison sample with a thicker capping layer exhibits exclusively Eu^{2+} contributions. This dataset is presented in the additional materials Chapter C and is therefore not discussed further here.

Furthermore, a field-dependent measurement at the Eu M_5 peak, shown in Figure 6.3(f), reveals an S-shaped loop. The loop shows no remanence at zero field and a very small coercive field, characteristic of a soft ferromagnet. This indicates that the observed hysteretic behavior in SQUID measurements, were indeed mostly due to type-II Bean model characteristics.

In conclusion, the XMCD results provide a definitive, element-specific confirmation of the magnetic state in EFAP. Magnetism is dominated by the ferromagnetic ordering of the Eu^{2+} sublattice, while the Fe sublattice responsible for superconductivity remains essentially non-magnetic. This confirms the model of two largely decoupled electronic systems coexisting within the material.

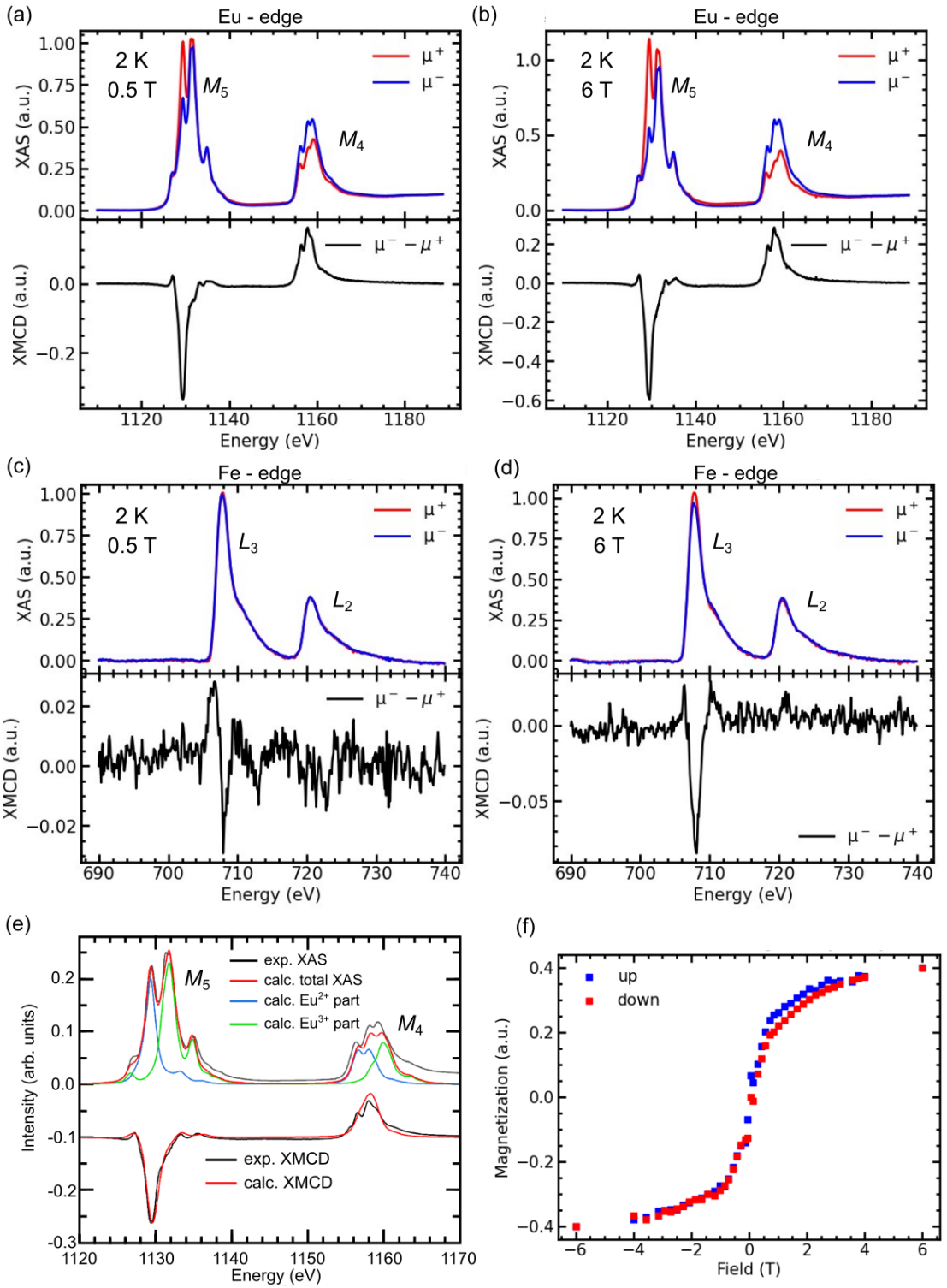


Figure 6.3: XAS and XMCD measurements. Red and blue curves correspond to μ^+ and μ^- polarizations, respectively. (a,b) XAS and XMCD around the Eu M_5 and M_4 edges at 2 K for applied fields of 0.5 T and 6 T, with the XMCD difference shown in black. (c,d) XAS and XMCD spectra ocross the Fe L_3 and L_2 edges at 0.5 T and 6 T, showing a weaker XMCD signal. (e) Comparison of Eu $M_{5,4}$ XAS and XMCD with atomic multiplet calculations (Cowan's Hartree-Fock code with relativistic corrections). (f) Eu M_5 edge TEY-XMCD hysteresis loop up and down sweeps from −6 to 6 T.

7
Summary and Outlook

This thesis focuses on the epitaxial growth of EFA and P-substituted EFAP thin films on STO, LSAT, and LAO substrates, with a primary emphasis on STO. The work detailed in Chapter 4.1 demonstrates the successful fabrication of high-quality epitaxial EFA films via MBE, as confirmed by XRD and STEM analysis. Due to the material's rapid oxidation, a protective Ta capping layer was necessary. The initial growth stages were investigated *in situ* using RT-STM, which revealed a half-layer growth mode. Chapter 4.2 extends the study to EFAP, exploring the influence of growth kinetics over a large number of samples. A plot of growth rate versus substrate temperature suggests the existence of a critical temperature threshold that linearly separates perfect epitaxial growth from defective structures, though this threshold exhibits considerable spread likely attributable to evolving chamber conditions over time. This chapter confirms that increasing P substitution, quantified by EDX, systematically reduces the *c*-axis lattice parameter measured by XRD, consistent with the induction of chemical pressure. Furthermore, STEM-EDX analysis indicates that P primarily substitutes for As and exhibits an interesting concentration modulation from one atomic layer to the next.

The investigation of electronic properties in Chapter 5 reveals that while parent EFA films exhibit a broad resistive peak characteristic of a SDW transition, P-doping in EFAP suppresses this feature and induces superconductivity. The EFAP samples

display a diverse range of normal-state resistivity behaviors, from metallic to strange-metallic and even including a resistive hump prior to the superconducting transition, which could not be correlated with systematic variations in thickness, P-content, or growth quality. A comprehensive phase diagram mapping T_c as a function of thickness and P-content is presented. In-depth analysis of a representative Hall-bar device under magnetic fields shows the expected broadening and suppression of the superconducting transition. The upper critical field, H_{c2}, exhibits a distinct concave curvature near T_c that cannot be explained by conventional WHH theory but is well described by a Gurevich two-band superconducting model. The multiband nature of EFAP is further supported by a non-linear Hall response in the normal state; simultaneous fitting of both ρ_{xx} and ρ_{xy} with a three-carrier model yields physically meaningful parameters. The chapter concludes with the successful observation of the LP effect in microfabricated rings. The LP period in EFAP is slightly shifted relative to conventional superconductors and shows a double-peak structure in its FFT, suggesting two distinct flux-quantization periods.

Chapter 6 details the magnetic properties, with SQUID magnetometry revealing a sharp diamagnetic onset attributable to the Meissner effect. A subtle upturn in the magnetic moment at temperatures below the superconductive transition at low fields signals a ferromagnetic transition, which becomes dominant at higher fields, obscuring the Meissner effect. A Curie–Weiss fit yields $T_C = 14.5$ K and an effective moment of 8 μ_B. M–H loops support the coexistence of two magnetic signals: a broad hysteresis from vortex pinning characteristic of a type-II superconductor, and a narrow, S-shaped curve from the soft ferromagnetic alignment of Eu^{2+} moments. In an attempt to understand the origin of the varied resistivity curves, vortex pinning dynamics were compared between a metallic and a strange-metallic sample. Analysis based on the Bean critical state model indicated that both samples were dominated by $\delta\ell$ pinning, suggesting similar random point-like pinning centers, but failing to explain the differing transport behaviors. Finally, the XMCD measurements support that magnetic signals observed in SQUID at low temperatures mostly originate

from the Eu^{2+} moments, implying that the Fe moments remain non-magnetic in the superconducting state.

The outlook for this work offers numerous possibilities, as is often the case when air-stable (in this case by capping) thin films of high epitaxial quality can be successfully grown. The realization of EFAP thin films opens a versatile platform for both fundamental and applied investigations.

From a fundamental physics perspective, these films enable detailed studies of the superconducting gap structure by spectroscopic techniques such as STM-based STS or ARPES. Mapping the band structure as a function of film thickness, potentially down to single or even half-unit-cell layers, could provide valuable insights into the dimensional crossover and subgap excitations. Moreover, local magnetic imaging techniques, such as MFM or scanning SQUID microscopy, could be employed to visualize vortex configurations or domain structures, continuing and extending similar studies performed on bulk crystals [113–115] toward the two-dimensional limit.

The possibility of growing films on different substrates further enables controlled studies of strain effects. In particular, strain tuning using piezoelectric substrates could provide dynamic control of superconducting and magnetic properties. Preliminary growth experiments on sacrificial $Sr_3Al_2O_6$ layers, which can be dissolved in deionized water to yield freestanding EFAP films, demonstrate the feasibility of strain-free and transferable superconducting layers. Although these freestanding films exhibited changes in their properties over time, further optimization of capping and handling procedures could improve air stability. Such freestanding architectures could then allow the study of strain effects by mechanically deforming or twisting the films, or by transferring them onto substrates of different curvature or lattice mismatch.

In addition to Eu-based compounds, related materials could be investigated to explore the influence of magnetic moment and chemical pressure. For example, partial substitution of Eu with Dy, which has a higher magnetic moment, in

(Eu,Dy)Fe_2As_2 or, if additional chemical pressure is required to stabilize superconductivity, mixed (Eu,Dy)Fe_2(As,P)$_2$ systems could be investigated. Such substitutions may enable enhanced or tunable magnetic interactions while maintaining or inducing superconductivity.

Finally, the combination of EFAP with ferromagnetic layers opens up exciting possibilities for hybrid device architectures [120, 181, 182]. Such EFAP/ferromagnet heterostructures could be employed to study spin-polarized transport, possible triplet Cooper pair generation, and interfacial phenomena between ferromagnetic superconductors and conventional ferromagnets. These directions highlight the broad potential of this material platform for advancing our understanding of the interplay between magnetism, superconductivity, and strain in complex quantum materials.

A

Additional Material for Chapter 4

STEM–EDX Clarifications

As promised in Chapter 4.2, this appendix addresses questions related to the STEM–EDX results presented in Figure 4.5.

First, the statement that P substitutes As in a regular, alternating fashion, one layer richer in P, the next poorer, may have seemed strong, particularly given the local nature of STEM measurements. One might therefore question the reproducibility of this observation. In fact, this behavior was observed consistently across multiple regions of the same sample. Moreover, the figure shown here corresponds to a *different* film, with a lower overall P concentration. This sample is superconducting, in contrast to the one discussed in Chapter 4.2, which contained a higher P content and was selected primarily because its stronger EDX contrast made the modulation easier to visualize.

The data presented in Figure A.1(a) show the As and P EDX maps and corresponding averaged line profiles along the growth direction for a sample with $\mathrm{P}/(\mathrm{As}+\mathrm{P}) = 0.22$, i.e., within the composition range where superconductivity occurs (and indeed confirmed for this film). As before, the EDX maps were denoised using a Wiener filter. In the present case, a mild additional smoothing was applied to the line profiles, this did not affect the overall features. The

periodic modulation of P concentration is again apparent. In this case, it even seems that one intermediate layer may be nearly P-free, although this cannot be stated definitively. As before, wherever the P signal peaks in the line scan, the As intensity is correspondingly reduced.

A second question concerns the appearance of Fe atoms as "lines" in Figure 4.5. This might suggest extensive lateral spreading of Fe, but this is more likely a geometric imaging effect. As noted briefly before, in a (100) cross-section, the in-plane spacing of Fe atoms is small, leading to their appearance as continuous lines in the STEM image. To clarify this, a (110) cross-section was prepared. As can be seen in Figure A.1(b), in this orientation the Fe atoms become distinguishable individually, whereas the Eu atoms now appear as lines. This behavior follows directly from the crystal geometry: along the (100) direction, the resolved Eu–Eu spacing corresponds to a, but when rotated to (110) it becomes $a/\sqrt{2}$ and is no longer resolvable. Conversely, for the Fe sublattice, the apparent spacing increases from a^* in (100) to $a^*\sqrt{2}$ in (110), making the Fe atoms individually resolvable. The accompanying schematic illustrates this geometric effect.

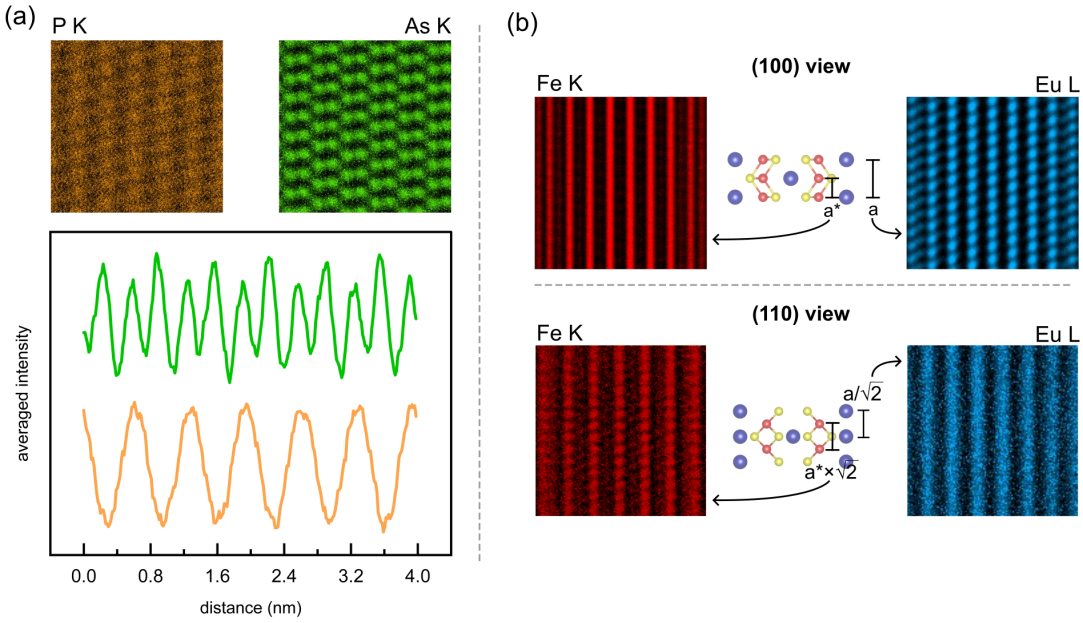


Figure A.1: (a) EDX elemental maps of As and P, and corresponding averaged line profiles along the growth direction for a EFAP film with $P/(As + P) = 0.22$. A clear modulation of P concentration is visible, consistent with alternating P-rich and P-poor layers, confirming that the substitutional pattern is reproducible across samples.
(b) STEM images and schematic atomic models comparing (100) and (110) cross-sections. In the (100) view, Fe atoms appear as continuous lines due to their small in-plane spacing, while in the (110) orientation the Fe atoms become individually resolvable and the Eu rows appear line-like, as explained by the geometric projection.

B

Additional Material for Chapter 5

Low-temperature STM/STS Measurements

As discussed in Chapter 5.1, Figure 5.1 shows red crosses for samples below 8 nm thickness, indicating that superconductivity could not be reliably detected. This does not necessarily imply the absence of superconductivity; rather, measurements of such thin films in SQUID or transport setups were not feasible. To gain further insight, a 4 nm non-capped film was transferred using a vacuum suitcase to a low-temperature STM.[1] Compared to the room-temperature STM connected to the MBE UHV chamber (Chapter 4.1, Figure 4.2), this instrument can operate at temperatures down to 600 mK and offers higher spatial resolution, making it suitable for probing both the superconducting gap and surface features.

STS measurements with a setpoint current of 500 pA revealed a gap even in the 4 nm film. Upon application of a magnetic field, the gap partially closed up to 3 T, while higher fields up to 6 T did not further modify the gap. Spatial mapping of the LDOS was not possible due to the surface reactivity and rapid changes during scans. On a slightly thicker film ($\sim$ 6 nm), the same behavior was observed, and LDOS maps could be recorded briefly before degradation. At sample biases of +5 meV and -40 meV, periodic features were detected: approximately $5.8 - 5.9$ Å in the first

[1]The STM measurements were carried out by Felix Küster and Jenny Davern, whose contributions are gratefully acknowledged.

case and longer-scale modulations of 16.9 Å and 18 Å in the second. These values do not correspond to simple multiples of the in-plane lattice spacing ($\sim$ 3.9 Å).

Although the dataset is limited, these observations may indicate subtle electronic ordering or nematicity in the films. The measured periodicities suggest a modulation of electronic or structural origin beyond the basic crystal lattice. Nematicity is not unexpected in Fe-based superconductors, as briefly touched on in Chapter 1.1.2.

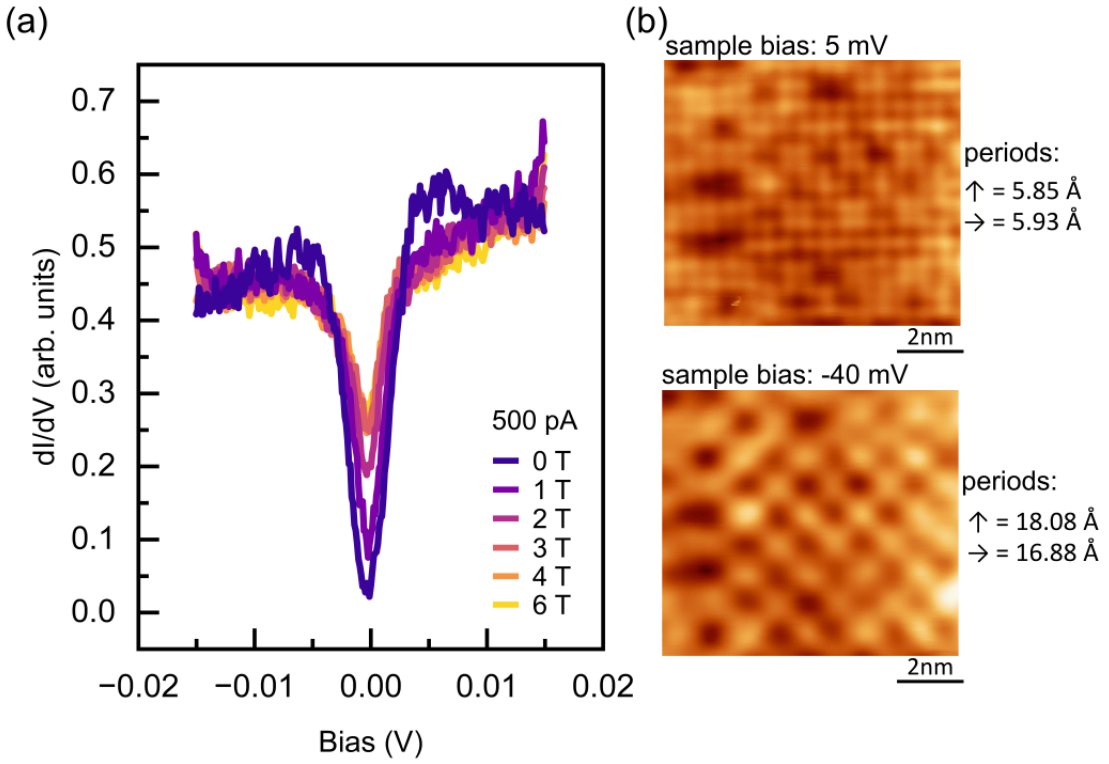


Figure B.1: (a) STS measurement of the 4 nm EFAP film at 2 K, showing a superconducting gap. (b) Local density of states (LDOS) maps of a slightly thicker (6 nm) film, obtained at sample biases of 5 meV and -40 meV, highlighting the observed periodic modulations. LODS slightly enhanced by FFT filtering.

C

Additional Material for Chapter 6

XMCD Results on a Sample with Thicker Capping

As discussed in the XAS results of Chapter 6.3, the M_5 edge exhibited contributions from mixed Eu^{2+}/Eu^{3+} valence states, which were attributed to possible surface oxidation, particularly given the surface sensitivity of the TEY mode. Here, XAS spectra for left- and right-circularly polarized light (μ^+ and μ^-) and the corresponding XMCD signal are presented for a thicker film (83 nm) with P/(As+P)= 22%, featuring a four-times thicker Ta capping layer (4 nm in total). The spectra reveal a pronounced suppression of the higher-energy M_5 feature (previously observed near 1131 eV), indicating that the Eu^{3+} contribution seen in the earlier measurement likely originated from surface oxidation rather than an intrinsic valence mixing within the material.

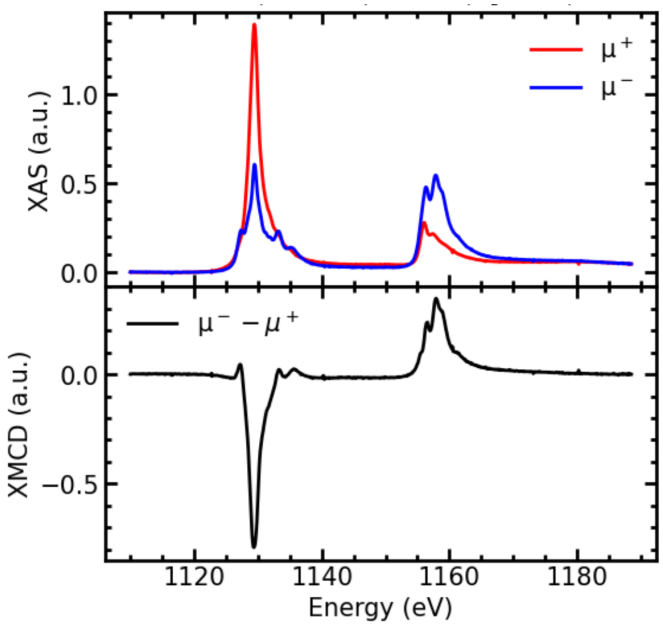


Figure C.1: XAS and XMCD spectra of a 83 nm EFAP film with a 4 nm Ta capping layer. The thicker capping suppresses the higher-energy M_5 feature associated with Eu^{3+}, supporting the interpretation that the mixed-valence signal in thinner-capped samples arises from surface oxidation rather than intrinsic effects.

References

[1] J. G. Bednorz and K. A. Müller, "Possible high T_c superconductivity in the Ba-La-Cu-O system", Zeitschrift für Physik B Condensed Matter **64**, 189–193 (1986).

[2] J. G. Bednorz and K. A. Müller, "Perovskite-type oxides—The new approach to high-T_c superconductivity", Rev. Mod. Phys. **60**, 585 (1988).

[3] B. Keimer et al., "From quantum matter to high-temperature superconductivity in copper oxides", Nature **518**, 179–186 (2015).

[4] Q. Si and N. E. Hussey, "Iron-based superconductors: Teenage, complex, challenging", Physics Today **76**, 34–40 (2023).

[5] D. C. Johnston, "The puzzle of high temperature superconductivity in layered iron pnictides and chalcogenides", Adv. Phys. **59**, 803–1061 (2010).

[6] G. R. Stewart, "Superconductivity in iron compounds", Rev. Mod. Phys. **83**, 1589–1652 (2011).

[7] Y. Kamihara et al., "Iron-based layered superconductor La[$O_{1-x}F_x$]FeAs (x=0.05–0.12) with T_c = 26 K", J. Am. Chem. Soc. **130**, 3296–3297 (2008).

[8] X. H. Chen et al., "Superconductivity at 43 K in SmFeAs$O_{1-x}F_x$", Nature **453**, 761–762 (2008).

[9] Z.-A. Ren et al., "Superconductivity at 55 K in Iron-Based F-Doped Layered Quaternary Compound Sm[$O_{1-x}F_x$]FeAs", Chin. Phys. Lett. **25**, 2215 (2008).

[10] M. Rotter, M. Tegel, and D. Johrendt, "Superconductivity at 38 K in the Iron Arsenide ($Ba_{1-x}K_x$)Fe_2As_2", Phys. Rev. Lett. **101**, 107006 (2008).

[11] P. W. Anderson, "The resonating valence bond state in La_2CuO_4 and superconductivity", Science **235**, 1196–1198 (1987).

[12] Q.-Y. Wang et al., "Interface-Induced High-Temperature Superconductivity in Single Unit-Cell FeSe Films on $SrTiO_3$", Chin. Phys. Lett. **29**, 037402 (2012).

[13] J.-F. Ge et al., "Superconductivity above 100 K in single-layer FeSe films on doped $SrTiO_3$", Nat. Mater. **14**, 285–289 (2015).

[14] T. Katase et al., "Advantageous grain boundaries in iron pnictide superconductors", Nat. Commun. **2**, 409 (2011).

[15] T. Katase et al., "Biaxially textured cobalt-doped $BaFe_2As_2$ films with high critical current density over 1 MA/cm^2 on MgO-buffered metal-tape flexible substrates", Appl. Phys. Lett. **98**, 242510 (2011).

[16] S. Zapf and M. Dressel, "Europium-based iron pnictides: a unique laboratory for magnetism, superconductivity and structural effects", Rep. Prog. Phys. **80**, 016501 (2017).

[17] H. Ghosh and S. Sen, "Iron based superconductors: A brief overview", arXiv preprint arXiv:1408.3244 (2014).

[18] J. Zhao et al., "Structural and magnetic phase diagram of $CeFeAsO_{1-x}F_x$ and its relation to high-temperature superconductivity", Nat. Mater. **7**, 953–959 (2008).

[19] C. de la Cruz et al., "Magnetic Order Close to Superconductivity in the Iron-Based Layered $LaO_{1-x}F_xFeAs$ Systems", Nature **453**, 899–902 (2008).

[20] C. R. Rotundu et al., "Phase diagram of the $PrFeAsO_{1-x}F_x$ superconductor", Phys. Rev. B **80**, 144517 (2009).

[21] A. E. Böhmer et al., "Nematicity and nematic fluctuations in iron-based superconductors", Nat. Phys. **18**, 1412–1419 (2022).

[22] R. M. Fernandes, A. V. Chubukov, and J. Schmalian, "What drives nematic order in iron-based superconductors?", Nat. Phys. **10**, 97–104 (2014).

[23] H. Luetkens et al., "Field and temperature dependence of the superfluid density in $LaFeAsO_{1-x}F_x$ superconductors: A muon spin relaxation study", Phys. Rev. Lett. **101**, 097009 (2008).

[24] H. Okada et al., "Superconductivity under High Pressure in LaFeAsO", J. Phys. Soc. Jpn. **77**, 113712 (2008).

[25] H. Hiramatsu et al., "Heteroepitaxial growth and optoelectronic properties of layered iron oxyarsenide, LaFeAsO", Appl. Phys. Lett. **93**, 162504 (2008).

[26] T. Kawaguchi et al., "In situ growth of superconducting NdFeAs(O,F) thin films by molecular beam epitaxy", Appl. Phys. Lett. **97**, 042509 (2010).

[27] S. Ueda et al., "High-T_c and high-J_c SmFeAs(O,F) films on fluoride substrates grown by molecular beam epitaxy", Appl. Phys. Lett. **99**, 232505 (2011).

[28] S. Haindl et al., "In-situ growth of superconducting $SmO_{1-x}F_xFeAs$ thin films by pulsed laser deposition", Sci. Rep. **6**, 35797 (2016).

[29] F.-C. Hsu et al., "Superconductivity in the PbO-type structure α-FeSe", Proc. Natl. Acad. Sci. USA **105**, 14262–14264 (2008).

[30] S. Medvedev et al., "Electronic and magnetic phase diagram of β-$Fe_{1.01}Se$ with superconductivity at 36.7 K under pressure", Nat. Mater. **8**, 630–633 (2009).

[31] M. H. Fang et al., "Superconductivity close to magnetic instability in $Fe(Se_{1-x}Te_x)_{0.82}$", Phys. Rev. B **78**, 224503 (2008).

[32] W. Si et al., "Enhanced superconducting transition temperature in $FeSe_{0.5}Te_{0.5}$ thin films", Appl. Phys. Lett. **95**, 052504 (2009).

[33] Q.-K. Xue et al., "High-temperature superconducting film", Patent US9461233B2 (Oct. 2016).

[34] Q. Wang et al., "Magnetic ground state of FeSe", Nat. Commun. **7**, 12182 (2016).

[35] S. Tan et al., "Interface-induced superconductivity and strain-dependent spin density waves in FeSe/$SrTiO_3$ thin films", Nat. Mater. **12**, 634–640 (2013).

[36] J. P. Sun et al., "Dome-shaped magnetic order competing with high-temperature superconductivity at high pressures in FeSe", Nat. Commun. **7**, 12146 (2016).

[37] J. H. Tapp et al., "LiFeAs: An intrinsic FeAs-based superconductor with $T_c = 18$ K", Phys. Rev. B **78**, 060505(R) (2008).

[38] S. V. Borisenko et al., "Superconductivity without Nesting in LiFeAs", Phys. Rev. Lett. **105**, 067002 (2010).

[39] P. Jeglič et al., "^{75}As nuclear magnetic resonance study of antiferromagnetic fluctuations in the normal state of LiFeAs", Phys. Rev. B **81**, 140511(R) (2010).

[40] S. Li et al., "Structural and magnetic phase transitions in $Na_{1-\delta}FeAs$", Phys. Rev. B **80**, 020504(R) (2009).

[41] C. W. Chu et al., "The synthesis and characterization of LiFeAs and NaFeAs", Physica C: Superconductivity **469**, 326–331 (2009).

[42] D. R. Parker et al., "Control of the competition between a magnetic phase and a superconducting phase in cobalt-doped and nickel-doped NaFeAs using electron count", Phys. Rev. Lett. **104**, 057007 (2010).

[43] A. F. Wang et al., "Phase diagram and calorimetric properties of $NaFe_{1-x}Co_xAs$", Phys. Rev. B **85**, 224521 (2012).

[44] Q. Huang et al., "Neutron-diffraction measurements of magnetic rrder and a structural transition in the parent BaFe2As2 compound of FeAs-based high-temperature superconductors", Phys.Rev. Lett. **101**, 257003 (2008).

[45] Y. Xiao et al., "Magnetic structure of $EuFe_2As_2$ determined by single-crystal neutron diffraction", Phys. Rev. B **80**, 174424 (2009).

[46] M. Rotter et al., "Superconductivity and Crystal Structures of $(Ba_{1-x}K_x)Fe_2As_2$ (x=0–1)", Angewandte Chemie International Edition **47**, 7949–7952 (2008).

[47] Z. Bukowski et al., "Bulk superconductivity at 2.6 K in undoped $RbFe_2As_2$", Phys. C: Supercond. Appl. **470**, 328–329 (2010).

[48] K. Sasmal et al., "Superconducting Fe-Based Compounds $(A_{1-x}Sr_x)Fe_2As_2$ with A = K and Cs with Transition Temperatures up to 37 K", Phys. Rev. Lett. **101**, 107007 (2008).

[49] N. Ni et al., "Effects of Co substitution on thermodynamic and transport properties and anisotropic H_{c2} in $Ba(Fe_{1-x}Co_x)_2As_2$ single crystals", Phys. Rev. B **78**, 214515 (2008).

[50] S. Jiang et al., "Superconductivity up to 30 K in the vicinity of the quantum critical point in $BaFe_2(As_{1-x}P_x)_2$", J. Phys. Condens. Matter **21**, 382203 (2009).

[51] T. Yamazaki et al., "Appearance of pressure-induced superconductivity in $BaFe_2As_2$ under hydrostatic conditions and its extremely high sensitivity to uniaxial stress", Phys. Rev. B **81**, 224511 (2010).

[52] H. Sato et al., "Enhanced critical-current in P-doped $BaFe_2As_2$ thin films on metal substrates arising from poorly aligned grain boundaries", Sci. Rep. **6**, 36828 (2016).

[53] F. Kurth et al., "Unusually high critical current of clean P-doped $BaFe_2As_2$ single crystalline thin film", Appl. Phys. Lett. **106**, 072602 (2015).

[54] T. Hatano et al., "High tolerance of the superconducting current to large grain boundary angles in potassium-doped $BaFe_2As_2$", NPG Asia Mater. **16**, 41 (2024).

[55] E. Wiesenmayer et al., "Microscopic coexistence of superconductivity and magnetism in $Ba_{1-x}K_xFe_2As_2$", Phys. Rev. Lett. **107**, 237001 (2011).

[56] L. Ma et al., "Microscopic coexistence of superconductivity and antiferromagnetism in underdoped $Ba(Fe_{1-x}Ru_x)_2As_2$", Phys. Rev. Lett. **109**, 197002 (2012).

[57] P. Cai et al., "Visualizing the microscopic coexistence of spin density wave and superconductivity in underdoped $NaFe_{1-x}Co_xAs$", Nat. Commun **4**, 1596 (2013).

[58] J. Munevar et al., "Magnetism in superconducting $EuFe_2As_{1.4}P_{0.6}$ single crystals studied by local probes", Solid State Commun. **187**, 18–22 (2014).

[59] D. J. Singh and M.-H. Du, "Density functional study of $LaFeAsO_{1-x}F_x$: A low carrier density superconductor near itinerant magnetism", Phys. Rev. Lett. **100**, 237003 (2008).

[60] D. H. Lu et al., "Electronic structure of the iron-based superconductor LaOFeP", Nature **455**, 81–84 (2008).

[61] I. I. Mazin et al., "Unconventional superconductivity with a sign reversal in the order parameter of $LaFeAsO_{1-x}F_x$", Phys. Rev. Lett. **101**, 057003 (2008).

[62] J. Paglione and R. L. Greene, "High-temperature superconductivity in iron-based materials", Nat. Phys. **6**, 645–658 (2010).

[63] X. Chen et al., "Iron-based high transition temperature superconductors", Natl. Sci. Rev. **1**, 371–395 (2014).

[64] Y. Zhang et al., "Nodal superconducting-gap structure in ferropnictide superconductor $BaFe_2(As_{0.7}P_{0.3})_2$", Nat. Phys. **8**, 371–375 (2012).

[65] K. Kuroki et al., "Unconventional Pairing Originating from the Disconnected Fermi Surfaces of Superconducting $LaFeAsO_{1-x}F_x$", Phys. Rev. Lett. **101**, 087004 (2008).

[66] S. Graser et al., "Near-degeneracy of several pairing channels in multiorbital models for the Fe pnictides", New J. Phys. **11**, 025016 (2009).

[67] D. J. Scalapino, "A common thread: The pairing interaction for unconventional superconductors", Rev. Mod. Phys. **84**, 1383 (2012).

[68] M. Tinkham, *Introduction to Superconductivity*, 2nd ed. (McGraw-Hill, New York, 1996).

[69] K. Terashima et al., "Fermi surface nesting induced strong pairing in iron-based superconductors", Proc. Natl. Acad. Sci. U.S.A. **106**, 7330–7333 (2009).

[70] T. Hajiri et al., "Three-dimensional electronic structure and interband nesting in the stoichiometric superconductor LiFeAs", Phys. Rev. B **85**, 094509 (2012).

[71] S. Chi et al., "Imaging the real space structure of the spin fluctuations in an iron-based superconductor", Nat. Commun. **8**, 15996 (2017).

[72] H. Ding et al., "Observation of Fermi-surface–dependent nodeless superconducting gaps in $Ba_{0.6}K_{0.4}Fe_2As_2$", Europhys. Lett. **83**, 47001 (2008).

[73] A. D. Christianson et al., "Unconventional Superconductivity in $Ba_{0.6}K_{0.4}Fe_2As_2$ from Inelastic Neutron Scattering", Nature **456**, 930–932 (2008).

[74] R. Marchand and W. Jeitschko, "Ternary lanthanoid-transition metal pnictides with $ThCr_2Si_2$-type structure", J. Solid State Chem. **24**, 351–357 (1978).

[75] Z. Ren et al., "Antiferromagnetic transition in $EuFe_2As_2$: A possible parent compound for superconductors", Phys. Rev. B **78**, 052501 (2008).

[76] H. Raffius et al., "Magnetic properties of ternary lanthanoid transition metal arsenides studied by Mössbauer and susceptibility measurements", J. Phys. Chem. Solids **54**, 135–144 (1993).

[77] S. Jiang et al., "Metamagnetic transition in EuFe2As2 single crystals", New J. Phys. **11**, 025007 (2009).

[78] J. Herrero-Martín et al., "Magnetic structure of EuFe2As2 as determined by resonant X-ray scattering", Phys. Rev. B **80**, 134411 (2009).

[79] Y. Xiao et al., "Field-induced spin reorientation and giant spin-lattice coupling in $EuFe_2As_2$", Phys. Rev. B **81**, 220406(R) (2010).

[80] C. F. Miclea et al., "Evidence for a reentrant superconducting state in $EuFe_2As_2$ under pressure", Phys. Rev. B **79**, 212509 (2009).

[81] T. Terashima et al., "$EuFe_2As_2$ under High Pressure: An Antiferromagnetic Bulk Superconductor", J. Phys. Soc. Jpn. **78**, 083701 (2009).

[82] N. Kurita et al., "Phase diagram of pressure-induced superconductivity in EuFe2As2 probed by high-pressure resistivity up to 3.2 GPa", Phys. Rev. B **83**, 214513 (2011).

[83] K. Matsubayashi et al., "Pressure-induced changes in the magnetic and valence state of $EuFe_2As_2$", Phys. Rev. B **84**, 024502 (2011).

[84] S. Ikeda et al., "New antiferromagnetic order with pressure-induced superconductivity in $EuFe_2As_2$", Phys. Rev. B **98**, 100502(R) (2018).

[85] A. Błachowski et al., "Interplay between magnetism and superconductivity in $EuFe_{2-x}Co_xAs_2$ studied by ^{57}Fe and ^{151}Eu Mössbauer spectroscopy", Phys. Rev. B **84**, 174503 (2011).

[86] W. T. Jin et al., "Magnetic structure of superconducting $Eu(Fe_{0.82}Co_{0.18})_2As_2$ as revealed by single-crystal neutron diffraction", Phys. Rev. B **88**, 214516 (2013).

[87] W. T. Jin et al., "Phase diagram of Eu magnetic ordering in Sn-flux-grown $Eu(Fe_{1-x}Co_x)_2As_2$ single crystals", Phys. Rev. B **94**, 184513 (2016).

[88] W.-H. Jiao et al., "Anomalous critical fields and the absence of Meissner state in $Eu(Fe_{0.88}Ir_{0.12})_2As_2$ crystals", New J. Phys. **15**, 113002 (2013).

[89] U. B. Paramanik et al., "Reentrant superconductivity in $Eu(Fe_{1-x}Ir_x)_2As_2$", J. Phys.: Condens. Matter **25**, 265701 (2013).

[90] U. B. Paramanik et al., "Magnetic and superconducting properties of Ir-doped $EuFe_2As_2$", Supercond. Sci. Technol. **27**, 075012 (2014).

[91] W. T. Jin et al., "Magnetic ground state of superconducting $Eu(Fe_{0.88}Ir_{0.12})_2As_2$: A combined neutron diffraction and first-principles calculation study", Phys. Rev. B **91**, 064506 (2015).

[92] W.-H. Jiao et al., "Anisotropic superconductivity in $Eu(Fe_{0.75}Ru_{0.25})_2As_2$ ferromagnetic superconductor", EPL **95**, 67007 (2011).

[93] W.-H. Jiao et al., "Evolution of superconductivity and ferromagnetism in $Eu(Fe_{1-x}Ru_x)_2As_2$", J. Phys.: Conf. Ser. **400**, 022038 (2012).

[94] Z. Zhou et al., "Universal critical behavior in the ferromagnetic superconductor $Eu(Fe_{0.75}Ru_{0.25})_2As_2$", Phys. Rev. B **100**, 060406(R) (2019).

[95] Z. Ren et al., "Superconductivity induced by phosphorus doping and its coexistence with ferromagnetism in $EuFe_2(As_{0.7}P_{0.3})_2$", Phys. Rev. Lett. **102**, 137002 (2009).

[96] S. Zapf et al., "Varying Eu^{2+} magnetic order by chemical pressure in $EuFe_2(As_{1-x}P_x)_2$", Phys. Rev. B **84**, 140503(R) (2011).

[97] S. Zapf et al., "Reentrant Spin Glass and Superconductivity in $EuFe_2(As_{1-x}P_x)_2$", Phys. Rev. Lett. **110**, 237002 (2013).

[98] S. Nandi et al., "Coexistence of superconductivity and ferromagnetism in P-doped $EuFe_2As_2$", Phys. Rev. B **89**, 014512 (2014).

[99] Anupam et al., "Superconductivity and magnetism in K-doped $EuFe_2As_2$", J. Phys.: Condens. Matter **21**, 265701 (2009).

[100] L. M. Tran et al., "Magnetic phase diagram of Ca-substituted $EuFe_2As_2$", Phys. Rev. B **98**, 104412 (2018).

[101] H. S. Jeevan et al., "Interplay of antiferromagnetism, ferromagnetism, and superconductivity in $EuFe_2(As_{1-x}P_x)_2$ single crystals", Phys. Rev. B **83**, 054511 (2011).

[102] D. Wu et al., "Optical investigations of chemically pressurized $EuFe_2(As_{1-x}P_x)_2$: An *s*-wave superconductor with strong interband interactions", Phys. Rev. B **83**, 100503(R) (2011).

[103] S. Thirupathaiah et al., "Dissimilarities between the electronic structure of chemically doped and chemically pressurized iron pnictides from an angle-resolved photoemission spectroscopy study", Phys. Rev. B **84**, 014531 (2011).

[104] J. Maiwald, H. S. Jeevan, and P. Gegenwart, "Signatures of quantum criticality in hole-doped and chemically pressurized $EuFe_2As_2$ single crystals", Phys. Rev. B **85**, 024511 (2012).

[105] H.-A. K. von Nidda et al., "Electron spin resonance in Eu-based iron pnictides", Phys. Rev. B **86**, 094411 (2012).

[106] Y. Tokiwa et al., "Unique phase diagram with narrow superconducting dome in $EuFe_2(As_{1-x}P_x)_2$ due to Eu^{2+} local magnetic moments", Phys. Rev. B **86**, 220505(R) (2012).

[107] S. Jiang et al., "Thermopower as a sensitive probe of electronic nematicity in iron pnictides", Phys. Rev. Lett. **110**, 067001 (2013).

[108] I. Nowik et al., "Coexistence of ferromagnetism and superconductivity: magnetization and Mössbauer studies of $EuFe_2(As_{1-x}P_x)_2$", J. Phys.: Condens. Matter **23**, 065701 (2011).

[109] A. Ahmed et al., "Competing ferromagnetism and superconductivity on FeAs layers in $EuFe_2(As_0.73P_0.27)_2$", Phys. Rev. Lett. **105**, 207003 (2010).

[110] G. Cao et al., "Superconductivity and ferromagnetism in $EuFe_2(As_{1-x}P_x)_2$", J. Phys.: Condens. Matter **23**, 464204 (2011).

[111] Z. Guguchia et al., "Muon-spin rotation and magnetization studies of chemical and hydrostatic pressure effects in $EuFe_2(As_{1x}P_x)_2$", J. Supercond. Nov. Magn. **26**, 285–295 (2013).

[112] A. Akbari, I. Eremin, and P. Thalmeier, "RKKY interaction in the spin-density-wave phase of iron-based superconductors", Phys. Rev. B **84**, 134513 (2011).

[113] V. S. Stolyarov et al., "Domain Meissner state and spontaneous vortex-antivortex generation in the ferromagnetic superconductor $EuFe_2(As_{0.79}P_{0.21})_2$", Sci. Adv. **4**, eaat1061 (2018).

[114] W. Jin et al., "Bulk domain Meissner state in the ferromagnetic superconductor $EuFe_2(As_{0.8}P_{0.2})_2$: Consequence of compromise between ferromagnetism and superconductivity", Phys. Rev. B **105**, L180504 (2022).

[115] J. A. Wilcox et al., "Magnetically controlled vortex dynamics in a ferromagnetic superconductor", Commun. Mater. **6**, 108 (2025).

[116] K. Iida, J. Hänisch, and C. Tarantini, "Fe-based superconducting thin films on metallic substrates: Growth, characteristics, and relevant properties", Appl. Phys. Rev. **5**, 031304 (2018).

[117] K. Iida et al., "Recent progress on epitaxial growth of Fe-based superconducting thin films", Supercond. Sci. Technol. **36**, 063001 (2023).

[118] K. Iida, "Status of iron based superconductors: characteristics and relevant properties for applications", arXiv preprint arXiv:2502.17063 (2025).

[119] J. Engelmann et al., "Strain induced superconductivity in the parent compound $BaFe_2As_2$", Nat. Commun. **4**, 2877 (2013).

[120] J. Linder and J. W. A. Robinson, "Superconducting spintronics", Nat. Phys. **11**, 307–315 (2015).

[121] J. Y. Tsao, *Materials Fundamentals of Molecular Beam Epitaxy* (Academic Press, Boston, 1993).

[122] W. K. Burton, N. Cabrera, and F. C. Frank, *The growth of crystals and the equilibrium structure of their surfaces*, Vol. 243 (Phil. Trans. R. Soc. Lond. Series A, Mathematical and Physical Sciences, 1951), pp. 299–358.

[123] T. Nishinaga and K.-I. Cho, "Theoretical study of mode transition between 2D nucleation and step flow in MBE growth of GaAs", Jpn. J. Appl. Phys. **27**, L12 (1988).

[124] T. Nishinaga, "Nucleation and Surface Diffusion in Molecular Beam Epitaxy", in *Handbook of Crystal Growth, Second Edition* (Elsevier, 2015) Chap. 23, pp. 943–982.

[125] T. Nishinaga and T. Suzuki, "Towards understanding the growth mechanism of III-V semiconductors on an atomic scale", J. Cryst. Growth **128**, 37–43 (1993).

[126] Eberl MBE-Komponenten, *DECO Compound Source - Technical Data Sheet*, `https://www.mbe-komponenten.de/pdf/data-sheet-deco.pdf`, Accessed: 2025-09-29.

[127] P. Laukkanen, J. Sadowski, and M. Guina, "Surface Studies by Low-Energy Electron Diffraction and Reflection High-Energy Electron Diffraction", in *Semiconductor Research: Experimental Techniques*, edited by A. Patane and N. Balkan (Springer, Berlin, Heidelberg, 2012), pp. 1–21.

[128] D. K. Biegelsen et al., "Surface reconstructions of GaAs(100) observed by scanning tunneling microscopy", Phys. Rev. B **41**, 5701 (1990).

[129] W.-K. Chu, J. W. Mayer, and M.-A. Nicolet, *Backscattering Spectrometry* (Academic Press, 1978).

[130] M. Mayer, *SIMNRA User's Guide*, tech. rep. IPP 9/113 (Max-Planck-Institut für Plasmaphysik, Garching, Germany, 1997).

[131] J. I. Goldstein et al., *Scanning Electron Microscopy and X-ray Microanalysis*, 4th (Springer, 2018).

[132] D. B. Williams and C. B. Carter, *Transmission Electron Microscopy: A Textbook for Materials Science*, 2nd (Springer, 2009).

[133] Q. Design, *MPMS®3 SQUID Magnetometer*, `https://qdusa.com/products/mpms3.html`, Accessed: 2025-10-02.

[134] G. van der Laan and A. I. Figueroa, "X-ray magnetic circular dichroism — a versatile tool to study magnetism", Coord. Chem. Rev. **277–278**, 95–129 (2014).

[135] N. R. Werthamer, E. Helfand, and P. C. Hohenberg, "Temperature and purity dependence of the superconducting critical field, H_{c2}. III. Electron spin and spin-orbit effects", Phys. Rev. **147**, 295 (1966).

[136] A. Gurevich et al., "Very high upper critical fields in MgB_2 produced by selective tuning of impurity scattering", Supercond. Sci. Technol. **17**, 278 (2004).

[137] A. Gurevich, "Enhancement of the upper critical field by nonmagnetic impurities in dirty two-gap superconductors", Phys. Rev. B **67**, 184515 (2003).

[138] A. Gurevich, "Upper critical field and the Fulde-Ferrell-Larkin-Ovchinnikov transition in multiband superconductors", Phys. Rev. B **82**, 184504 (2010).

[139] C. Kittel, *Introduction to Solid State Physics*, 8th ed. (Wiley, New York, 2005).

[140] J. S. Kim, "A matrix formalism for the Hall effect in multicarrier semiconductor systems", J. Appl. Phys. **86**, 3187–3194 (1999).

[141] C. P. Bean, "Magnetization of high-field superconductors", Rev. Mod. Phys. **36**, 31 (1964).

[142] E. M. Gyorgy et al., "Anisotropic critical currents in $Ba_2YCu_3O_7$ analyzed using an extended Bean model", Appl. Phys. Lett. **55**, 283–285 (1989).

[143] G. Blatter et al., "Vortices in high-temperature superconductors", Rev. Mod. Phys. **66**, 1125 (1994).

[144] R. Griessen et al., "Evidence for mean free path fluctuation induced pinning in $YBa_2Cu_3O_7$ and $YBa_2Cu_4O_8$ films", Phys. Rev. Lett. **72**, 1910 (1994).

[145] F. London, *Superfluids*, Vol. 1 (John Wiley Sons, Inc., New York, 1950).

[146] W. A. Little and R. D. Parks, "Observation of quantum periodicity in the transition temperature of a superconducting cylinder", Phys. Rev. Lett. **9**, 9 (1962).

[147] V. V. Moshchalkov et al., "Effect of sample topology on the critical fields of mesoscopic superconductors", Nature **373**, 319–322 (1995).

[148] R. P. Groff and R. D. Parks, "Fluxoid quantization and field-induced depairing in a hollow superconducting microcylinder", Phys. Rev. **176**, 567 (1968).

[149] V. G. Kogan, J. R. Clem, and R. G. Mints, "Properties of mesoscopic superconducting thin-film rings: London approach", Phys. Rev. B **69**, 064516 (2004).

[150] I. Sochnikov et al., "Large oscillations of the magnetoresistance in nanopatterned high-temperature superconducting films", Nat. Nanotechnol. **5**, 516–519 (2010).

[151] S. B. Chung, H. Bluhm, and E.-A. Kim, "Stability of half-quantum vortices in $p_x + ip_y$ superconductors", Phys. Rev. Lett. **99**, 197002 (2007).

[152] G. B. Halász, "Fractional magnetoresistance oscillations in spin-triplet superconducting rings", Commun. Phys. **6**, 133 (2023).

[153] A. Almoalem et al., "The observation of π-shifts in the Little-Parks effect in 4Hb-TaS_2", Nat. Commun. **15**, 4623 (2024).

[154] Y. Li et al., "Observation of half-quantum flux in the unconventional superconductor β-Bi_2Pd", Science **366**, 238–241 (2019).

[155] V. B. Geshkenbein, A. I. Larkin, and A. Barone, "Vortices with half magnetic flux quanta in "heavy-fermion" superconductors", Phys. Rev. B **36**, 235 (1987).

[156] A. C. Yuan, E. Berg, and S. A. Kivelson, "Strain-induced time reversal breaking and half quantum vortices near a putative superconducting tetracritical point in Sr_2RuO_4", Phys. Rev. B **104**, 054518 (2021).

[157] J. Dai et al., "Iron pnictides as a new setting for quantum criticality", Proc. Natl. Acad. Sci. **106**, 4118–4121 (2009).

[158] G. P. Mikitik and E. H. Brandt, "Effect of pinning on the vortex-lattice melting line in type-II superconductors", Phys. Rev. B **68**, 054509 (2003).

[159] Q.-P. Ding et al., "Magnetic and transport properties of iron-platinum arsenide $Ca_{10}(Pt_{4-\delta}As_8)(Fe_{2-x}Pt_xAs_2)_5$ single crystal", Phys. Rev. B **85**, 104512 (2012).

[160] B. Shen et al., "Flux dynamics and vortex phase diagram in $Ba(Fe_{1-x}Co_x)_2As_2$ single crystals revealed by magnetization and its relaxation", Phys. Rev. B **81**, 014503 (2010).

[161] C. Chaparro et al., "Doping dependence of the specific heat of single-crystal $BaFe_2(As_{1-x}P_x)_2$", Phys. Rev. B **85**, 184525 (2012).

[162] J. Kacmarcik et al., "Strongly dissimilar vortex-liquid regimes in single-crystalline NdFeAs(O,F) and (Ba,K)Fe_2As_2: A comparative study", Phys. Rev. B **80**, 014515 (2009).

[163] F. Hunte et al., "Two-band superconductivity in $LaFeAsO_{0.89}F_{0.11}$ at very high magnetic fields", Nature **453**, 903–905 (2008).

[164] J. Jaroszynski et al., "Upper critical fields and thermally-activated transport of $NdFeAsO_{0.7}F_{0.3}$ single crystal", Phys. Rev. B **78**, 174523 (2008).

[165] M. Bristow et al., "Competing pairing interactions responsible for the large upper critical field in a stoichiometric iron-based superconductor $CaKFe_4As_4$", Phys. Rev. B **101**, 134502 (2020).

[166] M. Bristow et al., "Multiband description of the upper critical field of bulk FeSe", Phys. Rev. B **108**, 184507 (2023).

[167] J. Hänisch et al., "High field superconducting properties of $Ba(Fe_{1-x}Co_x)_2As_2$ thin films", Sci. Rep. **5**, 17363 (2015).

[168] W. R. Meier et al., "Anisotropic thermodynamic and transport properties of single crystalline $CaKFe_4As_4$", Phys. Rev. B **94**, 064501 (2016).

[169] K. Cho et al., "Anisotropic upper critical field and possible Fulde-Ferrell-Larkin-Ovchinnikov state in the stoichiometric pnictide superconductor LiFeAs", Phys. Rev. B **83**, 060502R (2011).

[170] M. Kano et al., "Anisotropy of the upper critical field in a Co-doped $BaFe_2As_2$ single crystal", J. Phys. Soc. Jpn. **78**, 084719 (2009).

[171] C. Tarantini et al., "Significant enhancement of upper critical fields by doping and strain in iron-based superconductors", Phys. Rev. B **84**, 184522 (2011).

[172] N. Kurita et al., "Pressure-induced superconductivity in $EuFe_2As_2$ without a quantum critical point: Magnetotransport and upper critical field measurements under high pressure", Phys. Rev. B **88**, 224510 (2013).

[173] N. Liu, J. Teng, and Y. Li, "Two-component anomalous Hall effect in a magnetically doped topological insulator", Nat. Commun. **9**, 1282 (2018).

[174] G. P. Papari and V. M. Fomin, "Quantum interference by vortex supercurrents", Phys. Status Solidi RRL **17**, 2300038 (2023).

[175] A. V. Samokhvalov et al., "Little-Parks oscillations in hybrid ferromagnet-superconductor systems", Phys. Rev. B **79**, 174502 (2009).

[176] C. Feng et al., "Magnetic ordering and dense Kondo behavior in $EuFe_2P_2$", Phys. Rev. B **82**, 094426 (2010).

[177] B. T. Thole et al., "3d X-ray-absorption lines and the $4f^n \rightarrow 3d^9 4f^{n+1}$ multiplets of the lanthanides", Phys. Rev. B **32**, 5107 (1985).

[178] G. van der Laan, "Hitchhiker's Guide to Multiplet Calculations", in *Magnetism: A Synchrotron Radiation Approach*, Vol. 697, edited by E. Beaurepaire et al., Lecture Notes in Physics (Springer, Berlin, Heidelberg, 2006), pp. 143–199.

[179] R. D. Cowan, *The Theory of Atomic Structure and Spectra* (University of California Press, Berkeley, 1992).

[180] G. van der Laan and B. T. Thole, "Strong magnetic X-ray dichroism in 2p absorption spectra of 3d transition-metal ions", Phys. Rev. B **43**, 13401 (1991).

[181] A. I. Buzdin, "Proximity effects in superconductor-ferromagnet heterostructures", Rev. Mod. Phys. **77**, 935–976 (2005).

[182] R. Cai, I. Žutić, and W. Han, "Superconductor/ferromagnet heterostructures: a platform for superconducting spintronics and quantum computation", Adv. Quantum Technol. **6**, 2200080 (2023).